TECHNISCHE UNIVERSITÄT MÜNCHEN
TUM School of Engineering and Design
Photogrammetrie und Fernerkundung

Change detection and geometric BIM verification for indoor construction site monitoring based on 3D point clouds and uncertainties

Theresa Meyer

Dissertation

2022

TECHNISCHE UNIVERSITÄT MÜNCHEN
TUM School of Engineering and Design

Change detection and geometric BIM verification for indoor construction site monitoring based on 3D point clouds and uncertainties

Theresa Emma Meyer

Vollständiger Abdruck der von der TUM School of Engineering and Design der Technischen Universität München zur Erlangung des akademischen Grades einer

Doktorin der Ingenieurwissenschaften (Dr.-Ing.)

genehmigten Dissertation.

Vorsitz:	Prof. Dr.-Ing. André Borrmann
Prüfer der Dissertation:	1. Prof. Dr.-Ing. Christoph Holst
	2. Prof. Dr.-Ing. Markus Gerke Technische Universität Braunschweig
	3. Prof. Dr.-Ing. Ansgar Brunn Technische Hochschule für angewandte Wissenschaften Würzburg-Schweinfurt

Die Dissertation wurde am 04.11.2022 bei der Technischen Universität München eingereicht und durch die TUM School of Engineering and Design am 22.05.2023 angenommen.

Abstract

Change detection in terms of construction progress documentation and evaluation is currently of great value for the construction industry and BIM. Not only many positive experiences in construction practice indicate a strong correlation between permanent construction monitoring and compliance with project schedule, but careful researches and case studies confirm this positive effects also from a scientific point of view. Nevertheless, in practice, progress monitoring and geometric evaluation are only poorly automated yet. Although 3D point clouds are well suited for fast and high resolution "as-built" scene capture on site, especially in indoor environments, these techniques still lack deliberate analysis, computer aided interpretation and strategies for metric evaluation.

This thesis aims to develop and investigate novel methods in the field of 3D point cloud based change detection and geometric evaluation for indoor BIM. The conducted research provides contributions to three major aspects: (i) an optimization procedure for image-to-BIM co-registration, (ii) a high resolution 3D point cloud based change detection approach and (iii) a method for the geometric verification of a given BIM.

An estimation model for the refinement of image-to-BIM co-registration is developed. It is based on the incidence condition between model edges and corresponding straight lines in an image. 3D model edges are considered to be statistically uncertain and assigned a standard deviation according to the Level of Accuracy (LOA) specification for BIM. Given an optimal alignment between a 3D point cloud and a BIM, a high-resolution change detection for indoor progress monitoring is achieved through a voxel based discretization of space and occupancy modeling. In order to evaluate the geometric quality of a BIM, the effects of geodetic point measures on the occupancy of space are mathematically modeled by belief functions and evaluated by utilizing the Dempster-Shafer theory of evidence. This novel method considers statistical uncertainties of both the measurement and the given model under test itself. It is adapted and adjusted for the usage of 3D point clouds from terrestrial laser scanning and photogrammetry.

The presented methods are demonstrated and evaluated on the basis of multi temporal point cloud datasets that were obtained from surveys on real construction sites and synthetic data as ground truth for accuracy assessment regarding image-to-BIM co-registration. The results show that 3D point clouds are suitable to verify a given BIM up to LOA 30/40 ($\sigma = 7.5\,\mathrm{mm}/\sigma = 2.5\,\mathrm{mm}$), if special attention is paid to the geometry during the acquisition by laser scanning or photogrammetry. A voxel based change detection application with 1 cm voxel size meets LOA 30. Furthermore, an image co-registration can be improved as long as the BIM compliant geodetic reference meet the requirements of LOA 30 or higher.

Kurzfassung

Änderungsdetektion im Sinne von Baufortschrittsdokumentation und -evaluation ist derzeit von großem Wert für die Baubranche und BIM. Nicht nur viele positive Erfahrungen aus der Baupraxis zeigen einen starken Zusammenhang zwischen permanenter Bauüberwachung und der Einhaltung des Projektzeitplans. Untersuchungen und Fallstudien bestätigen diese positiven Effekte auch aus wissenschaftlicher Sicht. Dennoch sind Baufortschrittsüberwachung und die geometrische Evaluation in der Praxis bisher nur wenig automatisiert. Obwohl 3D-Punktwolken für die schnelle und hochauflösende Erfassung des Ist-Zustandes auf der Baustelle, insbesondere in Innenräumen, gut geeignet sind, fehlt es diesen Verfahren noch an kontextbezogener Analyse, computergestützter Interpretation und Strategien zur metrischen Bewertung.

Ziel dieser Arbeit ist die Entwicklung und Untersuchung neuer Methoden im Bereich der 3D-Punktwolken-basierten Änderungsdetektion und geometrischen Bewertung für BIM im Innenbereich. Die durchgeführte Forschung liefert Beiträge zu drei Hauptaspekten: (i) ein Optimierungsverfahren für die Bild-zu-BIM-Koregistrierung, (ii) einen hochauflösenden 3D-Punktwolken-basierten Ansatz zur Änderungsdetektion und (iii) eine Methode zur geometrischen Verifizierung eines gegebenen BIM.

Zunächst wird ein Schätzmodell für die Verfeinerung einer Ko-Registrierung von Bild-zu-BIM entwickelt. Es basiert auf der Inzidenzbedingung zwischen Modellkanten und entsprechenden Linien in einem Bild. 3D-Modellkanten werden als statistisch unsicher angesehen und mit einer Standardabweichung gemäß der Level of Accuracy (LOA) Spezifikation für BIM versehen. Unter der Voraussetzung einer optimalen Georeferenzierung einer 3D-Punktwolke im Gebäudereferenzsystem wird durch voxelbasierte Diskretisierung des Raums und Belegungsmodellierung eine hochauflösende Änderungserkennung für die Überwachung von Fortschritten in Innenräumen erreicht. Um die geometrische Qualität eines BIM zu bewerten, werden die Auswirkungen geodätischer Punktmessungen auf die Raumbelegung mathematisch durch Glaubensfunktionen modelliert und unter Verwendung der Dempster-Shafer-Evidenztheorie bewertet. Diese neuartige Methode berücksichtigt statistische Unsicherheiten sowohl der Messung als auch des zu prüfenden Modells selbst. Sie wird jeweils für die Verwendung von 3D-Punktwolken aus terrestrischem Laserscanning und Photogrammetrie optimiert.

Die vorgestellten Methoden werden anhand von multitemporalen Punktwolkendatensätzen demonstriert und evaluiert, die aus Vermessungen auf realen Baustellen gewonnen wurden. Darüber hinaus werden synthetischen Daten als Ground Truth für die Genauigkeitsbewertung der Bild-zu-BIM Ko-Registrierung genutzt. Die Ergebnisse zeigen, dass 3D-Punktwolken geeignet sind, ein gegebenes BIM bis hin zu LOA 30/40 ($\sigma = 7,5\,\mathrm{mm}/\ \sigma = 2,5\,\mathrm{mm}$) zu verifizieren, wenn der Aufnahmegeometrie bei der Erfassung durch Laserscanning oder Photogrammetrie besondere Beachtung zukommt. Ein voxelbasierter Ansatz zur Erkennung von Änderungen mit einer Voxelgröße von 1 cm erfüllt die Anforderungen von LOA 30. Darüber hinaus kann die Ko-Registrierung von Bildern mit dem Modell verbessert werden, solange die BIM-konforme Modellreferenz den Anforderungen von LOA 30 oder höher gerecht wird.

Content

List of Abbreviations

Abbreviation	Description	Page
2D	two dimensional	20
3D	three dimensional	17
ALS	Airborne Laser Scanning	21
BIM	Building Information Modeling/ Model	17
DP	Dense Point	57
GCP	Ground Control Point	20
GIS	Geo Information Science/ System	103
GNSS	Global Navigation Satellite System	18
GPS	Global Positioning System	19
FPV	First Person View	19
IMU	Inertial Measurement Unit	35
INS	Inertial Navigation System	20
LiDAR	Light Detection and Ranging	22
LOA	Level of Accuracy	33
LOD	Level of Detail	62
MLS	Mobile Laser Scanning	21
MVS	Multi View Stereo	35
OP	Object Point	30
RGB	Red, Green and Blue (image)	24
SfM	Structure from Motion	20
SGM	Semi Global Matching	32
SIFT	Scale Invariant Feature Transform	31
TLS	Terrestrial Laser Scanning	21
TP	Tie Point	19
USIBD	United States Institute of Building Documentation	33

List of Figures

List of Tables

1 Introduction

Within the framework and process of Building Information Modeling (BIM), modern construction projects benefit from Building Information Models (BIMs). Such a model represents a hierarchical structure of building and construction related objects, which are composed of both 3D geometry and semantics, including comprehensive information regarding the relationships between elements [Borrmann et al., 2021]. BIMs are considered fundamentally important as they act as a central and multidisciplinary database and digital platform for all project participants such as architects, engineers, trades, manufacturers and construction managers. The BIM is used over the entire life cycle of a building - from design and planning to execution and operation. Therefore, it is supposed to represent the planned state of building objects in their various phases of construction and operation. To conduct spatio-temporal analysis properly and in order for the construction management to be able to react to possible deviations from the planning at an early stage, a regular comparison of the as-planned and as-built project status must be carried out, because a BIM is only as valuable as the degree of its correspondence to real world conditions is high. In this context, this thesis addresses the comparison of BIM related 3D geometry and geodetic observations of the real building object, which is in the following referred to as construction progress documentation. In particular, the geometric-statistical evaluation of given model geometry with respect to the verification of metric tolerances is of great importance.

as-planned BIM

as-built BIM

Figure 1.1: BIM transition from as-planned (left) to as-built (right) using image data and generated 3D point clouds

1.1 Motivation

Change detection and geometry verification in terms of construction progress documentation and evaluation is currently of great interest for the branch of Architecture, Engineering and Construction (AEC) and BIM processes. Not only many positive experiences in construction practice indicate a strong correlation between permanent construction monitoring and compliance with project schedule, but careful researches and case studies such as presented in Alizadehsalehi & Yitmen

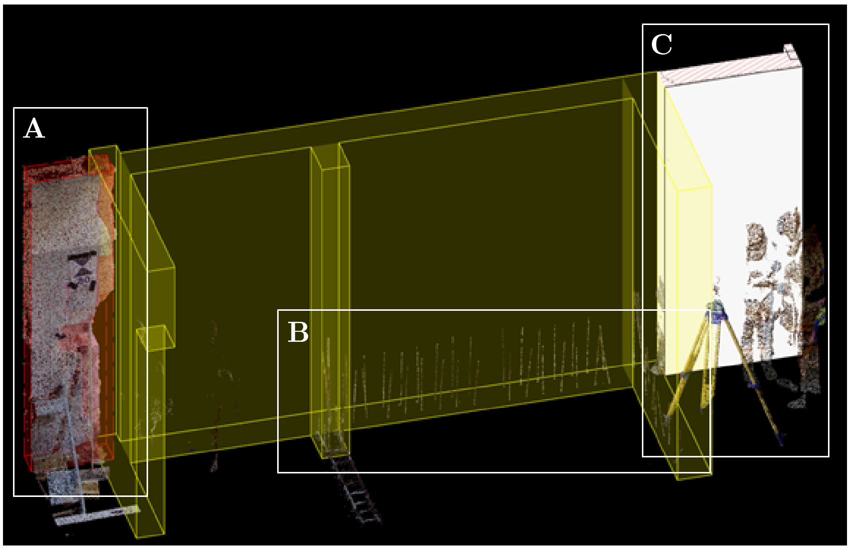

Figure 1.2: As-built point clouds for BIM: BIM objects superimposed with a 3D point cloud as a result of construction progress documentation; detail A: A piece of wall marked as going to be demolished in the course of a reconstruction (transparent red); detail B: From the captured reinforcement steel, it can be seen that a new wall is in its first state of construction (transparent yellow); detail C: Model of an existing wall from the BIM (solid white) with scanning artifacts in front of it (surveying engineers with tripod).

[2019] confirm this positive effects also from a scientific point of view. Nevertheless, progress monitoring and evaluation during the construction phase are usually time-consuming and still only poorly automated. So far progress monitoring either comes with visual inspections performed by construction workers or time and cost-intensive professional surveys using total stations and leveling devices. 3D laser scanning and image-based 3D scene captures are good alternatives for fast and high resolution as-built recording on site and there are many approaches and techniques for reconstruction from 3D point clouds, e.g. assembled and discussed in Xu et al. [2021].

In a building constructions interior however, monitoring effort based on 3D point clouds is greater compared to exterior, and therefore mostly assumed unsuitable for high-frequency monitoring. This is due to very limited views in confined indoor environments, which usually cause weak scanning geometries, occlusions, low observational redundancies and hence the need for many scanning and observation stations. At the same time there is a great demand for the documentation of detailed interiors which require even higher geometric resolution and reliably confirmed accuracy. Additionally, the georeferencing of point clouds in a BIM reference system has been identified as a particular bottleneck indoors, as a traverse survey is necessary in the GNSS-denied environment in order to determine 3D coordinates of temporally mounted control point markers, e.g. checkerboard targets. Once 3D point cloud data is generated though, it is commonly overlaid and visualized with the BIM geometry in specialized 3D software so that trained users can make individual and subjective interpretations of the supposed construction progress (Fig. 1.2). However, these procedures are time-consuming and labor-intensive. Point cloud based approaches for BIM still lack deliberate analysis and computer aided interpretation, which is why there is a great demand for automation in monitoring based on point clouds and for the evaluation of metric tolerances in engineering practice.

Especially when it comes to design and construction in existing contexts, e.g. in the course of a conversion project, reliably as-built geometry serves as highly valuable planning basis. A so called "as-built BIM" is considered to represent the actually built conditions up to a certain level of detail and accuracy. Since the generation of model geometry requires a spatial sampling by some kind of geodetic measurement and a digital model fitting, which is usually characterized by some degree of generalization, as-built BIMs strongly differ in geometric quality. Generally, with the ongoing development of BIM processes, the demand on geometric model qualities are constantly increasing as as the geometric aspect of BIM is essential for connectivity, localization, spatial networking and monitoring of assets. This is especially true for the modeling of detailed structures in building interiors as they continue to be maintained beyond the construction phase as a central database for many applications such as, for example, indoor navigation, asset tracking, Location Based Services (LBS) and the Internet of Things (IoT). However, it is understandable that for planning purposes it is crucial whether the as-built geometry is reliably true to form or consists only of rough geometric primitives. In this context, standardized approaches for the geometric validation of as-built BIMs considering both measurement and modeling related uncertainties are needed.

1.2 State-of-the-art

A BIM compliant model is object-oriented and the spatial relationship of those geometric objects within a buildings interior, in addition to their spatial appearance are subject of this work. In particular, the subject area involves issues of automated co-registration, change detection and geometric model validation with special attention to statistical uncertainties. These aspects are considered the central fields of research. Many authors have already contributed to these fields and related sub-topics, which shall be presented and summarized in the following. They are an important foundation and framework without which this work could not have begun at this point.

1.2.1 Image-to-model co-registration

3D object recognition and localization in images depends on corresponding features between model and image. Through model-to-image matching, inferences can be made about scenes beyond what is explicitly available in the image. Model-to-image methods are often cited in the literature as a precursor to tracking, change detection, texture mapping, as well as sensor orientation and positioning applications. Lowe [1991] refers to the term *Model-based Vision*.

Geometric feature matching: Points can be used as correspondence features for the assignment between image and model: Hoegner & Stilla [2015] refine GPS camera positions of a thermal infrared image sequence, which is matched with 3D vertex coordinates of a pre-known building model. Avbelj et al. [2010] improve the exterior orientation of infrared images by point-to-point matching with 3D wireframe models using Förstner points and intersections of straight segments. Lerner et al. [2006] presented a method for accurately determining sensor pose and motion using homologous image points and an already given digital terrain model, and Unger et al. [2016] use Tie Points (TP), which they assign to levels of a generalized building model using a distance criterion. Edge detection is a standard task of digital image processing, which is why line features are particularly suitable in the context of building model matching. Iwaszczuk & Stilla [2017] use corresponding image lines and 3D model edges to refine the coarse camera pose of thermal infrared images for texture extraction. In Läbe & Ellenbeck [1996], lines from approximately oriented aerial images are extracted and edges are assigned from 3D wireframe models of buildings. Li-Chee-Ming & Armenakis [2013] use vertical lines from video streams from a UAV-borne First-Person-View (FPV) camera in urban areas, which they match with extracted lines from synthetic images of 3D building models. For this purpose, the authors realize in Li-Chee-Ming & Armenakis [2014] an efficient model-to-image matching using geometric hashing. Li-Chee-Ming & Armenakis [2017] use vertical lines matched with a 3D model to determine a sensor pose indoors. Other related works with examples of successful line matching are Gerke [2011], Schickler [1992], Lee et al. [2002],

Kada & Haala [2005], Iwaszczuk [2015], Nyaruhuma et al. [2012], Boerner & Kröhnert [2016] and Koch et al. [2016].
A-priori information about the parallelism of object lines extracted in the image can be exploited by applying automatic vanishing point detection. This technique can be used for both 3D reconstruction and determination of external orientation parameters and is used in van den Heuvel [1998], Rother [2000], and Förstner [2010], among others. The combination of points and lines is also described in the literature: Jung et al. [2016] extract building corners with associated edges (edged corner feature) from aerial images, which they map to corresponding elements from 3D building models, and Tian et al. [2008] combine reliably mapped point features with edges in video sequences, aiming to reconstruct the 3D structures of objects. Edge matching in this case is only between images and not with an a priori 3D object model. However, linked vertices and edges represent valuable topological constraints for the reconstruction of 3D structures. Lowe [1991], on the other hand, extracts contours in the image and uses them to determine projection and model parameters of objects to be detected and tracked. Unger et al. [2017] generate sparse point clouds from UAV images using Structure from Motion (SfM), in which planes are estimated and assigned to the corresponding planes (facades) of 3D building models. Furthermore, there are also works that utilize textures: DeGol et al. [2016] combine 2D and 3D information from oriented images, which they use in different ways for material classification. A given object model is not included. However, the authors give an outlook that this new method can be further improved with the introduction of context-based constraints. Nakagawa & Shibasaki [2008] detect changes in buildings using aerial images and given textured 3D reference models. However, the exact orientation of the new comparison images is a basic requirement in this work. Molton et al. [2004] use locally planar patch features instead, where the image texture is attached to small, local 3D surfaces and the current estimates of camera and feature position are used to predict and search for the texture on the expected appearance.

Relational matching: The information from images and 3D models can be available in various degrees of abstraction - from simple gray values (e.g. gradients), to extracted points, lines and regions, to relational descriptors. Relational feature mapping uses contextual information between features. The features are therefore not considered to be independent of each other. For example, a polygon can represent the outline of a region. When searching for the corresponding elements, the search can be limited to such pairs of polygons and regions that have similar attributes and are in the same relationship. Vosselman [1992] gives an overview of the relational matching method, and in particular addresses the qualitative evaluation of correspondences. He also presents a method for evaluation that combines matching strategies, approaches from information theory (mutual information), and hierarchical search methods. Eugster & Nebiker [2009] use relational matching for matching UAV-borne video images to 3D virtual city models. They state that this approach is computationally intensive compared to simple feature-based matching, but robust with respect to poor approximations of sensor orientation. Finally, Jung et al. [2016] realize feature matching with geometric hashing and context features, which, in addition to local edged corner features, give global structural information about the building object.

Approximate sensor orientation: To obtain approximate values for sensor pose, many authors use direct georeferencing of the mapping system. The parameters of the external orientation are determined with GNSS receiver (only outdoors) and an Inertial Navigation Systems (INS) if necessary. In addition, Ground Control Points (GCPs), besides the given 3D model, can be used in the object space. Gerke [2011] combines linear structures in urban aerial scenes (as fictitious observations in the bundle block adjustment) with some reduced number of GCPs. In Iwaszczuk [2015], model edges are projected into an oblique aerial image using coarse exterior orientation parameters obtained by direct georeferencing to reveal corresponding image line segments for each model edge. Similar approaches, where the sensor pose is approximately known before model-to-

image matching, can also be found in: Lerner et al. [2006], Avbelj et al. [2010], Braun et al. [2015], Unger et al. [2017, 2016] and Hoegner et al. [2017].
Due to signal shading, it is usually not possible to receive sufficiently good GNSS signals in building interiors. An (approximate) indoor positioning can be used in this case alternatively with technologies like Radio Frequency Identification (RFID) [Olszewski et al., 2013], WLAN [Youssef et al., 2003], radar [Bahl & Padmanabhan, 2000] or also infrared [Want et al., 1992], provided that a corresponding infrastructure is installed, which is usually not the case for construction scenarios. Retscher & Kistenich [2006] compare in their article different systems and technologies for positioning and navigation in buildings.

There are many valuable works on the topic of image-to-model matching from points and lines to surfaces and textures, but no specializations of these methods to interior BIM can be found in the literature yet.

1.2.2 Change detection and construction progress documentation

Change detection: Dense 3D point clouds can be analyzed to derive knowledge about the occupancy of space through voxel-based discretization. The origins of change detection based on 3D point clouds and occupancy grids are mainly in the field of informatics and robot navigation and were first introduced by Moravec & Elfes [1985]. Due to the practicality of this method, it has also already been used for several years in the field of engineering and geodesy to process high-quality point clouds from multi view photogrammetry and 3D laser scanning. Aijazi et al. [2013] process 3D point clouds based on occupancy grids for change classification in urban landscapes whereas Kromer et al. [2017] apply near-real-time detection for monitoring landslides from laser scanning point clouds. Also related to large-scale areas is the work of Hebel et al. [2013], who presented a method for automatic change detection from Airborne Laser Scanning (ALS) point clouds. They used a relatively coarse voxel space for comparing point clouds from different epochs and refined the change detection result by considering single points in pre-selected areas of interest. Gehrung et al. [2020, 2022] build up on the work of Hebel et al. [2013] and combined change detection based on single points and occupancy grids for Mobile Laser Scanning (MLS) data in order to efficiently handle occlusions and at the same time providing fast runtimes. A point based comparison for 3D change detection is also presented by Liu et al. [2021], who address the problem of point density variations in point clouds of buildings from Terrestrial Laser Scanning (TLS). They propose the calculation of adaptive thresholds to determine whether changes occurred between two point clouds and consider registration errors. The tremendous advances in voxel or single point based comparison of point clouds have created many opportunities for specialized applications in change detection, including buildings. However, the comparison of changes with respect to a specific model is not yet or hardly addressed in these publications. Wysocki et al. [2022] have contributed to the improvement and enhancement of 3D building models by comparing co-registered point clouds from mobile laser scanning with modeled building facades. The authors do not refer to BIM, however, the work in the field of 3D urban modeling can certainly be considered strongly related work.

Construction progress monitoring: Change detection in the context of BIM and site monitoring is a common application and wide-ranging research topic. Braun et al. [2015] and Tuttas et al. [2017] show how change detection based on photogrammetric point clouds, occupancy grids and visibility analysis is integrated into the BIM process where it has a positive impact on project progress. The change detection method introduced by Hebel et al. [2013] is also adopted to the field of construction site monitoring. Huang et al. [2022] utilized photogrammetric observations. They developed a method for point cloud registration as a prerequisite for geometric and semantic change detection based on voxel and occupancy grids on construction sites. Golparvar-Fard et al.

[2015] modeled the occupancy of space from unordered site images and analyzed the scene with a given BIM based on a robust registration approach and a proposed machine-learning scheme that automatically detects physical progress. Machine-learning and point based algorithms are also used by Shirowzhan et al. [2019], who track building and construction progress from airborne LiDAR point clouds. Other authors focus on point clouds from terrestrial laser scanning for construction progress documentation as well. Bosche & Haas [2008] contributed a method for the comparison of as-planned and as-built data based on terrestrial laser scanning. In a subsequent publication [Bosché et al., 2015], the authors focus on detecting and identifying cylindrical BIM objects that are not built in their intended location and considering their completeness based on TLS. Zhang & Arditi [2013] presented an automated process that measures construction progress in terms of percentage of completion by using TLS data which is superimposed on the reference model. Although they demonstrate feasibility, their experiments relate only to laboratory conditions and not to real construction projects. A comprehensive overview of change detection in construction industry based on point clouds and voxel representation is given in Xu et al. [2021].

Indoor applications and models: There are many works considering outdoor observations and the observation of sites that are still open and easily accessible in all areas because, for example, ceilings and roofs have not yet been installed. In recent years, more and more authors have taken up this issue and started to particularly address closed indoor scenarios and related point cloud applications. Nikoohemat et al. [2020, 2018] addressed processing 3D point clouds especially of indoor environments for reconstruction and analysis applications. They do not examine construction site applications, but rather exploit the indoor topology of existing buildings. Jung et al. [2018] claim that complex indoor environments still remain an open challenge for automated as-built BIM. The authors propose a method for 3D volumetric indoor reconstruction based on 3D point clouds, room segmentation and noise filtering. Yang et al. [2019] extended existing methods and resolved the special case of indoor reconstruction of multi-room environments with curved walls based on 3D point clouds. Tran & Khoshelham [2020] focus especially on indoor applications, because indoor point clouds are typically erroneous and incomplete. Therefore, they propose a novel method based on the combination of shape grammar and a data-driven process for procedural reconstruction of 3D indoor models from point clouds.

1.2.3 Uncertainty evaluation and evidence-based decision making

Measurement accuracy: A priori knowledge of the stochastic properties of the measuring sensor is important to detect outliers as well as to separate statistically significant deformations from the measurement uncertainty. Many authors such as Gordon & Lichti [2007], Golparvar-Fard et al. [2011], Soudarissanane et al. [2011] and Zámečníková et al. [2014] have comprehensively investigated error sources, influencing parameters and their effects on the geometric quality of 3D point clouds in order to allow for proper handling, compensation and prior accuracy assumption. Wujanz et al. [2018] and Tan et al. [2018] introduce intensity-based stochastic models while other authors particularly address systematic error models and propose calibration strategies for reducing the effect of systematic effects on practical deformation analyses [Lichti, 2007; Koch, 2008; Holst et al., 2018]. All of this work provides a valuable scientific basis for evaluating TLS-only accuracy. Photogrammetric applications for BIM commonly appear directly in context of construction progress monitoring. Dai & Lu [2010] assessed the general accuracy of image-measurements for as-built observations on construction sites by an analytical assessment based on regression and correlation coefficient in comparison to corresponding tape measurements. They already point out that for construction tasks, it is important to mind error tolerances and that the accuracy achievable by photogrammetry must be weighed against the accuracy desired for a particular engineering application. Another relatively early contribution is that of Golparvar-Fard et al. [2011] who compared image-based and TLS borne point clouds for modeling the as-is condition on construction sites. They state image-based point clouds to be less accurate compared to TLS point clouds. Later, Golparvar-Fard et al. [2015] integrated occupancy analyzes and propose a machine-learning approach for automated progress detection with an available BIM.

Uncertainty of the reference model: The subject of the research presented in this thesis is related to geodetic applications given a general geometric model. In particular, model related uncertainty is a main aspect. In this context previous works have also already considered the statistical uncertainty of model information. Therefore, uncertainty assessment is an important topic in "scan-to-BIM" applications, which is increasingly getting more and more attention. Sester & Förstner [1989] used mathematical statistics and probability theory to deal with the problem of uncertainty encountered during the pose estimation of objects from digital images, for which models are known and Meidow et al. [2009] discuss representations of uncertain geometric image features. A later work of Iwaszczuk & Stilla [2017] picks up on that topic and considers the uncertainty of 3D building models as geometric constraint for camera pose optimization of aerial thermal images. The valuable contributions of Förstner & Wrobel [2016] and Heuel & Förstner [2001]; Heuel [2004] are not necessarily related to BIM but with focus on reasoning with uncertain given model features. The geometric quality of a given BIM is crucial when it comes to a comparison of as-planned and as-built. The overall accuracy of this process depends not only on the measurement accuracy, but in particular significantly on the geometric quality of the given BIM. Esfahani et al. [2021] address this problem and assess the impact of levels of automation and modeller training on the accuracy and precision of generated BIMs. A related approach is visual localization from indoor images in combination with an available BIM based on line-features as introduced by Acharya et al. [2019].

Evidence based reasoning: In order to manage different sources of uncertainty properly, a special theory following Shafer [1976] and Dempster [1976] can be used. It is a mathematical theory of evidence and a theory of probable reasoning. It deals with weights of evidence and with numerical degrees of support based on evidence. Reineking [2014] gives an overview of belief function theory and demonstrates its application in different contexts. In the context of computer vision Zlatoff et al. [2006] presented a framework for perceptual grouping, on region-based segmented images based on evidence from multiple sources. Using Dempster-Shafer theory for geodetic applications has been introduced by Hebel et al. [2013], who have incorporated the theory for change detection of airborne laser scanning (ALS) point clouds. They formulated belief functions to derive belief masses pointing to both the states occupied" and "empty". They processed every single ALS point in the vicinity of arbitrary targeted locations and evaluated the result from the combination multiple evidence. Huang et al. [2022] transferred evidence theory and belief masses on the modeling of photogrammetric observations. They developed a method for point cloud registration as prerequisite for geometric and semantic change detection based on voxel and occupancy grids on construction sites. These previous works represent the basis for the methodology presented in this thesis, where the belief function theory is adopted for TLS and photogrammetric observations.

The problem of statistical uncertainty has been successfully addressed in many contexts, so that standardized methods have been established for many practical problems of engineering and construction. However, in the specific area of as-built documentation of building interiors and the associated accuracy requirements, there is still a research gap to be identified.

1.3 Objectives and contributions

In contrast to related work in the field of monitoring and evaluation for BIM, this research project is characterized in particular by two major aspects:

1) This thesis adresses change detection primarily in indoor scenarios, because a building's interior, especially when it is under construction, is a much more challenging environment compared to its exterior. This is due to constraint scanning geometries, low observational redundancy and weak georeferencing whilst high architectonic symmetry resulting in ambiguities during processing and analysis. Related work and approaches addressing change detection for BIM largely rely on outside observations.

2) Uncertainties are explicitly considered and integrated using classical probability theory and the Dempster-Shafer evidence theory. On the one hand, these uncertainties refer to the physical properties of the geodetic measurements, the coordinate reference frame and the point cloud alignment but on the other hand, the novelty of our research results from the consideration of the indoor model to be checked and validated itself as statistically uncertain. In contrast to previous works in the field of change detection for BIM, we are particularly capable of evaluating the significance of detected changes by considering the quality of the reference model itself.

Focusing on these aspects, we aim to answer the following research questions, which have not yet been considered or fully addressed in state of the art literature:

I To what extend do geometric uncertainties of BIM related reference objects effect the accuracy of an image-to-model co-registration? Is the geometric quality of common BIM-compliant interior models sufficient to serve as a geodetic reference itself and to make statements about the compliance with metric tolerances?

II What are the limits of automated 3D point cloud based change detection in terms of detail and resolution? Is it sufficient for interior building documentation with associated accuracy requirements?

III Which accuracy classes for BIM can still be verified with sufficient confidence using common laser scanners and RGB cameras?

1.4 Structure and organization

This thesis is structured as follows: Chapter 2 provides theoretical background on selected topics that represent important foundations to the methodologies described in the following chapters. These mainly include projective mappings with homogeneous representations of points and lines, estimation theory for bundle adjustment including accuracy assessment, and an introduction to evidence theory according to Dempster and Shafer.

Chapter 3 represents the starting point for the scientific work of this thesis. It deals with an approach for image-to-BIM co-registration based on corresponding straight line features, where not only extracted image lines are supposed to be statistically uncertain but also the BIM related model edges. The main contribution of this first part is the derivation and formulation of the functional model for an optimization procedure in the projective space that is based on a constraint Gauss-Helmert model. This is followed by a guide back to the Euclidean interpretation of the results.

In Chapter 4, the focus is shifted to terrestrial laser scanning, 3D point clouds and a change detection approach for construction progress monitoring. High resolution occupancy modeling for voxel based change detection is introduced and it is investigated whether the geometric resolution meets common accuracy requirements in professional building documentation for BIM processes.

Chapter 5 deals with a novel method for the geometric validation of a BIM. It is demonstrated how to model the occupancy of space from single laser and image points with belief functions prior to an evidence based reasoning pipeline. This involves an accuracy assessment of single point qualities and a proposal for the separate treatment of photogrammetric tie points and the image based dense cloud. In particular, it is shown how to integrate the uncertainty of a given BIM and how to combine potentially conflicting and non-conflicting evidence properly in order to make a final decision.

In order to verify the theses and methods, a series of experiments was conducted partially with synthetic data as ground truth for accuracy evaluation but also carried out on real indoor construction sites. Chapters 6, 7 and 8 introduce and discuss the used point cloud and BIM data, the different experimental designs and the achieved results. Finally, Chapter 9 answers the specific research questions of Sec. 1.3 and gives general conclusions and an outlook on future work and open topics in this research field.

2 Basics

This chapter provides theoretical background of selected subjects that built an important foundation for the methodology of this thesis. The topics relate to photogrammetric observations of geometric features, followed by according estimation and accuracy assessment strategies, the generation of 3D point clouds from active and passive sensor technologies, and an introduction to evidence based reasoning according to Dempster-Shafer theory. The chapter closes with an overview of requirements and specifications for as-built documentation for BIM.

2.1 Representation and estimation of geometry from images

An essential prerequisite for applications and approaches based on photogrammetry is a suitable representation of geometrical features. Geometric observations are then processed in bundle block adjustment for parameter estimation and evaluated in terms of accuracy. The results can then be used in further analysis and processing.

2.1.1 Homogeneous representation of points and lines

A 2D point with Euclidean coordinates $\chi = [x, y]^T$ can be represented homogeneously $x \rightarrow \mathbf{x}$:

$$\mathbf{x} = \begin{bmatrix} x_o \\ x_h \end{bmatrix} = \begin{bmatrix} u \\ v \\ w \end{bmatrix} = \begin{bmatrix} \lambda x \\ \lambda y \\ \lambda \end{bmatrix} \tag{2.1}$$

x_o represents the Euclidean part, whereas x_h denotes the homogeneous part of the homogeneous vector.

Analogously, 3D point with Euclidean coordinates $\mathcal{X} = [X, Y, Z]^T$ can be represented homogeneously $X \rightarrow \mathbf{X}$:

$$\mathbf{X} = \begin{bmatrix} X_o \\ X_h \end{bmatrix} = \begin{bmatrix} U \\ V \\ W \\ T \end{bmatrix} = \begin{bmatrix} \lambda X \\ \lambda Y \\ \lambda Z \\ \lambda \end{bmatrix} \tag{2.2}$$

X_o represents the Euclidean part, whereas X_h denotes the homogeneous part of the homogeneous vector.

In the Euclidean plane, a line representing the x-axis has the form $l_x(\theta, r)$, with $\theta = 90°$ and $r = 0$. A straight line with the parameters θ and r is given in Hessian normal form, where θ is the direction of the normal (counterclockwise direction from the x-axis) and r is the shortest distance from the origin.

A straight line can also be described homogenously by $ax + by + c = 0$ and represented by a homogeneous vector:

$$\mathbf{l} = \begin{bmatrix} a \\ b \\ c \end{bmatrix} = \begin{bmatrix} cos(\theta) \\ sin(\theta) \\ -d \end{bmatrix} \tag{2.3}$$

In homogeneous coordinates $l_x(\theta, r)$ has the form:

$$\mathbf{l}_x = \begin{bmatrix} 0 \\ 1 \\ 0 \end{bmatrix} \tag{2.4}$$

Based on the representation for the x-axis ($\mathbf{l}_x$), any straight line $\mathbf{l}$ can be represented by rotation through an angle α and translation with a vector $x_t = (t_x, t_y)$.

$$\mathbf{l} = T(x_t)R(\alpha)\mathbf{l}_x = \begin{bmatrix} 1 & 0 & 0 \\ 0 & 1 & 0 \\ -t_x & -t_y & 1 \end{bmatrix} \begin{bmatrix} sin(\alpha) & cos(\alpha) & 0 \\ -cos(\alpha) & sin(\alpha) & 0 \\ 0 & 0 & 1 \end{bmatrix} \begin{bmatrix} 0 \\ 1 \\ 0 \end{bmatrix} \tag{2.5}$$

A 3D line is expressed with Plücker coordinates by a 6-parameter vector:

$$\mathbf{L} = (L_1, L_2, L_3, L_4, L_5, L_6)^T \tag{2.6}$$

with the homogeneous part $\mathbf{L}_h = (L_1, L_2, L_3)^T$ and the Euclidean part $\mathbf{L}_O = (L_4, L_5, L_6)^T$. A 3D line has a start and an end point $\mathbf{X}$ and $\mathbf{Y}$. In homogeneous coordinates, a 3D line $\mathbf{L}$ is most easily described by connecting two 3D points ($\mathbf{X}$ and $\mathbf{Y}$):

$$\mathbf{L} = \mathbf{X} \wedge \mathbf{Y} = \begin{bmatrix} \mathbf{L}_h \\ \mathbf{L}_O \end{bmatrix} = \Pi(\mathbf{X})\mathbf{Y} \tag{2.7}$$

with

$$\Pi(\mathbf{X}) := \frac{\partial \mathbf{X} \wedge \mathbf{Y}}{\partial \mathbf{Y}} = \begin{bmatrix} T & 0 & 0 & -U \\ 0 & T & 0 & -V \\ 0 & 0 & T & -W \\ 0 & -W & V & 0 \\ W & 0 & -U & 0 \\ -V & U & 0 & 0 \end{bmatrix} \tag{2.8}$$

where U, V, W and T are the elements of the homogeneous 3D point vector.

In the projective space, a 3D line can be described by the Plücker matrix as well:

$$\Gamma(\mathbf{L}) = \mathbf{X}\,\mathbf{Y}^T - \mathbf{Y}\,\mathbf{X}^T = \begin{bmatrix} -S_{\mathbf{L}_0} & -\mathbf{L}_h \\ \mathbf{L}_h^T & 0 \end{bmatrix} \tag{2.9}$$

with the 3×3 skew matrix $S_{\mathbf{L}_0}$:

$$S_{\mathbf{L}_0} = \begin{bmatrix} 0 & -L_6 & L_5 \\ L_6 & 0 & -L_4 \\ -L_5 & L_4 & 0 \end{bmatrix} \tag{2.10}$$

2.1.2 Bundle adjustment using Gauss-Markov model

Photogrammetric methods are very popular for fast, flexible and above all cost-efficient 3D scene capture. It allows obtaining geometric and radiometric object information from images. The prerequisite is a mathematical modeling of the camera and the mapping process.

Mapping an object point $\mathcal{X}_i(\mathbf{X}_i)$ to an image point $\chi_{it}(\mathbf{x}_{it})$ with a pinhole camera $({}_t)$ is achieved by multiplication with the projection matrix P_t:

$$\mathbf{x}_{it} = \mathrm{P}_t\,\mathbf{X}_i \tag{2.11}$$

With calibration matrix K, rotation matrix R, identity matrix I_3 and the inhomogeneous 3D coordinates of the projection center $\boldsymbol{O}$, the homogeneous P-matrix results from:

$$\mathrm{P}_t = \mathrm{K}\,\mathrm{P}_t^c = \mathrm{K}\,\mathrm{R}_t\,[\mathrm{I}_3| - \boldsymbol{O}_t] \tag{2.12}$$

Bundle adjustment is applied to process an arbitrary number of images in order to reconstruct a 3D scene with respect to a superior coordinate system, e.g. the BIM's reference system. The parameters to be estimated are camera poses (exterior orientation), 3D object point coordinates and commonly a camera's interior orientation. In the following, the adjustment is based on the nonlinear *Gauss-Markov* functional model for the (inhomogeneous) coordinates of the obtained image points $\boldsymbol{x}'_{it}$ for observed 3D scene points $\mathbf{X}_i$.

$$\underline{\boldsymbol{x}}'_{it} = c(\mathrm{K}\,\mathrm{P}_t^c\,\mathbf{X}_i) \tag{2.13}$$

with $c(x) = \boldsymbol{x}_o/x_h$ where $\boldsymbol{x}_o$ denotes the Euklidean and x_h the homogeneous part of the homogeneous representation. Equation 3.5 is equivalent with the well known collinear equations. The measured image coordinate is considered a stochastic variable and therefore indicated by an underscore. For the adjustment, the observations are described as functions of the unknown parameters:

$$\underline{\boldsymbol{x}}'_{it} + \hat{\boldsymbol{v}}_{it} = \boldsymbol{f}_{it}(\mathbf{X}_i, \boldsymbol{p}_t, \boldsymbol{s}) \tag{2.14}$$

The term $\underline{\boldsymbol{x}}'_{it} + \hat{\boldsymbol{v}}_{it}$ relates to the observed inhomogeneous image coordinates, e.g. automatically detected from an interest operator, with their corresponding residuals, which are returned from the mathematical model. Besides the unknown coordinates of the 3D scene points $\mathbf{X}_i$, the six pose parameters per image $\boldsymbol{p}_t$ as well as the interior orientation parameters $\boldsymbol{s}$ of the camera are to be adjusted and processed in the function $\boldsymbol{f}_{it}$. Based on approximate values for the unknown parameters (denoted by superscript $({}^a)$), the linearized model for bundle adjustment is obtained:

$$\Delta\boldsymbol{x}'_{it} + \hat{\boldsymbol{v}}_{it} = \mathsf{C}_{it}\widehat{\Delta\mathbf{X}_i} + \mathsf{D}_{it}\widehat{\Delta\mathbf{p}_t} + \mathsf{H}_{it}\widehat{\Delta\mathbf{s}} \tag{2.15}$$

where $\Delta\boldsymbol{x}'_{it} := \boldsymbol{x}'_{it} - \hat{\boldsymbol{x}}'^a_{it}$ with $\hat{\boldsymbol{x}}'^a_{it} = \boldsymbol{f}_{it}(\hat{\mathbf{X}}_i^a, \hat{\boldsymbol{p}}_t^a, \hat{\boldsymbol{s}}^a)$. C_{it}, D_{it} and H_{it} are the Jacobians of the model function with respect to the unknowns $\mathbf{X}_i$, $\mathbf{p}_t$ and $\mathbf{s}$. Since $\boldsymbol{f}_{it}$ is nonlinear, the Jacobians are recalculated at each iteration based on the current estimates of the parameters.

$$\mathsf{C}_{it} = \frac{\partial \boldsymbol{f}_{it}(\mathbf{X}_i, \boldsymbol{p}_t, \boldsymbol{s})}{\partial \mathbf{X}_i},\ \mathsf{D}_{it} = \frac{\partial \boldsymbol{f}_{it}(\mathbf{X}_i, \boldsymbol{p}_t, \boldsymbol{s})}{\partial \mathbf{p}_t},$$

$$\mathsf{H}_{it} = \frac{\partial \boldsymbol{f}_{it}(\mathbf{X}_i, \boldsymbol{p}_t, \boldsymbol{s})}{\partial \mathbf{s}}$$

The Gauss-Markov model is achieved by rewriting the notation within the estimation:

$$\widehat{\Delta\mathbf{y}} = \Delta\mathbf{y} + \hat{\mathrm{v}} = \mathsf{A}\,\widehat{\Delta\boldsymbol{\beta}} = [\mathsf{C}\,\mathsf{D}\,\mathsf{H}] \begin{bmatrix} \widehat{\Delta\mathbf{X}} \\ \widehat{\Delta\mathbf{p}} \\ \widehat{\Delta\mathbf{s}} \end{bmatrix} \tag{2.16}$$

with the vectors $\Delta\mathbf{y} := [\Delta\boldsymbol{x}'_{it}]$ referring to the observations and $\widehat{\Delta\boldsymbol{\beta}} = \hat{\boldsymbol{\beta}} - \hat{\boldsymbol{\beta}}^a$ referring to the unknown parameters.

2.1.3 Accuracy assessment

A proper uncertainty assessment is the general basis for the verification of a geometric model and a-priori standard deviations σ_y^a are a first intuitive quality indicator for the observations. They are based on past experiences and specifications and reflect the estimated uncertainty, e.g. 1 pixel[*] for tie point (TP) observations and 15 mm[†] for Object Point (OP) observations in a spatial reference system. The covariance matrix of the observations $\Sigma_{\mathbf{yy}}$ results from the approximate initial covariance matrix and an initial variance factor which is chosen to be $\sigma_0^2 = 1$:

$$\Sigma_{\mathbf{yy}} = \sigma_0^2 \, \Sigma_{\mathbf{yy}}^a \tag{2.17}$$

As there are different observation types involved (TP and OP), the a-priori covariance matrix has the form

$$\Sigma_{\mathbf{yy}}^a = \begin{pmatrix} \sigma_{TP}^2 \Sigma_{TP}^a & 0 \\ 0 & \sigma_{OP}^2 \Sigma_{OP}^a \end{pmatrix}$$

The individual variance components σ_{TP}^2 and σ_{OP}^2 can be evaluated for their corresponding group of observations.

The stochastic model is supposed to increase the influence of individual observations with higher accuracy. This is achieved by integrating the weight matrix $\mathsf{W}_{\mathbf{yy}} = \Sigma_{\mathbf{yy}}^{-1}$ into the normal equations:

$$\mathsf{A}^T \, \mathsf{W}_{\mathbf{yy}} \, \mathsf{A} \, \widehat{\Delta\boldsymbol{\beta}} - \mathsf{A}^T \, \mathsf{W}_{\mathbf{yy}} \, \widehat{\Delta\mathbf{y}} = \mathbf{0} \tag{2.18}$$

The unknown parameters result from $\hat{\boldsymbol{\beta}} = \boldsymbol{\beta}^a + \widehat{\Delta\boldsymbol{\beta}}$ with

$$\widehat{\Delta\boldsymbol{\beta}} = (\mathsf{A}^T \, \mathsf{W}_{\mathbf{yy}} \, \mathsf{A})^{-1} \, \mathsf{A}^T \, \mathsf{W}_{\mathbf{yy}} \, \Delta\mathbf{y} \tag{2.19}$$

with the assigned covariance matrix of the estimated parameters:

$$\Sigma_{\hat{\boldsymbol{\beta}}\hat{\boldsymbol{\beta}}} = \hat{\sigma}_0^2 (\mathsf{A}^T \, \mathsf{W}_{\mathbf{yy}} \, \mathsf{A})^{-1} \tag{2.20}$$

Using the initial weight matrix $\mathsf{W}_{\mathbf{yy}}^a$ of the observations, the estimated variance factor is given by the weighted sum of the squared residuals and the overall redundancy $R = N - U$ (N number of observations, U number of unknowns):

$$\hat{\sigma}_0^2 = \frac{\hat{\boldsymbol{v}}^T \, \mathsf{W}_{\mathbf{yy}}^a \, \hat{\boldsymbol{v}}}{R} \tag{2.21}$$

where $\hat{\boldsymbol{v}} = A \, \widehat{\Delta\boldsymbol{\beta}} - \Delta\mathbf{y}$ is the vector with the estimated corrections. The estimated variance factor is used to end up with the estimated covariance matrix of the observations:

$$\widehat{\Sigma_{\mathbf{yy}}} = \hat{\sigma}_0^2 \, \Sigma_{\mathbf{yy}}^a \tag{2.22}$$

2.2 Generation and characterization of 3D point clouds

3D point clouds are considered the basic data for the change detection and verification approaches of this thesis. There are mainly two sources for 3D point clouds, namely laser scanning, which is an active measurement technique, and passive image-based dense matching. Both types of 3D point clouds have individual characteristics, especially in close range indoor applications, that have to be considered during analysis and evaluation.

---

[*] $\sigma_{x'}^a = \sigma_{y'}^a = 1 \, pixel$

[†] $\sigma_X^a = \sigma_Y^a = \sigma_Z^a = 15 \, mm$

Table 2.1: Sources of error of a laser scanner and their effects in close-range applications using the example of a Z+F Imager 5016® (`https://www.zofre.de/`)

Source	**Error/ effect**
Range noise	0.25 mm rms
Beam divergence	≈ 3.5 mm @ 1 m
Range resolution	0.1 mm
Linearity error	≤ 1 mm + 10 ppm
Deflection vertical accuracy	0.004°
Deflection horizontal accuracy	0.004°

2.2.1 Terrestrial laser scanning

Terrestrial laser scanning (TLS) is commonly used for indoor scene documentation as it is not as sensitive to a limited range of sensor motion and constraint viewing conditions as passive, image based techniques usually are. Nevertheless, the quality of TLS point clouds does also suffer from this "indoor conditions". The surface of an object is scanned in a certain pattern when using TLS. The density of the resulting 3D point cloud depends on the pre-defined angular resolution and the distance between the scanning device and the object to be measured. A common point-to-point distance is 6 mm at 10 m. Due to constraint geometric conditions in a buildings interior, the average point-to-point density highly varies within the 3D point cloud of a single 360° scan.

There are some typical basic error sources on TLS measurements which are related to the scanning device (Tab. 2.1) and the quality of point cloud registration but there are also some that are more difficult to assess and are very individual, such as reflectivity depending on surface material, angle of incidence of the incoming laser beam and even meteorological effects [Wujanz et al., 2018]. However, for geodetic applications related to civil engineering and construction, the magnitude of systematic deviations and according measurement uncertainty can be assessed by following the Guide to the Expression of Uncertainty in Measurement (GUM) [ISO, 2008], as for example estimated and described by Koch [2008] for a deformation analyses of motorways based on TLS.

2.2.2 Dense image matching

For reasons of efficiency realistic 3D modeling for BIM is based on 3D point clouds rather than on discretely measured individual points. There exist two types of image based 3D point clouds. Type 1 is composed of tie points, which result from the application of an interest operator that automatically detects pixel correspondences in overlapping images for triangulation. Tie point coordinates and associated accuracies are estimated via the bundle adjustment procedure (Sec. 2.1.2 and 2.1.3). Many photogrammetric software relies on Scale Invariant Feature Transform (SIFT) for automatic tie point generation prior to image orientation. The number and spatial distribution of TPs cannot be controlled directly. Rather, their successful generation largely depends on the degree of overlap between images, the lighting conditions and object textures in the scene. Therefore, quality and quantity of TPs can be quite heterogeneous in close range applications. As there are usually several hundreds up to thousands TPs per image pair, in their entirety, 3D TP's coordinates are also referred to as a *sparse cloud*.

Point cloud type 2 is considered a *dense cloud*. It results from a dense image matching method that aims to reveal comprehensive pixel-to-pixel correspondences in order to derive depth values per pixel and thus an image-based dense 3D point cloud. After image orientation from bundle adjustment, dense matching is applied on rectified images where the epipolar lines exactly correspond with pixel rows to reduce the search space for matching pixel pairs. 3D point coordinates are calculated from the disparity, which is the distance in pixel of one image point in an image from another. A commonly implemented dense matching algorithm is Semi Global Matching (SGM), which approximates a global optimization of matching costs along several 1-dimensional path directions thru images, also across the epipolar line [Hirschmüller, 2008]. Due to weak texture areas and occlusions, resulting depth maps are usually error prone. Therefore, consistency checks based on redundant information from multiple images, smoothness constraints and distance weighted interpolation of gaps are necessarily applied in the phase of post-processing. Due to the different ways of generating the photogrammetric 3D point clouds of type 1 and 2, different analysis and evaluation strategies are to be chosen in further processing steps.

2.3 Evidence based reasoning according to Dempster and Shafer

Dempster-Shafer Theory (DST) [Shafer, 1976] uses *belief*, indicated by a number between zero and one, rather than *probability*. It is a mathematical theory of evidence and a theory of probable reasoning that deals with weights of evidence and with numerical degrees of support based on evidence. In accordance with Bayesian probability theory, a number between zero an one indicates the degree of support a body of evidence provides for a proposition. If a part of belief is confessed to a hypothesis in Bayesian theory, the rest must be assigned to its corresponding negation. A portion of belief that is tied to a proposition is thus also tied to every other proposition that it implies. At this point DST differs in the way that there is no such limiting constraint. Instead, DST focuses on the combination of degrees of belief, which are based on bodies of evidence with those based on entirely distinct bodies of evidence. This combination is effected by Dempster's rule [Shafer, 1976].
The advantage of DST is relative flexibility as vague states may exist and ignorance is explicitly measured, which requires an unknown state to exist for the calculation. When using DST, uncertainty is modeled by belief functions, quantifying belief masses and the combination of belief for evidence based reasoning.

The theory formally begins with a set of possible events Θ, also referred to as *frame of discernment*. A hypothesis is a subset $A \subseteq \Theta$ and the power set $\mathcal{P}(\Theta)$ denotes the set of all subsets of Θ. If $\Theta = \{a, b\}$ then $\mathcal{P}(\Theta) = \{\emptyset, \{a\}, \{b\}\{\Theta\}\}$.

A function is called a *mass function* or *basic probability assignment* whenever $m(0) = \emptyset$ and

$$\sum_{A \in \mathcal{P}(\Theta)} m(A) = 1 \tag{2.23}$$

Therefore, m is a mapping $m : \mathcal{P}(\Theta) \rightarrow [0; 1]$ and called *normalized* [Reineking, 2014].

Given several belief functions over the same frame of discernment Θ but based on distinct bodies of evidence, a new belief function based on the combined evidence can be computed with Dempster's rule of combination: $m_{1 \oplus 2} = m_1 \oplus m_2$ [Dempster, 1976].

Let m_1 and m_2 be two basic probability assignments associated with belief functions over Θ and let A_i denote focal elements of m_1 while B_j those of m_2. The joint mass resulting in hypothesis C is obtained from:

$$m_{1,2}(C) = \frac{\sum_{A_i \cap B_j = C} m_1(A_i)\, m_2(B_j)}{1 - k} \tag{2.24}$$

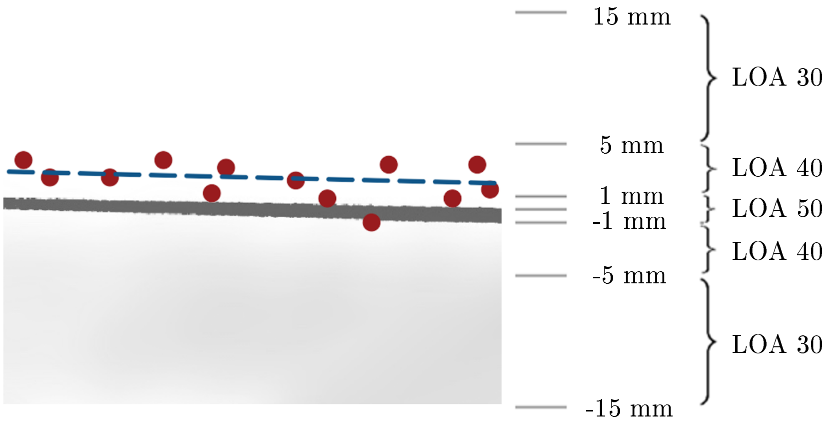

Figure 2.1: The Level of accuracy specification: The geometric accuracy of an as-built model depends on both, the accuracy of measurement (red dots) and the degree of generalization in the modeling process (blue dotted line). The degree of correspondence between the real object surface and the model is expressed by the project specific Level of Accuracy (LOA).

where

$$k = \sum_{A_i \cap B_j = \emptyset} m_1(A_i)\, m_2(B_j) \tag{2.25}$$

is the conflict degree, also called normalization constant. This constant tends towards 1 when belief functions are defined over sets of hypotheses that contradict each other.

Dempster's rule is a rule for combining a pair of belief functions, but by repeatedly applying it, it can be used to combine any number of belief functions. The operation $\oplus$ is commutative and associative.

$$\begin{aligned} &m_1 \oplus m_2, \\ &(m_1 \oplus m_2) \oplus m_3, \\ &((m_1 \oplus m_2) \oplus m_3) \oplus m_4, \\ &\ldots \end{aligned}$$

2.4 As-built documentation for BIM

It is a common practice to represent building objects in a geometrically generalized and orthogonal fashion, although of course real world existing conditions are seldom perfectly homogeneous and orthogonal. Design software packages are limited in their ability to represent real world conditions, especially with BIM compliance. Additionally, maximum realistic modeling is commonly associated with too high effort. Even if a BIM is considered to come with as-built geometry, error is introduced because real world conditions are usually represented in a more or less generalized and simplified fashion.

The U.S. Institute of Building Documentation (USIBD) provides the Level of Accuracy specification (LOA) in order to specify the accuracy and means by which to represent and document existing building conditions in context of BIM. Knowing reliably as-built conditions is important when dealing with analyzable building models and metric tolerance requirements. Generally, in construction, tolerances (T) specify allowable variations of materials, components, systems, installation techniques, buildings types etc. to ensure for example that neighboring component

Table 2.2: The Level of Accuracy according to the U.S. Institute of Building Documentation [USIBD, 2019]

Level	Lower range	Upper range
LOA 10	5 cm	15 cm
LOA 20	15 mm	5 cm
LOA 30	5 mm	15 mm
LOA 40	1 mm	5 mm
LOA 50	0 mm	1 mm

elements really do fit together when installed on site, e.g. flatness deviation of a surface. In order to prove compliance with metric tolerances of individual components, the confidence interval of the measurement should be significantly smaller than the specified tolerance of the object to be tested: $\sigma \leq T/15$ [Witte et al., 2020]. The LOA, on the other hand, refer to the acceptable tolerance range for the building measurements acquired during the "scan-to-BIM" acquisition process, and the tolerance range for the representation of these measurements in the model (Fig. 2.1 and Tab. 2.2). The LOA specification not only takes up common measurement accuracy standards (DIN 18710), but especially provides detailed guidance on the representation, modeling and verification of as-built measurement data and refers to a sensor accuracy of $\sigma \leq T/5$ assuming a confidence bound of 95%. There are five LOA, specified at the 95 confidence level ($2\,\sigma$). A LOA either relates to the measurement (e.g. TLS) or to the model accuracy (also referred to as "represented accuracy"). The LOA are especially important for detecting and evaluating changes when it comes to a comparison of LOA compliant model and its represented surface and captured as-built data, e.g. 3D point clouds.

3 Image-to-BIM co-registration

Photogrammetric applications can meet general requirements of accuracy and efficiency and therefore, are becoming more and more popular for visual localization and 3D data generation for building documentation. A camera's orientation is required in order to determine the spatial correspondence between an image and a 3D model (Fig. 3.1). However, the estimation of a camera's pose within a BIM's reference system is indoors much more difficult than outdoors. The lack of direct geo-referencing as a result of signal shading as well as occlusions and ambiguities due to general indoor structures are challenging circumstances for image based measurements within a building's interior and related accuracy requirements. This chapter presents an estimation model for camera pose refinement based on straight line references [Meyer et al., 2021], given a coarse orientation, e.g. from sensors of the Inertial Measurement Unit (IMU) and visual odometry. The stochastic model includes the individual uncertainty information of BIM related objects according to the Level of Accuracy specification for BIM [USIBD, 2019]. The approach is supposed to support future developments of image based change detection in indoor environments with available BIM. In line with compliance checking for BIM, the focus here is on structural and topological changes to the geometry of BIM-compliant 3D models.


(a) (b)

Figure 3.1: Image sequence within a BIM environment: a) image orientation with respect to a BIM's reference system, b) image overlayed with BIM

3.1 Concept of image-based co-registration and change detection for BIM

For an overall image based indoor change detection application a camera or stereo camera system with an IMU shall be used to obtain the relative orientation, an image based 3D point cloud by SfM and Multi View Stereo (MVS) and optionally the model scale. Indoor environments can be

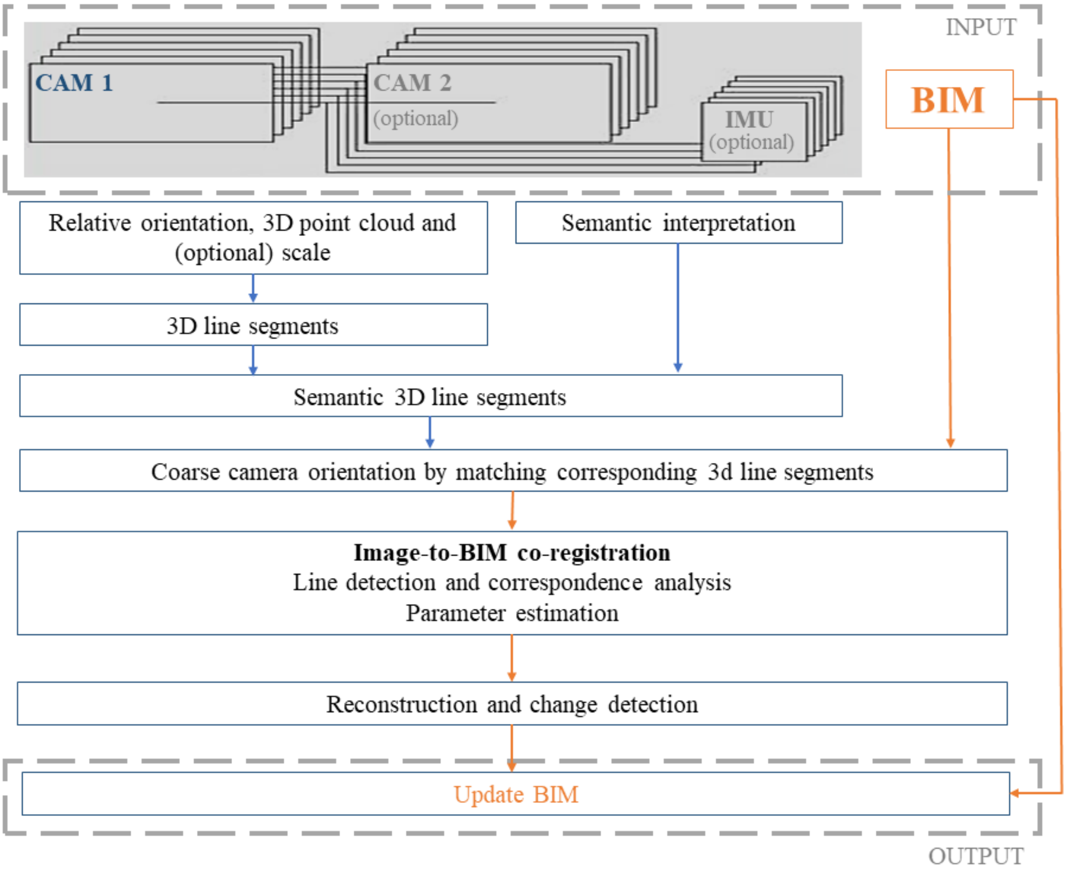

Figure 3.2: Concept of image-to-BIM co-registration for change detection for BIM

characterized by their large number of straight edges e.g. on windows, door, walls and furniture. 3D lines as geometric primitives can be used to describe the building interior in an abstract way. This brings advantages over unstructured 3D point clouds in terms of matching an co-registration with a corresponding 3D model. Therefore, the approach presented by Hofer et al. [2015] shall be integrated in the process in order to generate an abstract 3D line model. With the results of a semantic segmentation, detected an extracted 3D lines will be further enriched with semantic information. This approach is similar to what is described by Iwaszczuk et al. [2012]. The coarse absolute orientation of an image sequence in the BIM's reference system will be determined from matching corresponding 3D line segments. 3D scene reconstruction shall also be supported by the available BIM information in an object based procedure. Finally, the change detection can be realized by the comparison with last version of the BIM before it is updated with the new information. Altogether, this procedure is supposed to result in a positive feedback loop because the higher the quality of the initial BIM, the faster and more precisely it can be updated again. The overall concept is depicted in Fig. 3.2.

3.2 Feature extraction

Line features usually serve well as geodetic references in indoor scenes in order to estimate a camera's pose with respect to a superior coordinate system. They are sufficiently available in man-made environments and corresponding models and can be detected easily by common image processing algorithms.

3.2.1 Straight line detection

For image-to-BIM co-registration, corresponding line features are to be uncovered. As a preprocessing step, image pixels on edges are identified using the Canny Edge detector [Canny, 1986]. Using the Sobel operator, the algorithm provides boundaries of image areas with different intensities. For each pixel, the gradient is calculated from the magnitude of the partial derivatives in X and Y. High gradient values represent strong edges.

$$G(x,y) = \sqrt{g_x(x,y)^2 + g_y(x,y)^2} \tag{3.1}$$

The number and quality of detected elements varies with the minimum edge strength. It acts as a threshold to discard weak edge pixels with too little contrast and must be set specifically for the respective circumstances, such as individual room equipment, camera parameters, shooting perspective, lighting situation, etc. The actual line segments are estimated from the Hough transformation [Hough, 1962]. They are represented as straight lines in the Hessian normal form:

$$r = x\, cos\, \theta + y\, sin\, \theta \tag{3.2}$$

θ is the angle between the normal of the straight line and the x-axis, r is the distance from the origin to the plumb bob. θ and r span a two-dimensional parameter space. For each x and y of the previously detected edge pixels, r is computed in a quantized range $0 < \theta < 2\pi$, resulting in a sinusoidal curve in parameter space for each pixel. When multiple pixels lie on a common straight line, their curves intersect at a point. In Hough accumulation, each intersection is entered as a frequency point in a voting matrix. The more curves pass a point (θ, r), the more likely it is a distinct line in the image. Not all detected line segments are suitable for input into the correspondence analysis. Especially short segments are suspicious, which are often caused by interfering objects in the scene and image noise. To identify „good“ features and discard „bad“ ones, the line segments can be analyzed and weighted e.g. as in Iwaszczuk & Stilla [2017] with

$$g_i = \frac{1}{2}\left(\frac{l_i}{d_{max}} + \frac{a_i}{255}\right) \tag{3.3}$$

g_i represents the weight of the i-th line in the image, l_i represents the length of the i-th line, $a_i \in [0, 255]$ denotes the threshold value of the minimum edge strength used for the extraction of the i-th line, and d_{max} is the length of the image diagonal.

3.2.2 Uncertain BIM edges

BIMs are assigned to different expansion stages and while there are planning models from the phase of early conceptual design to detailed fabrication, those that come with as-built geometry are most sophisticated. As-built BIMs are commonly challenging because these models require a 3D capture of the real scene and subsequently a careful BIM compliant modeling that is based on the obtained 3D data. Building edges are never perfectly built as planned, often geometrically generalized for BIM-compliant representation and errors can occur during both measurement and modeling. As a result, line correspondences for image-to-BIM co-registration must be considered statistically uncertain entities as this is essential for dealing with metric confidences in the field of civil engineering and BIM.

In the following, extracted edges from BIM related objects such as walls, ceilings, windows and doors are enriched with individual uncertainty information. Although the information on the statistical geometric uncertainties can theoretically come from any source, in case of doubt it is advisable to refer to the LOA specification as introduced Sec. 2.4.

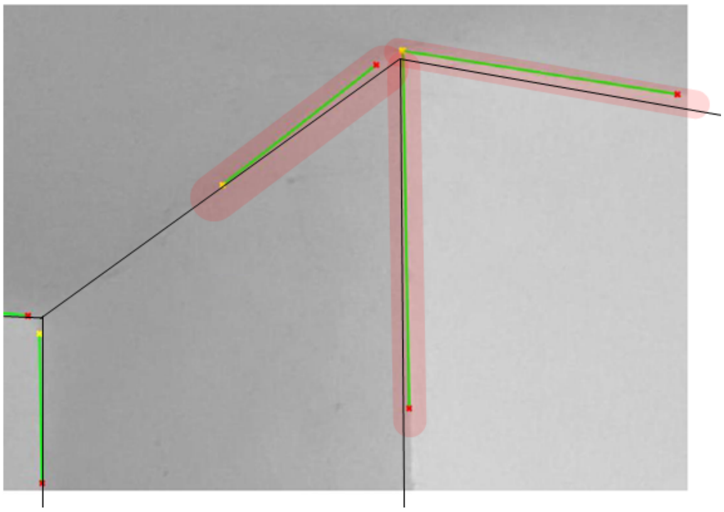

Figure 3.3: Statistically uncertain model edges: A real image of an indoor scene with detected uncertain straight lines (green lines and transparent red areas) overlayed with model edges (black lines) from the BIM

3.3 Constraint estimation based on Gauss-Helmert model

The exterior orientation parameters of a monocular camera $(X_0, Y_0, Z_0, \omega, \phi, \kappa)$ are implicitly available in the projection matrix P. The approximate projection matrix gets optimized in the BIM's reference system through the observation of straight lines in the image $(\mathbf{l}_i)$ and corresponding 3D model edges $(\mathbf{L}_i)$. The incidence condition of corresponding line features is used as input for the formulation of a functional model within a generic estimation model for homogeneous entities according to Meidow et al. [2009].

3.3.1 Functional model

The estimation is based on a Gauss Helmert model with constraints. The corrected observations $(\hat{\mathbf{y}} = \mathbf{y} + \hat{\mathbf{v}})$ and the estimated unknown parameters $(\hat{\boldsymbol{\beta}})$ have to fulfill certain conditions. The G-conditions $\mathbf{g}(\hat{\mathbf{y}}, \hat{\boldsymbol{\beta}}) = 0$ describe the relation between the observations and the parameters. The H-restrictions $\mathbf{h}(\hat{\boldsymbol{\beta}}) = 0$ concern only the parameters and the C-constraints $\mathbf{c}(\hat{\mathbf{y}}) = 0$ are imposed on the observations alone. The incidence condition of a 3D model edge, which is projected into the image with an observed corresponding straight line in the image serves as G-condition. It represents two independent constraints [Förstner & Wrobel, 2016]:

$$\Gamma(\mathbf{L})\, \mathrm{P}^T\, \mathbf{l} = \mathbf{0} \tag{3.4}$$

where $\mathbf{0}$ is a 4 x 1 zero vector.

For the handling of singular covariance matrices, the homogeneous observation entities as well as the parameters must be spherically normalized (normalized to 1). Therefore, the H-restrictions for the parameters is:

$$\mathbf{p}^T \mathbf{p} - 1 = 0 \tag{3.5}$$

where $\mathbf{p} = \mathrm{vec}(\mathrm{P})$, a column vector with the reshaped elements of P.

Respectively the C-constraints for the observations result in:

$$\mathbf{l}_j^T\mathbf{l}_j - 1 = 0 \tag{3.6}$$

$$\mathbf{X}_i^T\mathbf{X}_i - 1 = 0 \tag{3.7}$$

$$\mathbf{Y}_i^T\mathbf{Y}_i - 1 = 0 \tag{3.8}$$

The optimal solution for $\boldsymbol{\beta}$ is given by the minimum of the weighted squared residuals subject to the given constraints. This is achieved by minimizing the Lagrange function with the Lagrangian vectors $\boldsymbol{\lambda}, \boldsymbol{\mu}$ and $\boldsymbol{\nu}$:

$$L = \frac{1}{2}\hat{\boldsymbol{v}}^T\, \boldsymbol{\Sigma}_{\mathrm{yy}}^{+}\, \hat{\boldsymbol{v}} + \boldsymbol{\lambda}^T\mathbf{g}(\mathbf{y}+\hat{\boldsymbol{v}},\hat{\boldsymbol{\beta}}) + \boldsymbol{\mu}^T\mathbf{h}(\hat{\boldsymbol{\beta}}) + \boldsymbol{\nu}_1^T\mathbf{c}_1(\mathbf{y}+\hat{\boldsymbol{v}}) + \boldsymbol{\nu}_2^T\mathbf{c}_2(\mathbf{y}+\hat{\boldsymbol{v}}) + \boldsymbol{\nu}_3^T\mathbf{c}_3(\mathbf{y}+\hat{\boldsymbol{v}}) \tag{3.9}$$

The corrections for the observations and parameters are calculated in an iterative procedure according to Meidow et al. [2009]. In every iteration, the Jacobians are calculated:

$$\mathbf{A} = \frac{\partial\mathbf{g}(\mathbf{y},\boldsymbol{\beta})}{\partial\boldsymbol{\beta}}, \mathbf{B}^T = \frac{\partial\mathbf{g}(\mathbf{y},\boldsymbol{\beta})}{\partial\mathbf{y}}, \mathbf{C}^T = \frac{\partial\mathbf{c}(\mathbf{y})}{\partial\mathbf{y}}, \mathbf{H}^T = \frac{\partial\mathbf{h}(\boldsymbol{\beta})}{\partial\boldsymbol{\beta}}$$

Additionally, in every iteration (τ) the residuals of the constraints and the auxiliary variable $\mathbf{a}$:

$$\mathbf{g}_\tau = \mathbf{g}(\mathbf{y}^{(\tau)},\boldsymbol{\beta}^{(\tau)}), \quad \mathbf{h}_\tau = \mathbf{h}(\boldsymbol{\beta}^{(\tau)}), \quad \mathbf{c}_\tau = \mathbf{c}(\mathbf{c}^{(\tau)})$$

$$\mathbf{a} = \mathbf{B}^T\mathbf{C}(\mathbf{C}^T\mathbf{C})^{-1}(\mathbf{C}^T(\mathbf{y}-\mathbf{y}^{(\tau)})+\mathbf{c}_\tau) - \mathbf{B}^T(\mathbf{y}-\mathbf{y}^{(\tau)}) - \mathbf{g}_\tau$$

The normal equation system is solved by using $\mathbf{a}$ and matrix LU decomposition in order to receive the corrections for the estimated parameters:

$$\begin{bmatrix} \mathbf{A}^T\boldsymbol{\Sigma}_{\mathbf{gg}}^{-1}\mathbf{A} & \mathbf{H} \\ \mathbf{H}^T & \mathbf{0} \end{bmatrix} \begin{bmatrix} \widehat{\Delta\boldsymbol{\beta}} \\ \boldsymbol{\mu} \end{bmatrix} = \begin{bmatrix} \mathbf{A}^T\boldsymbol{\Sigma}_{\mathbf{gg}}^{-1}\mathbf{a} \\ -\mathbf{h}_\tau \end{bmatrix} \tag{3.10}$$

With the covariance matrix of the contradictions: $\boldsymbol{\Sigma}_{\mathbf{gg}} = \mathbf{B}^T\boldsymbol{\Sigma}_{\mathbf{yy}}\mathbf{B}$. Finally, the residuals:

$$\hat{\boldsymbol{v}}^{(\tau)} = -\boldsymbol{\Sigma}_{\mathbf{yy}}\mathbf{B}\boldsymbol{\lambda} - \mathbf{C}(\mathbf{C}^T\mathbf{C})^{-1}(\mathbf{C}^T(\mathbf{y}-\mathbf{y}^{(\tau)})+\mathbf{c}_\tau) \tag{3.11}$$

with:

$$\boldsymbol{\lambda} = \boldsymbol{\Sigma}_{\mathbf{gg}}^{-1}(\mathbf{A}\widehat{\Delta\boldsymbol{\beta}} - \mathbf{a}) \tag{3.12}$$

3.3.2 Stochastical model

The limited accuracy of the reference lines such as the inherent uncertainty of straight line detection have to be considered in the estimation. The homogeneous representations of 2D and 3D lines are therefore extended with individual stochastic information using covariance matrices.

A 3D point with Euclidean coordinates $X = [X, Y, Z]^T$ has the Euclidean covariance matrix:

$$\Sigma_{XX} = \begin{bmatrix} \sigma_X^2 & \sigma_{XY} & \sigma_{XZ} \\ \sigma_{XY} & \sigma_Y^2 & \sigma_{YZ} \\ \sigma_{XZ} & \sigma_{YZ} & \sigma_Z^2 \end{bmatrix} \tag{3.13}$$

The homogeneous representation of a 3D point $X \rightarrow \mathbf{X}$ is:

$$\mathbf{X} = [X_E, X_h]^T = [U, V, W, T]^T = [\lambda X, \lambda Y, \lambda Z, \lambda]^T \tag{3.14}$$

where $X_E = [U,V,W]^T$ is the Euclidean and $X_h = T$ is the homogeneous part. It follows the homogeneous covariance matrix $\Sigma_{\mathbf{XX}}$:

$$\Sigma_{\mathbf{XX}} = \lambda^2 \begin{bmatrix} \sigma_X^2 & \sigma_{XY} & \sigma_{XZ} & 0 \\ \sigma_{XY} & \sigma_Y^2 & \sigma_{YZ} & 0 \\ \sigma_{XZ} & \sigma_{YZ} & \sigma_Z^2 & 0 \\ 0 & 0 & 0 & 0 \end{bmatrix} = \lambda^2 \begin{bmatrix} \Sigma_{XX} & \mathbf{0} \\ \mathbf{0}^T & 0 \end{bmatrix} \tag{3.15}$$

For converting a homogeneous vector back in a Euclidean representation $\mathbf{X} \rightarrow \mathbf{X}^e$, the Jacobian J^e at $\mathbf{X}$ is needed, as the normalization is a non-linear function:

$$\mathbf{X}^e = \frac{\mathbf{X}}{X_h} = \begin{bmatrix} X \\ 1 \end{bmatrix} \tag{3.16}$$

$$J^e(\mathbf{X}) = \frac{1}{X_h} \begin{bmatrix} I_3 & -\frac{1}{X_h} X_E \\ \mathbf{0}^T & 0 \end{bmatrix} \tag{3.17}$$

$$\Sigma_{\mathbf{X}^e\mathbf{X}^e} = J^e(\mathbf{X})\, \Sigma_{\mathbf{XX}}\, J^e(\mathbf{X})^T \tag{3.18}$$

A two dimensional straight line with the homogeneous vector $\mathbf{l} = [a,b,c]^T$ has the homogeneous covariance matrix $\Sigma_{\mathbf{ll}}$:

$$\Sigma_{\mathbf{ll}} = \begin{bmatrix} \sigma_a^2 & \sigma_{ab} & \sigma_{ac} \\ \sigma_{ab} & \sigma_b^2 & \sigma_{bc} \\ \sigma_{ac} & \sigma_{bc} & \sigma_c^2 \end{bmatrix} \tag{3.19}$$

If an uncertain straight line is given by its homogeneous parameters, the parameters of the Hessian form can be derived form: $((\mathbf{l}, \Sigma_{\mathbf{ll}}) \rightarrow ([\theta, r], \Sigma_{hh}))$

$$\begin{bmatrix} \theta \\ r \end{bmatrix} = \begin{bmatrix} \operatorname{arctan2}(b,a) \\ -\frac{c}{\sqrt{a^2+b^2}} \end{bmatrix} \tag{3.20}$$

The Jacobian J_{lh} is needed at $\mathbf{l}$:

$$J_{lh}(\mathbf{l}) = \frac{1}{s^3} \begin{bmatrix} -bs & as & 0 \\ ac & bc & -s^2 \end{bmatrix} \quad \text{with} \quad s = \sqrt{a^2+b^2} \tag{3.21}$$

The covariance matrix Σ_{hh} results from:

$$\Sigma_{hh} = J_{hl}(\mathbf{l})\, \Sigma_{\mathbf{ll}}\, J_{hl}(\mathbf{l})^T \tag{3.22}$$

3.3.3 Parameter estimation

For each pair of corresponding lines, the vector with the observations is

$$\mathbf{y} = [\mathbf{l}_i, \mathbf{X}_i, \mathbf{Y}_i, ...]^T \tag{3.23}$$

and the related covariances respectively

$$\boldsymbol{\Sigma}_{\mathbf{yy}} = Diag[\boldsymbol{\Sigma}_{\mathbf{l}_i\mathbf{l}_i}, \boldsymbol{\Sigma}_{\mathbf{X}_i\mathbf{X}_i}, \boldsymbol{\Sigma}_{\mathbf{Y}_i\mathbf{Y}_i}, ...] \tag{3.24}$$

The elements of P are as $\mathbf{p}$ in $\boldsymbol{\beta}$.

Conditioning

As the homogeneous entities relate to Euclidean BIM objects, their coordinates are expressed with respect to the BIM's reference coordinate system. A big difference between the Euclidean and the homogeneous part causes the calculation to be numerical instable, which is why conditioning as proposed by Förstner & Wrobel [2016] is applied:

$$\mathbf{x}_c = \mathrm{T}_{2D}\,\mathbf{x} \quad \text{and} \quad \mathbf{y}_c = \mathrm{T}_{2D}\,\mathbf{y} \tag{3.25}$$

For 2D points T_{2D} is composed with the centroid coordinates μ_x and μ_y and the maximum distance to the centroid s_{max}:

$$\mathrm{T}_{2D} = \begin{bmatrix} 1 & 0 & -\mu_x \\ 0 & 1 & -\mu_y \\ 0 & 0 & s_{max} \end{bmatrix} \tag{3.26}$$

The procedure is analogous to 3D points.

Straight lines are conditioned and re-conditioned using:

$$\mathbf{l}_c = \mathrm{L}_{2D}\,\mathbf{l} \tag{3.27}$$

$$\mathbf{l} = \mathrm{L}_{2D}^{-1}\mathbf{l}_c \;\text{ with }\; \mathrm{L}_{2D} = (\mathrm{T}_{2D}^{-1})^T \tag{3.28}$$

Conditioning is applied on the observations. For the projection matrix results:

$$\mathrm{P}_c = \mathrm{T}_{2D}\,\mathrm{P}\,\mathrm{T}_{3D}^{-1} \tag{3.29}$$

Spherical Normalization

According to (3.5) and (3.6) the observations and initial parameters have to be spherically normalized prior to the adjustment

$$\mathbf{l}_c^s := \mathbf{l}_c/|\mathbf{l}_c| \tag{3.30}$$

$$\Sigma_{\mathbf{ll}} = \mathrm{J}_c\,\Sigma_{\mathbf{ll}}\,\mathrm{J}_c^T \tag{3.31}$$

With the Jacobian J_c:

$$\mathrm{J}_c(\mathbf{l}) = \frac{1}{|\mathbf{l}_c|}\left(I_3 - \frac{\mathbf{l}_c\,\mathbf{l}_c^T}{\mathbf{l}_c^T\,\mathbf{l}_c}\right) \tag{3.32}$$

In the same way it is done for the parameters and 3D model points with:

$$\mathbf{X}_c^s := \mathbf{X}_c/|\mathbf{X}_c| \tag{3.33}$$

with

$$\Sigma_{\mathbf{XX}} = \mathrm{J}_c\,\Sigma_{\mathbf{XX}}\,\mathrm{J}_c^T \tag{3.34}$$

and

$$\mathbf{p}_c^s := \mathbf{p}_c/|\mathbf{p}_c| \tag{3.35}$$

In the following sections we assume the homogeneous coordinates to be conditioned and spherically normalized and omit the indices c and s.

Jacobians

The A-Matrix includes the first derivatives of the G-constraints according to the unknown parameters of $\mathbf{p}$. As eq. 3.4 corresponds to 4 constraints of which two are chosen, the matrix has as twice as many rows as observed line correspondences and the number of columns corresponds to the number of parameters:

$$\mathbf{A} = \left[\begin{pmatrix} \mathrm{x}_{1i} & 0 \\ 0 & \mathrm{x}_{2i} \end{pmatrix} \begin{pmatrix} \mathrm{l}_{1i}\,\mathbf{Y}_i^T & \mathrm{l}_{2i}\,\mathbf{Y}^T & \mathrm{l}_{3i}\,\mathbf{Y}^T \\ \mathrm{l}_{1i}\,\mathbf{Y}_i^T & \mathrm{l}_{2i}\,\mathbf{Y}^T & \mathrm{l}_{3i}\,\mathbf{Y}^T \end{pmatrix} - \begin{pmatrix} \mathrm{y}_{1i} & 0 \\ 0 & \mathrm{y}_{2i} \end{pmatrix} \begin{pmatrix} \mathrm{l}_{1i}\,\mathbf{X}_i^T & \mathrm{l}_{2i}\,\mathbf{X}^T & \mathrm{l}_{3i}\,\mathbf{X}^T \\ \mathrm{l}_{1i}\,\mathbf{X}_i^T & \mathrm{l}_{2i}\,\mathbf{X}^T & \mathrm{l}_{3i}\,\mathbf{X}^T \end{pmatrix}, \ldots \right]^T \tag{3.36}$$

The B-Matrix includes the first derivatives of the G-constraints (3.4) according to the observations $\mathbf{l}_i$, $\mathbf{X}_i$ and $\mathbf{Y}_i$. It is a diagonal matrix where each main diagonal element has 2 rows (2 constraints) in (3.4) and 11 columns (11 elements in the homogeneous vectors $\mathbf{l}$, $\mathbf{X}$ and $\mathbf{Y}$).

$$\mathbf{B} = \mathrm{diag}\big[\big((\mathbf{X}_i\,\mathbf{Y}_i^T - \mathbf{Y}_i\,\mathbf{X}_i^T)\,\mathrm{P}^T, \mathbf{Y}_i^T\,\mathrm{P}^T\,\mathbf{l}_i\,\mathrm{I} - \mathbf{Y}_i\,\mathbf{l}_i^T\,\mathrm{P}, \mathbf{X}_i\,\mathbf{l}_i^T\,\mathrm{P} - \mathbf{X}_i^T\,\mathrm{P}^T\,\mathbf{l}_i\,\mathrm{I}\big), \ldots\big] \tag{3.37}$$

The C-Matrix includes the first derivatives of the C-constraints (3.5) according to the observations $\mathbf{l}_i$, $\mathbf{X}_i$ and $\mathbf{Y}_i$. The derivatives for each observation triple form diagonal sub-matrices of dimension (3×11), which in turn are written to the main diagonal matrix.

$$\mathbf{C} = \mathrm{diag}\big[\mathrm{diag}[2\,\mathbf{l}_i^T, 2\,\mathbf{X}_i^T, 2\,\mathbf{Y}_i^T], \ldots\big] \tag{3.38}$$

The H-Matrix includes the first derivatives of the H-constraints according to $\mathbf{p}$. It has one row and 12 columns.

$$\mathbf{H} = [2\,\mathbf{p}^T] \tag{3.39}$$

3.4 Euclidean interpretation

The initial projection matrix is optimized during the adjustment. The homogeneous matrix as well as the uncertain observations in the form of 3D points and 2D straight lines, are thereby conditioned and spherically normalized. For the application of the results in engineering practice, the output data should be interpreted Euclidean. After the adjustment, an estimated projection matrix ($\hat{\mathrm{P}}_c^s$) is available, which is also conditioned and normalized. It is reconditioned with (3.29).

From the estimated projection matrix, the improved parameters of the exterior orientation can be derived by decomposing the matrix:

$$\mathrm{P} = [\mathrm{A}|a] = [\mathrm{K}\,\mathrm{R}| - \mathrm{K}\,\mathrm{R}\,X^0] \tag{3.40}$$

[Förstner & Wrobel, 2016].

The projection center X^0 is obtained from

$$X^0 = -\mathrm{A}^{-1}\,a \tag{3.41}$$

Factorizing A by QR decomposition, which expresses a matrix A as multiplication of an orthogonal matrix Q and an upper triangular matrix R, results in the rotation matrix R. A should have a positive determinant: $\bar{\mathrm{A}} = sign(|\mathrm{A}|)\,\mathrm{A}$. The inverse $\bar{\mathrm{A}}$ is decomposed:

$$[\bar{\mathrm{R}}^T, \bar{\mathrm{K}}^{-1}] = qr(\bar{\mathrm{A}}^{-1}) \tag{3.42}$$

The sign s (here: $s = +1$) of principal distance needs to be specified for the calculation of the diagonal matrix D:

$$\mathrm{D} = \mathrm{diag}(\mathrm{sign}(\mathrm{diag}(\mathrm{K})))\mathrm{diag}([s, s, +1])$$

Finally, the rotation matrix R results from: $\mathrm{R} = \mathrm{D}\,\bar{\mathrm{R}}$.

After the adjustment, Euclidean interpretation of uncertain, homogeneous, conditioned and spherically normalized 3D points and 2D lines is achieved through Euclidean normalization and re-conditioning.

	3D point	**2D line**
State after adjustment	$\mathbf{X}_c^s, \mathit{\Sigma}_{\mathbf{X}_c^s\mathbf{X}_c^s}$	$\mathbf{l}_c^s, \mathit{\Sigma}_{\mathbf{l}_c^s\mathbf{l}_c^s}$
1. Euclidean normalization	$\mathbf{X}_c, \mathit{\Sigma}_{\mathbf{X}_c\mathbf{X}_c}$ with $J^e(\mathbf{X}_c^s)$	$\mathbf{l}_c^e, \mathit{\Sigma}_{\mathbf{l}_c\mathbf{l}_c}$ with $J^e(\mathbf{l}_c^s)$
2. Re-conditioning	$\mathbf{X}, \mathit{\Sigma}_{\mathbf{XX}}$ with T_{3D}	$\mathbf{l}, \mathit{\Sigma}_{\mathbf{ll}}$ with L_{2D}
3. Euclidean interpretation	$\mathbf{X}^e, \mathit{\Sigma}_{\mathbf{X}^e\mathbf{X}^e}$ with $J^e(\mathbf{X})$	$[\theta,\, r]^T$, $\mathit{\Sigma}_{hh}$ with $J_{hl}(\mathbf{l})$

Table 3.1: Euclidean interpretation of uncertain 3D points and 2D lines

4 Construction progress documentation

Progress monitoring of construction projects is a challenging and rapidly growing field of activity for geodesists. This chapter is about a change detection method based on 3D point clouds and the discretization of the object space by voxels, specifically adapted here for indoor building applications [Meyer et al., 2022a,b]. The occupancy of voxel space is determined using point clouds from terrestrial laser scanning at different construction stages. By detecting occupancy conflicts between two measurement epochs, it is determined whether changes have occurred at a particular location.

4.1 High resolution occupancy modeling

Up to now, construction progress documentation has mostly been done by visual inspections and control measurements carried out by construction workers or by very time-consuming and cost-intensive professional surveys with total stations and leveling devices. For several years now, TLS has been a popular alternative for fast and high-resolution as-built surveys of construction sites, but this technique still lacks focused analysis procedures, computer-aided interpretation, and strategies for automated evaluation in engineering practice. Accordingly, the challenge with TLS is the interpretation of these massive 3D data sets with the goal of being able to make automated statements about detected changes. Particularly in interior construction, there are many detailed changes in the condition of building components. Therefore, the accuracy requirements are particularly high there. 3D point clouds of indoor scenes are characteristically dense and very detailed. This is due to the fact, that modern devices provide enormous measurement rates that enable the generation of up to millions of 3D points per second, and that the average scanner-object distance is indoors usually very short. For this reason, a high-resolution analysis based solely on voxels is aimed.

4.1.1 Discretization of terrestrial laser scanning point clouds

A voxel relates to a cell in a regular 3D grid and a voxel based approach inherently comes with the decision and acceptance of discretization of actually continuous data. Otherwise, a "voxelization" is applied in the phase of pre-processing to speed up spatial queries and to reduce the amount of data for sophisticated analysis in certain regions of interest, hence, serves a 3D index, e.g. for point-level applications such as presented in Chapter 5. If an application is supposed to work exclusively on voxel level, the chosen voxel size is crucial for its accuracy and level of detail. Figure 4.1 depicts the effects of different voxel sizes on the resolution in terms of sharpness of detail of the result.

In the context of change detection a 3D point cloud is transformed into a generalized and well structured voxel grid in order to infer knowledge about the occupancy of space. In the beginning

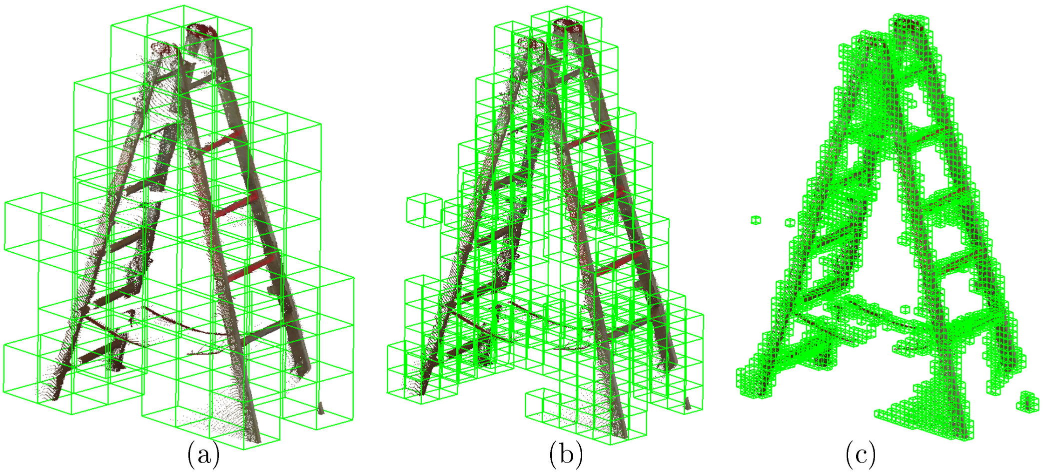

Figure 4.1: Resolution of a change detection application with respect to voxel size: a) 20 cm, b) 10 cm, c) 2.5 cm

the voxel space V is initiated i.e. the entire 3D space of the study site is tiled and resampled according to the specified voxel size. Every 3D point is assigned to its corresponding grid cell. In contrast to an octree based discretization, the actual distribution and cluster of 3D points is not taken into account at this initial step. Every 3D point votes for occupied space in its associated voxel. The more 3D points located within a voxel the higher the indication of real occupancy. A threshold should be found for a final decision through binarization, i.e. *not occupied* (0) or *occupied* (1). This threshold highly depends on the point density. If a voxel only contains a limited number of 3D points e.g. only isolated points that appeared due to noise, it is not going to be labeled instead of erroneously indicating occupied space.

4.1.2 Indoor voxel classification

3D point clouds from laser scanning bring the advantage of additional knowledge about non-occupied space as the laser ray $\mathbf{r}$ obviously traverses empty space due to the fact that a laser point $\mathbf{p}$ only appears when the beam hits an object's surface. Starting from a scanner source $\mathbf{s}$ resp. its corresponding voxel $\mathbf{s}_V$, $\mathbf{r}_V$ traverses empty voxel until $\mathbf{p}_V$ is met, which is obviously occupied (Fig. 4.2). Given a start point and an end point Bresenham's line algorithm [Bresenham, 1965] approximates a straight line between these points, using only addition, subtraction and bit shift. In this way, all raster cells that are traversed by a laser range measurement are accordingly labeled. Voxel that are neither traversed nor occupied remain *unknown*. In this way, the states of non-occupied voxel can be distinguished into *empty* and *unknown* (Fig. 4.3).

From one single point cloud a lot of valuable spatial information about a scene is already derived. A second point cloud, which covers the same spatial extend enables even more analysis as it either confirms the initial assumptions about the occupancy of space or evokes a contradiction. There are two types of conflicts:

i A new ray $\overrightarrow{\mathbf{s}_{V2}\mathbf{p}_{V2}}$ traverses voxel which have previously been marked as occupied.

ii New points $\mathbf{p}_{V2}$ occur in voxel that have actually been labeled as empty in the first point cloud (Fig. 4.4).

A detection of changes from voxel results form the exposure and evaluation of such conflicts. Vanished points form conflict type i) indicate a demolition whereas ii) indicates new built elements

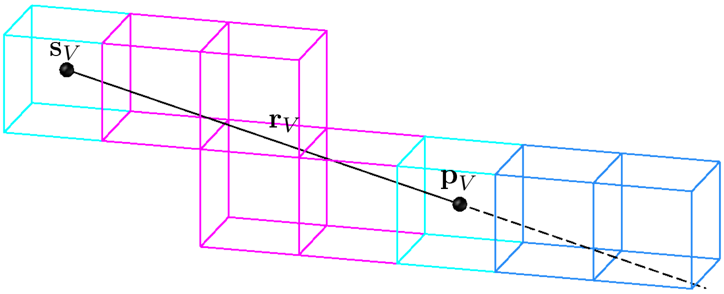

Figure 4.2: Principle of voxel space: Scanner source $\mathbf{s}_V$ and a laser point $\mathbf{p}_V$ in voxel space V. Voxel that are traversed by the laser ray $\mathbf{r}_V$ on its way from $\mathbf{s}_V$ to $\mathbf{p}_V$ are marked *empty* with magenta colored lines whereas *occupied* voxel are depicted cyan and occluded ones indicated as *unknown* in blue color.

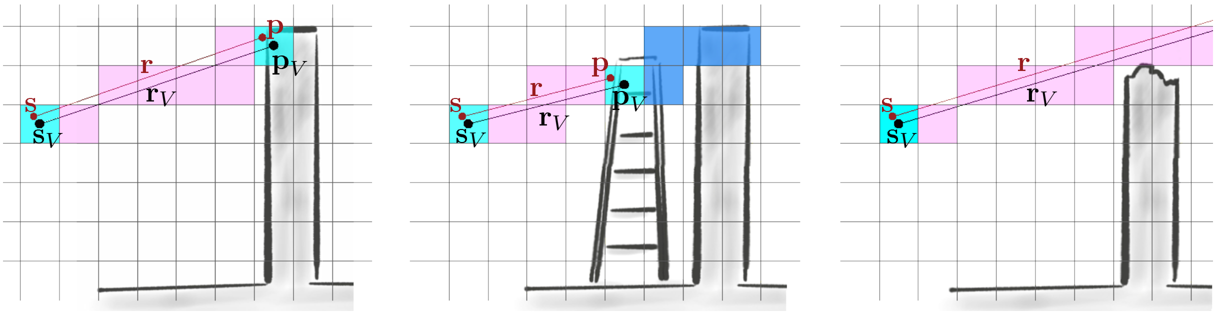

(a) (b) (c)

Figure 4.3: Principle of modeling the occupancy of space with voxel: Different scenarios can occur during acquisition: a) laser point on target object "wall", b) laser point on site equipment (ladder), c) no laser return on target object "wall" because of its demolition. The colored squares indicate the voxel states: cyan = *occupied*, magenta = *empty* and blue = *unknown*. There is always a discrepancy due to discretization between the actual measured beam (red) and the connection of source and target in voxel space (black).

or clutter, e. g. ladders or shovels. The result of this change detection approach is a voxel cloud consisting of the centroids of the labeled voxels.

The architectural condition inside buildings, especially during (re)construction, is generally a challenging environment for TLS. Confined spaces, strongly varying object distances and usually a lot of clutter and artifacts such as furniture and possibly construction site material cause low overlap of neighboring point clouds, gaps, occlusions, heterogeneous point densities and weak scanning geometries possibly resulting in small incident angles between measuring beam and object surface normal. The latter occurs in case the distance between scanner and object is too small (e. g. in a narrow, long hallway) and results not only in reduced measurement accuracy, but also incorrectly classified voxel for change detection. Small incidence angles result in occupied voxel also being traversed at the same time and, depending on the threshold, point density and voxel size, incorrectly classified as empty as depicted in Fig. 4.5. To avoid this effect, care should be taken to have a sufficient number of viewpoints during acquisition, a high point density and small voxel size respectively, and to pre-process the point clouds before further processing with a distance filter. This additional effort pays off in favor of an automated voxel based interpretation.

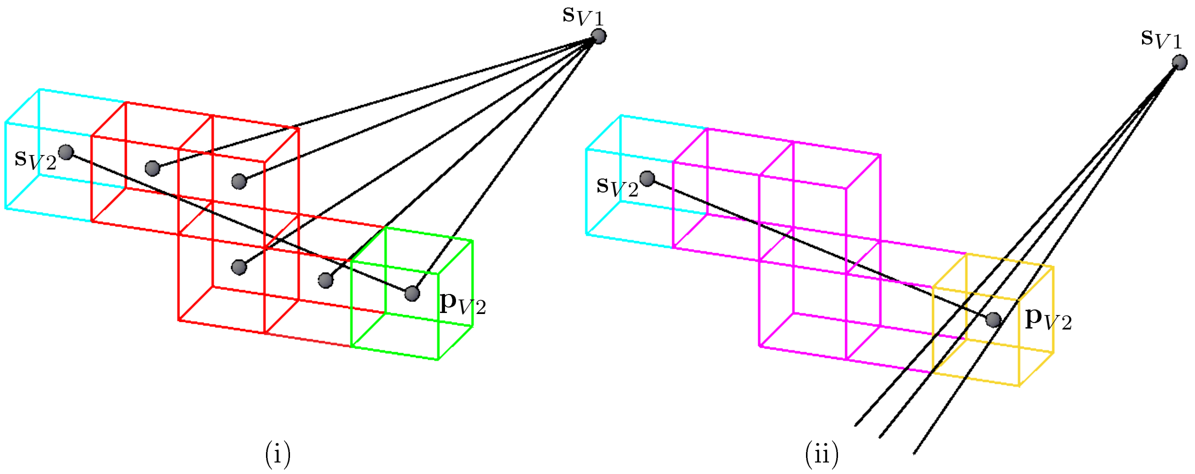

(i) (ii)

Figure 4.4: Conflicting occupancy of space from two epochs: i) *demolished* (red): new ray traverses voxel which have previously been marked as *occupied* ii) *new* (yellow): new point $\mathbf{p}_{V2}$ indicates occupancy whereas former voxel have been labeled as *empty*.

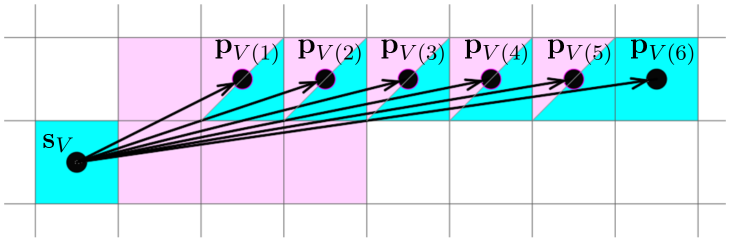

Figure 4.5: Effect of a low incidence angle of incoming laser rays on a flat surface: Occupied voxel also being traversed at the same time are incorrectly classified as empty and are therefore considered ambiguous.

4.1.3 Change detection given a BIM

The occupancy of space can not only be modeled from measurement data, e.g. 3D point clouds from different epochs, but can also be derived from a given BIM. The model then corresponds to the target occupancy and can thus be used not only for change detection but also for verification of the model in the course of progress documentation. In such an application, each measurement epoch would be compared against the BIM in order to recognize in an evaluation to what extent the situation already reflects the planned state (e.g. in a conversion project). For a comparison of one 3D point cloud with a model state, the BIM's geometry itself is also transferred into the voxel space V and discretized according to the target resolution in terms of voxel size.

The voxelization procedure is carried out in individual height layers. The layer thickness corresponds to the pre-defined voxel size. The model geometry, usually provided in the IFC format, is sliced and discretisized in order to result in a series of two-dimensional occupancy grids (Fig. 4.6). The comparison of point cloud vs. BIM has the advantage over the comparison of point cloud vs. point cloud that the occupancy of space from the BIM is volumetrically completely described, while the occupancy of space from two point clouds is usually incomplete and incomplete only in their overlap area and also only on the basis of the scanning on the object surface. In a complete occupancy model the interior of an object body, e.g., a wall, is also described, so that laser rays traversing the space indicate volumetrically complete truncation. This completeness is

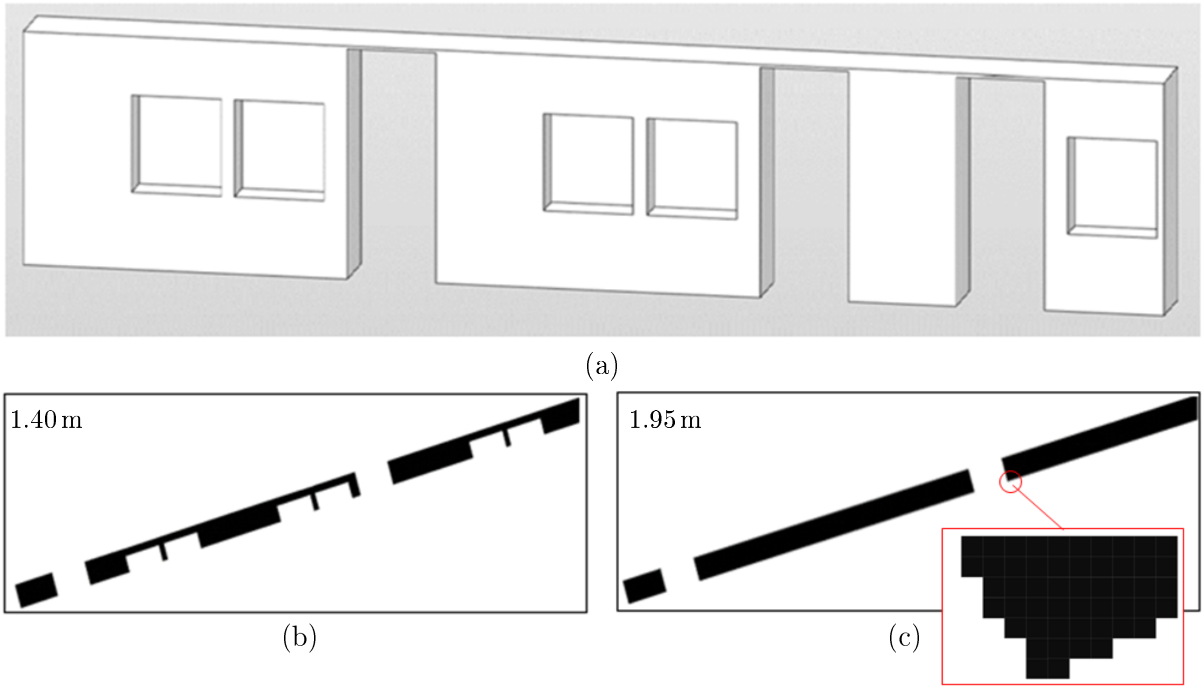

Figure 4.6: Modeling the occupancy of space from a given BIM: a) 3D visualization of a piece of wall with openings for doors and showcases as part of a BIM, b) Exemplary occupancy grid on 1.40 m above the floor level (black pixel indicate occupancy, whereas white areas indicate emptiness of space), c) Exemplary occupancy grid on 1.95 m above the floor level.

particularly valuable when classified voxels are used for spatial queries and operations in a spatial building database.

4.2 Accuracy discussion in context of BIM

In the course of voxel based modeling the occupancy of space from a TLS point cloud, an unavoidable discretization error occurs because all calculations and spatial queries refer to the voxel center and no longer to the original measured 3D points. The model of spatial occupancy is only an approximation of the real situation and varies depending on voxel size, origin and orientation of the voxel space (Fig. 4.7). Even if the original points would be labeled according to their assigned voxel class, the occupancy state would still refer to the assumption of a discretized model. Whether a voxel is labeled *empty*, *occupied* or *unknown* might change with a different initialization of the voxel space V. Depending on the voxel size and the individual density of the point cloud, the deviation of an actually generated 3D point from its voxel centroid is more or less significant. Additionally, as the geometric effect of a discretization by voxel also depends on the location and shape of the target object itself, the exact discretization error for every individual 3D point can only be predicted to a limited extend. However, the maximum point shift error d is:

$$d = \frac{\sqrt{3}\,a}{2} \tag{4.1}$$

where a is the voxel size, i.e. the length of the side of the regular 3D grid cell.

The discretization error, together with the error influences of TLS, must conform to the construction project's requirements in the individual case. With reference to the LOA specification

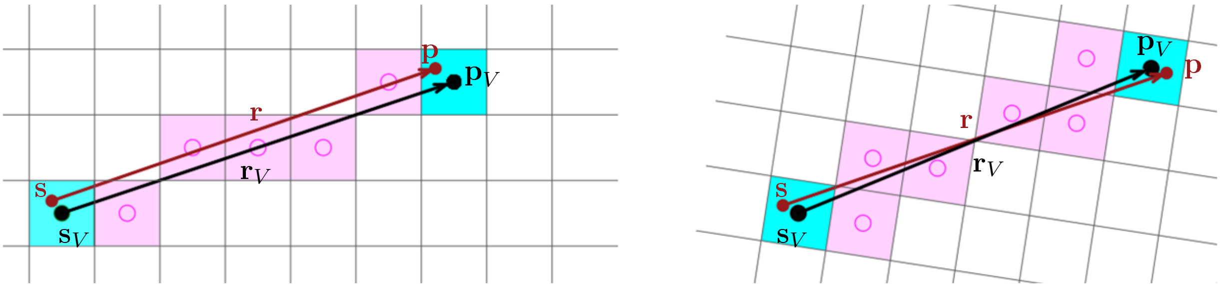

(a) (b)

Figure 4.7: Effect of differently initalized voxel spaces: $\mathbf{r}_V$ connects $\mathbf{s}_V$ and $\mathbf{p}_V$ in voxel space (black) while $\mathbf{r}$ represents the actual laser measurement from $\mathbf{s}$ to $\mathbf{p}$ (red): a) Voxel based of the occupancy of space, b) Voxel based modeling of the occupancy of space using a differently initalized voxel space.

(Sec. 2.4), the requirements for the maximum permissible error of TLS and voxelization can be well estimated in advance. In the context of modeling a subsystem or single object, the correct description of its individual shape, independent of its absolute position in the building, can be far more important for many tasks. For example, the relative accuracy is crucial for the distance between two walls, while the positions of the walls within the building reference system can be described by the absolute accuracies. While the absolute accuracy of a measurement and an according model are easily to be assessed from Tab. 2.2, the specification document proposes two approaches for tolerance computation in case of relative measurements.

The squared approach is considered the standard method. It is assumed that the tolerance T is small with respect to the underlying nominal dimension and that the actual sizes are randomly distributed around the nominal value.

$$T = \sqrt{\sum_{i=1}^{n} T_i^2} \tag{4.2}$$

The linear approach to tolerance calculation is used for a kind of pessimistic extreme value calculation. It assumes that all or almost all deviations from the nominal value occur with either a positive or negative sign.

$$T = \sum_{i=1}^{n} \left| \frac{\partial y_i}{\partial x_i} \right| T_i \tag{4.3}$$

In the case of a distance calculation (object 1 and object 2), the upper and lower limits of the relative tolerance T range are obtained using the quadratic approach:

$$T_{dist} = \sqrt{T_1^2 + T_2^2} \tag{4.4}$$

And with the linear approach, which estimates the situation more pessimistically:

$$T_{dist} = T_1 + T_2 \tag{4.5}$$

[USIBD, 2019]

Assuming for a BIM object the distance between the measured points, the voxel centers, and the model is 5 mm or less, the modeling accuracy would still meet the requirements of LOA 40 (1-5 mm). Referring to Fig. 4.8, the distance between the models of object 1 and object 2 could

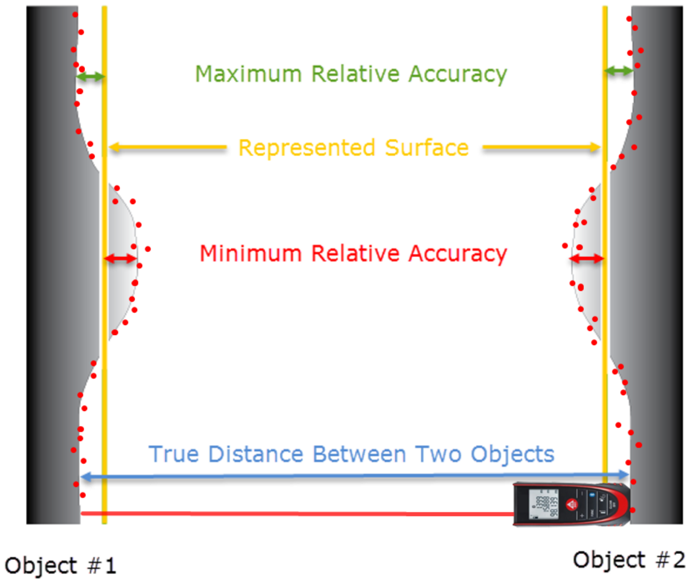

Figure 4.8: Relative accuracy between two BIM objects according to the LOA specification: The calculated distance and relative accuracy between two walls varies with the entity point cloud (red dots) or model (yellow lines). In this way, the relative accuracy of using voxels instead of points can also be estimated [USIBD, 2019].

be a maximum of 10 mm too long, or 10 mm too short, due to the absolute LOA 40 and a linear tolerance calculation. The relative distance accuracy would exceed the maximum permitted 5 mm of LOA 40 and would be in the range of LOA 30. To achieve LOA 40 for relative accuracy, an absolute modeling accuracy of LOA 50 would be required. When using a voxel approach for efficient construction progress documentation, it is important to pay attention to and agree with the client on the absolute and relative accuracies to be maintained.

5 Geometric BIM verification

This chapter focuses on the geometric verification of a given BIM from geodetic observations. Dempster-Shafer theory is used for the fusion and handling of uncertainties from laser range measurements and image rays with uncertainties related to the geometry of a given BIM (Fig. 5.1) [Meyer et al., 2022a,c]. The chapter includes a detailed insight in the mathematical and numerical formulation of appropriate belief functions for TLS measurements and image rays according to DST. In particular a separate treatment and weighting of the photogrammetric sparse cloud and the estimated dense cloud is proposed. Furthermore, it is shown how to apply Dempster's rule for combining bodies of evidence based on TLS and photogrammetric specific belief masses for final decision making.

5.1 Modeling the occupancy of space

A 3D point is actually a 0-dimensional entity and does not represent an object's surface directly as is it is not assigned any kind of spatial expression, e.g. a surface or a volume. However, a bunch of assumptions about the occupancy of space from 3D point clouds can be made, which usually consist of millions of individual 3D points. Laser range measurements and image based observations can be used to obtain belief masses about occupancy and emptiness of space and applying DST helps to find confirmation for either one of the hypothesis by the combination and fusion of multiple evidence from 3D point clouds.

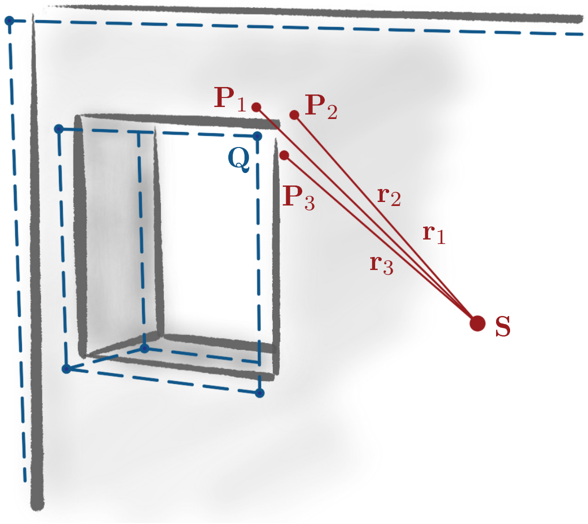

Figure 5.1: Principle of uncertain TLS point measures and uncertain BIM: Laser rays $\mathbf{r}_n$ and TLS points $\mathbf{P}_n$ on the true wall surface and the according BIM implied with an exemplary corner point $\mathbf{Q}$. Obviously, the model (blue dashed line) does not exactly fit the real world conditions. These inherent discrepancies must be considered in a point cloud based evaluation approach.

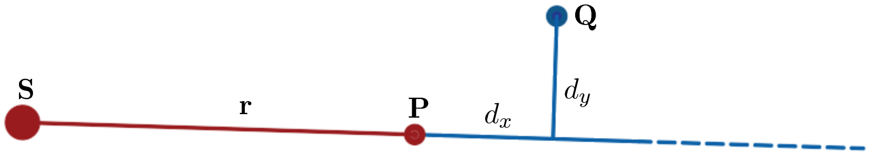

Figure 5.2: Impact of a single laser range measurement on the occupancy of space: The impact of a single laser range measurement from **S** to **P** on a query position **Q** is determined. In order to infer knowledge about either occupancy or emptiness at **Q**, the longitudinal distance d_x and transverse distance d_y from **P** to **Q** are to be calculated.

5.1.1 Belief from laser range measurements

According to Hebel et al. [2013] mass functions are used for modeling the occupancy of space from statistically uncertain laser range measurements. Obviously, a 3D point cloud from TLS provides a lot of information including evidence about the occupancy of space: It is assumed that the space along the laser ray **r** is empty while the space at the scanner source **S** and at a 3D point's location **P** are occupied. Anywhere else the occupancy remains unknown.

It is aimed to decide whether a query position **Q** in 3D space is occupied (occ) or empty (emp). As a result, the set of possible events is $\Theta = \{occ, emp\}$. In contrast to the Bayesian probability framework, the belief in a hypothesis and the belief in its complement can be less than 1. Therefore, belief functions provide an additional "dimension of uncertainty", which allows for making ignorance explicit. In the context of reasoning from TLS point clouds this brings the advantage that occlusions in the laser range measurement (e.g. caused by site equipment) are implicitly handled as they simply cause a lack of evidence instead of erroneously pointing to empty space at **Q**.

Although a point is 0-dimensional, hence does not cover an area in 3D space nor indicate any kind of occupancy directly, it can be associated with physical properties of the laser range measurement. Every 3D point **P** is assigned a spatial appearance reflecting the impact of typical error sources on TLS measurements according to Table 2.1. Furthermore, it can be assumed that the scanner resolution in indoor scenes (close range) results in a point density which allows for the assumption that there is no empty space between neighboring points, e.g. on a wall surface. Hence, the spatial extent of a point **P** should be modeled in accordance with the average point-to-point distance.

Hebel et al. [2013] suggested to define the impact of a laser range measurement $\mathbf{P} = \mathbf{S} + \mathbf{r}$ on a query position **Q** on the basis of the parameters d_x and d_y. The longitudinal distance of **Q** to **P** is represented by

$$d_x = (\mathbf{Q} - \mathbf{P}) \cdot \mathbf{r}_0 \qquad \text{where} \qquad \mathbf{r}_0 = ||\mathbf{r}|| \tag{5.1}$$

Similarly, d_y denotes the transverse distance **Q** to **P** (Fig. 5.2):

$$d_y = ||(\mathbf{Q} - \mathbf{P}) \times \mathbf{r}_0|| \tag{5.2}$$

The parameters d_x and d_y are used to define the following belief masses according to Hebel et al.

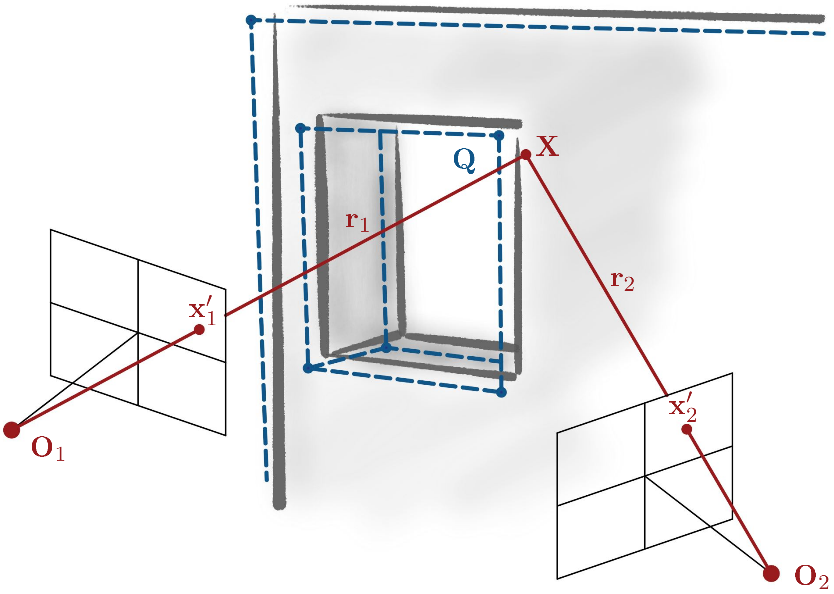

Figure 5.3: Photogrammetric observation of a BIM object: Two cameras with projection centers $\mathbf{O}_1$ and $\mathbf{O}_2$ map a 3D point $\mathbf{X}$ onto the image points $\mathbf{x}'_1$ and $\mathbf{x}'_2$. The according BIM (blue dashed line) is implied with an exemplary corner point $\mathbf{Q}$. The inherent discrepancies between the true wall surface (grey) and the model must be considered in a geometric verification pipeline.

[2013]:

$$m_{\mathbf{Q},\mathbf{P}}(0) = \emptyset \tag{5.3}$$

$$m_{\mathbf{Q},\mathbf{P}}(\{occ\}) = \left(1 - \frac{1}{e^{-\lambda\, d_x - c}}\right) \cdot e^{-\kappa\, d_y^2} \tag{5.4}$$

$$m_{\mathbf{Q},\mathbf{P}}(\{emp\}) = \left(\frac{1}{1 + e^{-\lambda\, d_x - c}} - \frac{1}{1 + e^{-\lambda\, d_x + c}}\right) \cdot e^{-\kappa\, d_y^2} \tag{5.5}$$

$$m_{\mathbf{Q},\mathbf{P}}(\Theta) = 1 - m_{\mathbf{Q},\mathbf{P}}(\{emp\}) - m_{\mathbf{Q},\mathbf{P}}(\{occ\}) \tag{5.6}$$

c: controls the longitudinal extend of occupied space at $\mathbf{Q}$.

λ: controls the gradual transition *empty* $\rightarrow$ *occupied* $\rightarrow$ *unknown*.

κ: controls the transverse extend of occupied space at $\mathbf{Q}$.

5.1.2 Belief from image rays

Assuming oriented cameras $(I_1, ..., I_n)$, forward intersection of image rays from different viewing positions results in 3D point coordinates $\mathbf{X}_n$ (Fig. 5.3). Every 3D measurement indicates the existence of a physical object as the space is obviously occupied at the intersection point $\mathbf{X}$. Furthermore, from the physical properties of the process of image creation, it can be assumed that the space along corresponding image rays $\mathbf{r}_n$ is empty. It can be further concluded that for arbitrary locations $\mathbf{Q}_n$ in the object space, one of the following states applies: *occupied (occ)*, *empty (emp)* or *unknown (U)*, where the latter indicates a lack of information, thus $\Theta = \{occ, emp\}$. This set of possible states corresponds to modeling the occupancy of space from TLS measurements (Sec. 5.1.1). It is depicted in Fig. 5.4.

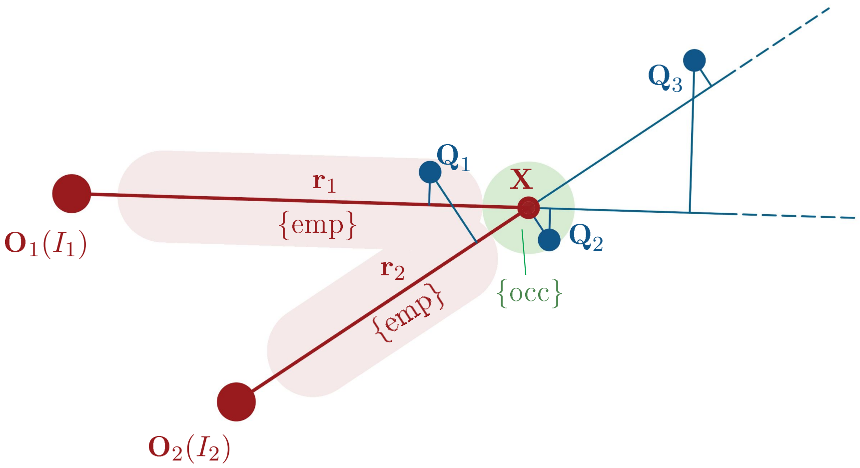

Figure 5.4: Areas of belief from the observation of a 3D point $\mathbf{X}$ by two cameras I_1 and I_2: The red area indicates emptiness along $\mathbf{r}$, whereas the green area depicts occupancy in the vicinity of $\mathbf{X}$. Based on these spatial belief assignments the query location $\mathbf{Q}_1$ is in an empty area (does not exist), $\mathbf{Q}_2$ appears occupied (exists) and $\mathbf{Q}_3$ remains in an unknown state.

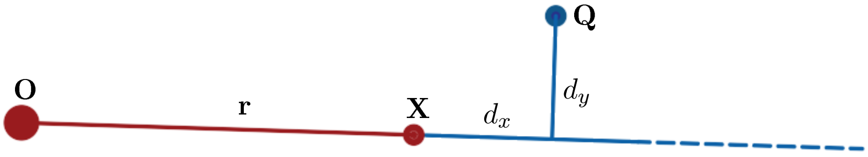

Figure 5.5: Interrelation between a 3D point and a query location: the measures $\mathbf{d}_x$ and $\mathbf{d}_y$ are defined as the longitudinal and transverse distances from point $\mathbf{X}$ to query location $\mathbf{Q}$ along the ray $\mathbf{r}$.

The distance measures d_x and d_y are decisive for supporting or refuting either one of the hypotheses $\{emp\}$ or $\{occ\}$ for each combination of $\mathbf{X}_n$ and $\mathbf{Q}_n$. According to Sec. 5.1.1 d_x is defined as the longitudinal distance from $\mathbf{X}$ to $\mathbf{Q}$ along the viewing ray $\mathbf{r}$, whereas d_y represents the corresponding transverse distance as depicted in Fig. 5.5.

$$\begin{aligned} d_x &= (\mathbf{Q} - \mathbf{X}) \cdot \mathbf{r}_0 \\ d_y &= \|(\mathbf{Q} - \mathbf{X}) \times \mathbf{r}_0\| \quad \text{where} \quad \mathbf{r}_0 = \|(\mathbf{X} - \mathbf{O})\| \end{aligned} \tag{5.7}$$

Following the approach presented by Hebel et al. [2013] and Sec. 5.1.1, the variables d_x and d_y are processed by sigmoid functions (Eq. 5.11) in order to model a gradual transition from one state to another and to achieve a basic probability assignment, which quantifies belief masses according to Eq. 2.23. These functions are controlled by the parameters c (longitudinal extend), λ (gradual transition) and κ (transverse extend). For photogrammetric observations, they should be chosen such that the functions reflect the individual point accuracy and the sampling resolution. Figure 5.6 shows a 3D plot of the mass functions $m\{emp\}$ and $m\{occ\}$ depending on d_x and d_y with the exemplary parameters $c = 5$, $\lambda = 800$ and $\kappa = 15.000$. It depicts the situation of emptiness

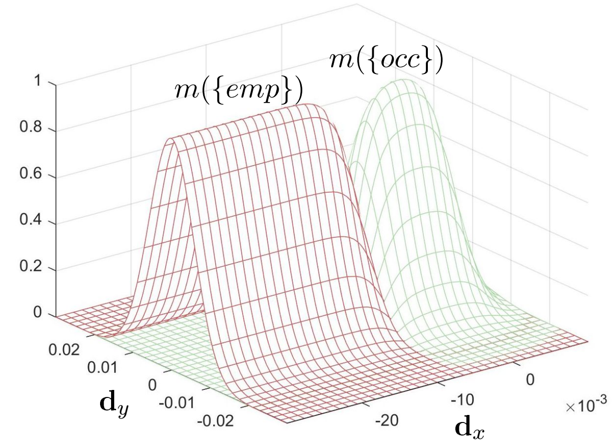

Figure 5.6: 3D plot of mass functions: $m\{emp\}$ (red) and $m\{occ\}$ (green) depending on d_x and d_y [m] with the parameters $c = 5$, $\lambda = 800$ and $\kappa = 15.000$

along the image ray, while the space at the intersection point of two image rays is considered occupied.

$$m_{\mathbf{Q},\mathbf{X}}(0) = \emptyset \tag{5.8}$$

$$m_{\mathbf{Q},\mathbf{X}}(\{occ\}) = \left(1 - \frac{1}{e^{-\lambda\, d_x - c}}\right) \cdot e^{-\kappa\, d_y^2} \tag{5.9}$$

$$m_{\mathbf{Q},\mathbf{X}}(\{emp\}) = \left(\frac{1}{1 + e^{-\lambda\, d_x - c}} - \frac{1}{1 + e^{-\lambda\, d_x + c}}\right) \cdot e^{-\kappa\, d_y^2} \tag{5.10}$$

$$m_{\mathbf{Q},\mathbf{X}}(\Theta) = 1 - m_{\mathbf{Q},\mathbf{X}}(\{emp\}) - m_{\mathbf{Q},\mathbf{X}}(\{occ\}) \tag{5.11}$$

5.1.3 Belief from photogrammetric dense cloud

Due to the complex process of disparity optimization (Sec. 2.2.2), the information about the involved source images from which a 3D point from the image based dense cloud ("dense point" (DP)) was actually generated is usually not accessible. Nor is there an estimated accuracy according to Sec. 2.1.3 per DP available. This results in a necessary change in strategy for evidence based evaluation:

1. The absence of image rays for DPs leads to a lack of information for $m\{emp\}$ and thus to an increase of $m\{U\}$.
2. A lack of accuracy measure leads to a lack of reasonable parameter setting for the mass functions, confidence levels and final belief assignments.

Interior scenes and corresponding building models consist mainly of planar surfaces, and this prior knowledge can be used to derive belief masses in a similar way as suggested by Hebel et al. [2013]. In contrast to the approach of Sec. 5.1.2, the distance measures d_x and d_y are now based on the surface normal $\mathbf{n}_0$ of a query location $\mathbf{Q}$. d_x is the shortest distance from a DP $\mathbf{X}$ to the surface of $\mathbf{Q}$ and d_y is defined as the distance from this perpendicular point to $\mathbf{Q}$ (Fig. 5.7).

$$\begin{aligned} d_x &= (\mathbf{X} - \mathbf{Q}) \cdot \mathbf{n}_0 \\ d_y &= \|(\mathbf{X} - \mathbf{Q}) \times \mathbf{n}_0\| \end{aligned} \tag{5.12}$$

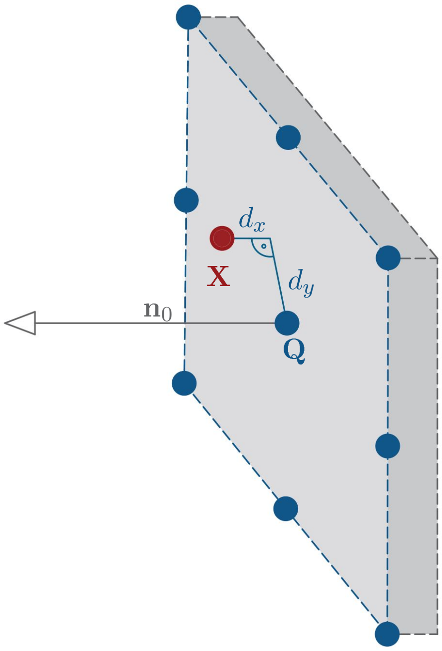

Figure 5.7: Distance measures d_x and d_y between $\mathbf{X}$ and a query location $\mathbf{Q}$ in case $\mathbf{X}$ is a "dense point" considered on a plane with normal direction $\mathbf{n}_0$

The corresponding mass functions simplify to:

$$\begin{aligned} m_{\mathbf{Q},\mathbf{X}}(0) &= \emptyset \\ m_{\mathbf{Q},\mathbf{X}}(\{occ\}) &= \left(1 - \frac{1}{e^{-\lambda\, d_x - c}}\right) \cdot e^{-\kappa\, d_y^2} \\ m_{\mathbf{Q},\mathbf{X}}(\{U\}) &= 1 - m_{\mathbf{Q},\mathbf{X}}(\{occ\}) \end{aligned} \tag{5.13}$$

The variable d_x indicates the deviation of $\mathbf{X}$ from the surface of $\mathbf{Q}$. A large d_x should be punished with low belief in occupancy at $\mathbf{Q}$. A degradation of d_x is achieved by increasing the transverse extend and decreasing the longitudinal extend of occupied space at $\mathbf{X}$ in a way that the function gets a narrow, elliptical shape that expands in the direction of d_y. Figure 5.8 shows an example of the effect of an adjusted parameter setting for DP belief assignment on a planar surface.

5.2 Fusion of multiple evidence

Whenever there is not only one TLS ($\mathbf{P}$) or image based ($\mathbf{X}$) observation but several observations in the neighborhood of $\mathbf{Q}$, it is necessary to calculate their joint belief mass. The fusion of belief according to *Dempster's Rule of Combination* requires a separate treatment of potentially conflicting and non-conflicting evidence.

5.2.1 Combining potentially conflicting evidence

Each individual consideration of a point measure $\mathbf{P}$ or $\mathbf{X}$ and a query location $\mathbf{Q}$ results in a certain amount of belief for $\{occ\}$, $\{emp\}$ and $\{U\}$. However, there is more than only one observation in the immediate vicinity of $\mathbf{Q}$ expected. As the "heart" of DST, Dempster's rule for the combination

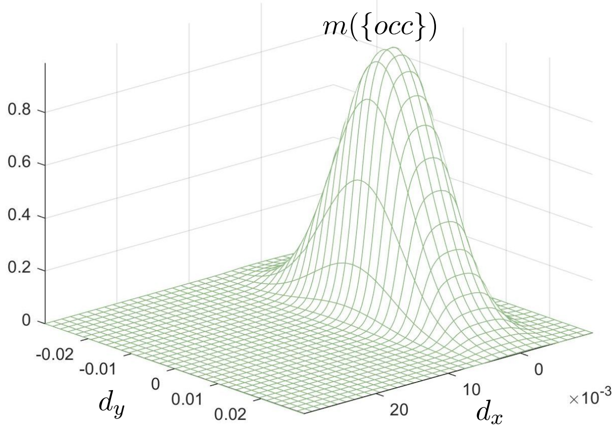

Figure 5.8: 3D plot of the mass function $m\{occ\}$ depending on d_x and d_y for belief assignments on planar surfaces with the adjusted parameters $c = 5$, $\lambda = 1.200$ and $\kappa = 6.000$

Table 5.1: Designations for the application of Dempster's rule of combination (eq. 2.24). For better readability, the following abbreviations are used: $m_1(\{occ\})$ to $m_1(o)$, $m_1(\{emp\})$ to $m_1(e)$, etc.

$m_1(A)$	$m_2(B)$	$m_{1,2}(C)$
$m_1(o)$	$m_2(o)$	$m_{1,2}(o)$
$m_1(e)$	$m_2(e)$	$m_{1,2}(e)$
$m_1(U)$	$m_2(U)$	$m_{1,2}(U)$

of multiple evidence is applied to consider the influence of several belief assignments for a joint interpretation of the observations.

$$m_{1\oplus 2} = m_1 \oplus m_2 \tag{5.14}$$

The physical states $\{occ\}$ and $\{emp\}$ cannot exist simultaneously at one position $\mathbf{Q}$. If one of the hypotheses is true, this means that the other must be excluded. Therefore, the conflict degree k must be considered for belief functions that are defined over sets of hypotheses that contradict each other according to Eq. 2.25.

$$k = m_1(e)\, m_2(o) + m_1(o)\, m_2(e) \tag{5.15}$$

The application of eq. 2.24 on both TLS and photogrammetric observations with assigned mass functions results in the following operations:

$$m_{1,2}(o) = \frac{m_1(o)\, m_2(o) + m_1(o)\, m_2(U) + m_1(U)\, m_2(o)}{1 - (m_1(e)\, m_2(o) + m_1(o)\, m_2(e))} \tag{5.16}$$

$$m_{1,2}(e) = \frac{m_1(e)\, m_2(e) + m_1(e)\, m_2(U) + m_1(U)\, m_2(e)}{1 - (m_1(e)\, m_2(o) + m_1(o)\, m_2(e))} \tag{5.17}$$

$$m_{1,2}(U) = \frac{m_1(U)\, m_2(U)}{1 - (m_1(e)\, m_2(o) + m_1(o)\, m_2(e))} \tag{5.18}$$

Table 5.1 gives an overview for proper use and assignment of designations and abbreviations in the formulas.

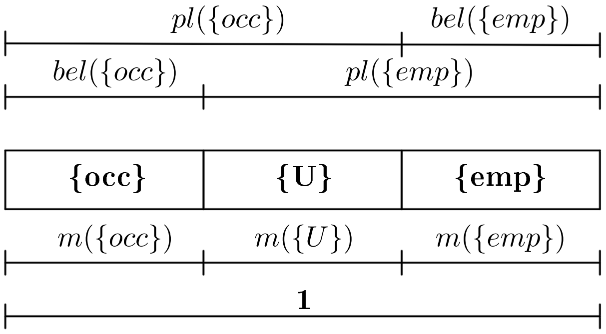

Figure 5.9: Illustration of different belief representations m, bel and pl associated with occ, emp and U.

5.2.2 Combining non-conflicting evidence

The number of image based depth points is usually significantly larger than the number of tie points. It is very likely to find several DP in the neighborhood of $\mathbf{Q}$. Therefore, the application of Dempster's combination rule is even more important here. In contrast to $m\{occ\}$ and $m\{emp\}$, the hypothesis $m\{occ\}$ and $m\{U\}$ do not contradict each other. Therefore, the normalization constant can be omitted for the joint mass calculation, which simplifies to:

$$\begin{aligned} m_{1,2}(o) &= m_1(o)\, m_2(o) + m_1(o)\, m_2(U) + m_1(U)\, m_2(o) \\ m_{1,2}(U) &= m_1(U)\, m_2(U) \end{aligned} \tag{5.19}$$

5.3 Integration of model uncertainty

The representation of real-world conditions in a BIM is inherently uncertain. According to the USIBD, each represented element of a BIM can be assigned to a certain LOA in order to properly reason with its geometric accuracy (Sec. 2.4 and Fig. 2.1). The LOA are defined in terms of standard deviation σ. This information from classical probability theory must now be related to the available evidences about the occupancy of space from the TLS measurements.

In DST the degree of belief for a certain question is obtained from masses which refer to subjective probabilities (Sec. 2.3). A hypothesis can be constituted by subsets. Otherwise, if a hypothesis is consisting of only one element ($A \subseteq \Theta$ with $|A| = 1$) it is called a *singleton*. The belief in a hypothesis $bel(A)$ is constituted by the sum of the masses of all subsets B_i that may exist ($B \subseteq A$):

$$bel(A) = \sum_{B_i \in A} m(B_i) \tag{5.20}$$

It forms a lower bound on the probability of a given hypothesis. The plausibility (pl) expresses how plausible a hypothesis A is, i.e. how much belief mass potentially supports A because there may be only a certain amount of evidence that completely contradicts that hypothesis. Plausiblity is 1 minus the sum of all masses that can be committed to the complement

$$\bar{A} : pl(A) = 1 - bel(\bar{A}) \tag{5.21}$$

$pl()$ can be interpreted as an upper bound for an unknown probability function [Shafer, 1976]. The functions $bel()$ and $pl()$ convey precisely the same information and may be obtained from the other [Reineking, 2014]. Figure 5.9 illustrates the relationship between the different belief representations.

Table 5.2: Probabilities for point cloud-to-BIM verification for different LOA

LOA	2σ [mm]	Φ	$P(A)$
50	1	0.9773	0.9545
40	5	0.6554	0.3108
30	15	0.5517	0.1034
20	50	0.5160	0.0319

Table 5.3: Numerical example for different belief representations for a laser point **P** and a model edge **Q** assigned to LOA 50.

	$m()$		$bel()$		$pl()$	
	p	**q**	**p**	**q**	**p**	**q**
occ	0.20	0.95	0.20	0.95	0.50	0.95
emp	0.50	0.05	0.50	0.05	0.80	0.05
U	0.30	0.00	1.00	0.00	1.00	0.00

A probability function $P(A)$ is a normalized belief function with a focal set composed of singeltons. Such a belief function is called *Bayesian* and satisfies the property of additivity:

$$bel(A \cup B) = bel(A) + bel(B) \tag{5.22}$$

A belief function is called *Bayesian* if it is normalized and all of its focal sets are singletons, i.e. if it is a probability function:

$$P(A) = bel(A) = pl(A) \tag{5.23}$$

The hypothesis $\{occ\}$ and $\{emp\}$ are singeltons because they do not have any subsets. The probability for a BIM element **Q** can be derived from its standard deviation according to its assigned LOA. Assuming normally distributed observations, the standard deviation can be used to define a confidence level. In agreement with the TLS and image measurements, it is assumed that the occupancy of a location is confirmed over 95%, assuming an accuracy of 1 mm. This corresponds to LOA 50 with a confidence of $0.9545 \mathrel{\widehat{=}} 2\sigma = 1\text{mm}$. Starting from the confidence level for LOA 50, the confidences for BIM elements that correspond to other accuracy levels can be derived according to the standard normal distribution. For each multiple of $\sigma = 0.5$ mm the area under the standard curve is determined in order to derive its probability e.g. using a unit table which contains the values (Φ) of the cumulative distribution function of the normal distribution. Table 5.2 shows the resulting probabilities for LOA 50 to LOA 20. The density function from probability theory corresponds to the mass function in evidence theory. Refer to Table 5.3 for a numerical example for different belief representations for an exemplary **P** and a corresponding **Q** of LOA 50.

Also for photogrammetric observations individual accuracy information of tie points (TP) and depth points (DP) with σ_{TP} and σ_{DP} have to be put in a reasonable relation according to the belief masses of the initial BIM representation **Q**. A fusion of belief masses from different confidence levels is achieved by converting the belief assignments according to the cumulative distribution

Table 5.4: Numeric example of the conversion of belief masses from different sources

	$\sigma_{TP} = 2\,\text{mm}$; $bel(o)_{TP} = 0.8500$			$\sigma_{DP} = 2.5\,\text{mm}$; $bel(o)_{DP} = 0.7300$		
LOA	50	40	30	50	40	30
σ_i [mm]	0.5	2.5	15	0.5	2.5	15
Z	0.25	1.25	7.5	0.2	1	6
$\Phi(Z)$	0.40129	0.10565	≈ 1	0.42074	0.15866	≈ 1
$P(o)$	0.19742	0.78870	≈ 1	0.15852	0.68268	≈ 1
$bel(o)_P$	0.1766	0.7057	0.8947	0.1218	0.5246	0.7684

function of the normal distribution. An up- or downgraded belief mass $bel()_{LOA}$ for joint mass calculation results from

$$bel()_{LOA} = \frac{P()\,bel()}{2(\Phi(1) - 0.5)} \qquad (5.24)$$
$$\text{where } P() = 2\sqrt{(\Phi(Z) - 0.5)^2}$$

Table 5.4 gives an numeric example for the conversion of belief assignments from different sources.

5.4 Decision making from combined belief and BIM related uncertainty

As-built building models, also referred to as *digital twins*, are playing a central role in the AEC industry's digital revolution. The creation and maintenance of these 3D models is to already start with the first construction works, so that the construction management can carry out progress control, documentation and as-built analyses with the time of beginning early construction phases. Geodesists are to answer the question of whether or not 3D measurements conducted on site confirm an associated BIM-compliant model for certain tasks. In order to give a qualified assessment on the basis of photogrammetric 3D point clouds and given BIM data, the following three aspects have to be evaluated:

- Accuracy: The significance of detected deviations between measurement and model depends on both, the accuracy of the measurement (Sec. 2.1.3) and the accuracy of the reference geometry, e.g. according to the LOA specification (Sec. 2.4). The maximum belief in the geometrical correctness of a BIM that is obtained from a single $\mathbf{P}-\mathbf{Q}$ or $\mathbf{X}-\mathbf{Q}$ combination is limited by the individual measurement uncertainty in terms of standard deviation σ. In decision making, however, evidence theory and Dempster's Rule of Combination allow for the strengthening of final belief by combining multiple pieces of evidence, in case they do not contradict each other (Fig. 5.10).
- Resolution: BIM objects are represented by continuous surfaces. However, a photogrammetric scene capture comes with a point-wise sampling that largely depends on the camera-object distance and the conditions on site. With prior knowledge of the object and a suitable target resolution, it is justified to assume directly adjacent measurement points to represent a closed surface. A reasonable resolution can be derived from the BIM's associated Level of Detail (LOD), in order to figure out the smallest detail yet to be modeled, captured and verified. The resolution is obtained from the average point-to-point distance of the 3D point

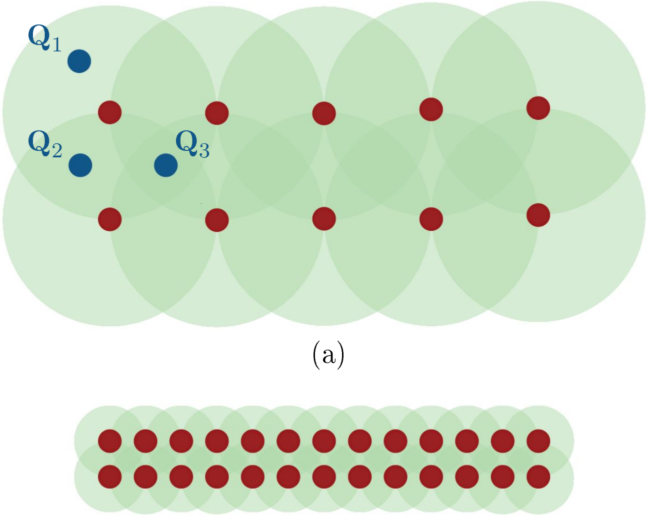

(a)

(b)

Figure 5.10: Different resolution of BIM verification: a) low resolution, i.e. large point-to-point distance, b) high resolution, i.e. small point-to-point distance. The green circles indicate belief around a 3D measurement (red dots) that reinforces in overlapping areas of belief, therefore $bel()_{Q_1} < bel()_{Q_2} < bel()_{Q_3}$.

cloud, e. g. 2 mm. It is the basis for appropriate parameter setting of the belief functions (κ, λ and c) in order to assure their sufficient spatial expression (Fig. 5.10).

- Completeness: Both accuracy and resolution are just as important as the completeness of the object capture is. A critical value for the derived percentage should best be agreed with the aimed resolution and the object's LOD. Indoor sites in particular are commonly challenging environments due to clutter, occlusions, inaccessible areas and a limited range of sensor motion. In order to differ objects that are not observed from those that are actually not there, it is reasonable to structure both the point cloud and the BIM by voxel, e. g. of size 5 x 5 cm, and to perform a visibility analysis according to Chapter 4 in addition to the point-wise evaluation presented in this chapter.

6 Experiments

This chapter presents datasets and experiments that were carried out in order to evaluate the introduced methods of Chapters 3, 4 and 5. All experiments relate to applications for BIM processes, although the first experiment for accuracy investigation on image-to-BIM co-registration is based on synthetic data. The other experiments were conducted at real construction sites with different laser scanners and image sensors and relate to change detection and geometric BIM verification.

6.1 Accuracy investigation on image-to-BIM co-registration

The estimation model presented in Chapter 3 for the optimization of an approximately known camera pose was tested with synthetic data as ground truth for accuracy assessment. The basis is a real test environment. In the following, the reference model, the generation of synthetic data as well as the conducted pose optimizations are presented.

6.1.1 Synthetic images from a virtual camera

A laboratory for measurements with geodetic reference network is used as test environment (Fig. 6.1). It has a local coordinate system whose main axes are aligned with the walls of the building. The network is realized by permanently installed mini prisms and enables the stationing of tacheometers in the lower millimeter range. The laboratory serves as a test environment for validating image measurement techniques and achievable accuracies with respect to the detection of typical objects and component classes inside buildings. To obtain precise geodetic survey data, the laboratory was captured by a 3D laser scanner in a high resolution. The registration of the single scans was done by control points. The global, absolute measurement accuracy in the reference system is 1.5 millimeters and the standard deviation of the relative orientation of the individual scans is in the sub millimeter range when cloud-to-cloud adjustment is performed. The resulting point cloud served as the basis for BIM compliant modeling. The modeling accuracy depends on the respective object class and is based on the recommendations according to the LOA specification. For example, interior doors and windows are assigned to accuracy levels 30 and 40.

A virtual view of the interior model was rendered with 36 mm sensor width, 1600 x 1200 pixels and 30 mm focal length. The projection center is located at position $\tilde{X^0} = [43.907, 28.847, 8.053]^T$ in the reference system and the camera system is rotated by angles $\tilde{\omega} = -67.318°$, $\tilde{\phi} = 1.8°$ and $\tilde{\kappa} = 29.498°$ with respect to the BIM system. The true projection matrix ($\tilde{\mathrm{P}}$) was derived from the parameters of the distortion-free virtual camera according to (2.12).

6.1.2 Parameter estimation from simulated uncertainty

36 model points ($\mathbf{X}_i$) were projected with $\tilde{\mathrm{P}}$ and (2.11) into the synthetic image in order to obtain $\tilde{\mathbf{x}}_i$. For the simulation of inaccuracies in the detection of edges in the image, Gaussian noise of

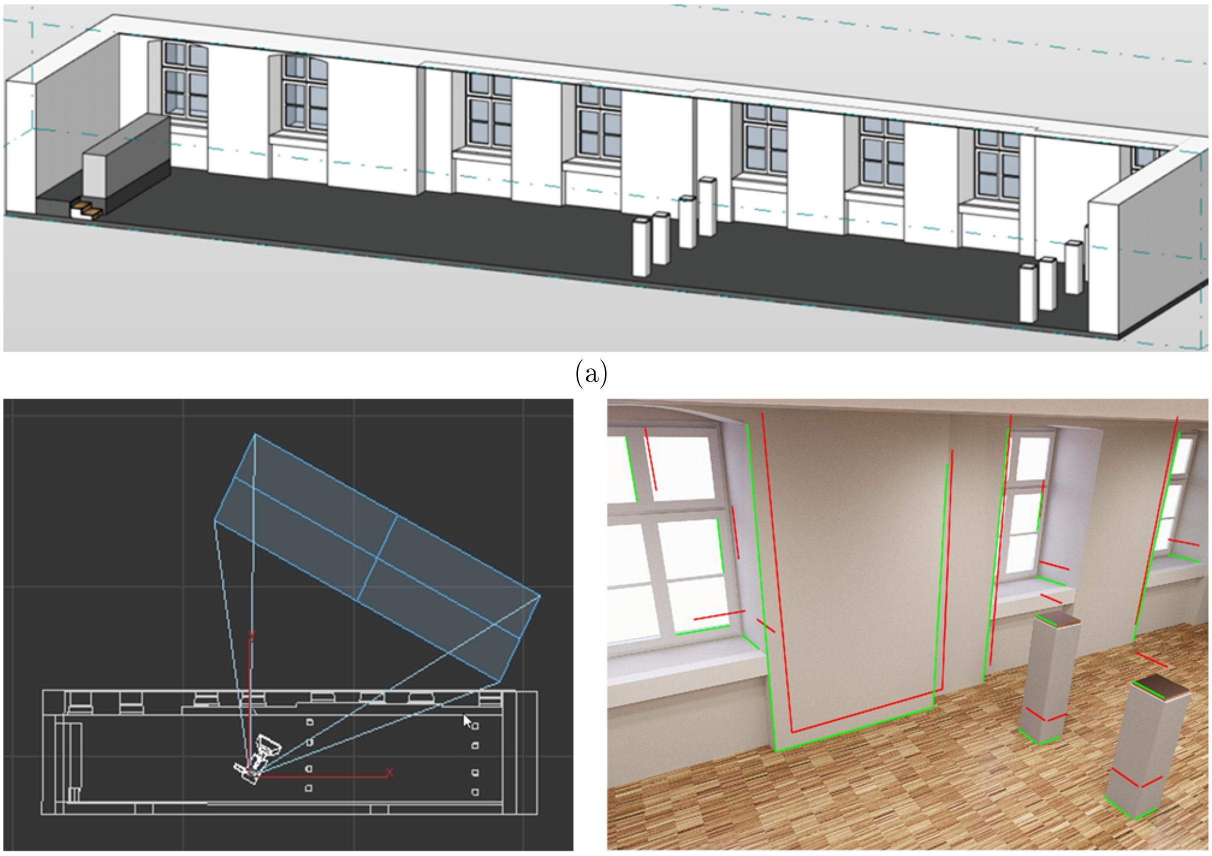

(a)

(b) (c)

Figure 6.1: Generation of synthetic data of a real BIM: a) 3D visualization of the BIM, b) set up of a virtual camera within the BIM for rendering, c) synthetic image with projected 3D edges using $\tilde{\mathrm{P}}$ (green) and P (red)

varying magnitude is added to the Euclidean part of the true pixels ($\tilde{\mathbf{x}}_i$) in the further course. Noisy pixels ($\mathbf{x}_i$) result with the normally distributed random number N:

$$\mathbf{x}_i = \tilde{\mathbf{x}}_i + \sigma_{\mathbf{x}_i} N \tag{6.1}$$

Then, the uncertain image points ($\mathbf{x}_i, \Sigma_{\mathbf{x}_i\mathbf{x}_i}$) were joined to lines by join operation and variance propagation to obtain the uncertain image lines corresponding to the model edges ($\mathbf{l}_i, \Sigma_{\mathbf{l}_i\mathbf{l}_i}$) as observations. A standard deviation in translation of $0.15\,m$ and in rotation of 1° was then set for the external orientation of the camera for artificial degradation (σ_{cam}). This resulted in the initial projection matrix P which is used in the adjustment as approximate initial solution. Figure 6.1 c) shows the synthetic image with the model edges projected into it using $\tilde{\mathrm{P}}$ (green) and P (red).

The estimation of the projection matrix is to be done several times with different imprecise model reference. For this purpose, Gaussian noise is also added to the model points ($\mathbf{X}_i$) in several simulations. The determination of the standard deviation is based on the LOA specification:

$$\mathbf{X}_i = \mathbf{X}_i + \sigma_{\mathbf{X}_i} N \tag{6.2}$$

The LOA are: $2\sigma = 15\,cm$ (LOA 10), $2\sigma = 5\,cm$ (LOA 20), $2\sigma = 15\,mm$ (LOA 30), $2\sigma = 5\,mm$ (LOA 40), $2\sigma = 1\,mm$ (LOA 50) [USIBD, 2019].

P is put in the estimation model as initial value. The actual accuracy of the reference model does not matter here when using synthetic data. For LOA 10 to LOA 50, 100 simulations each

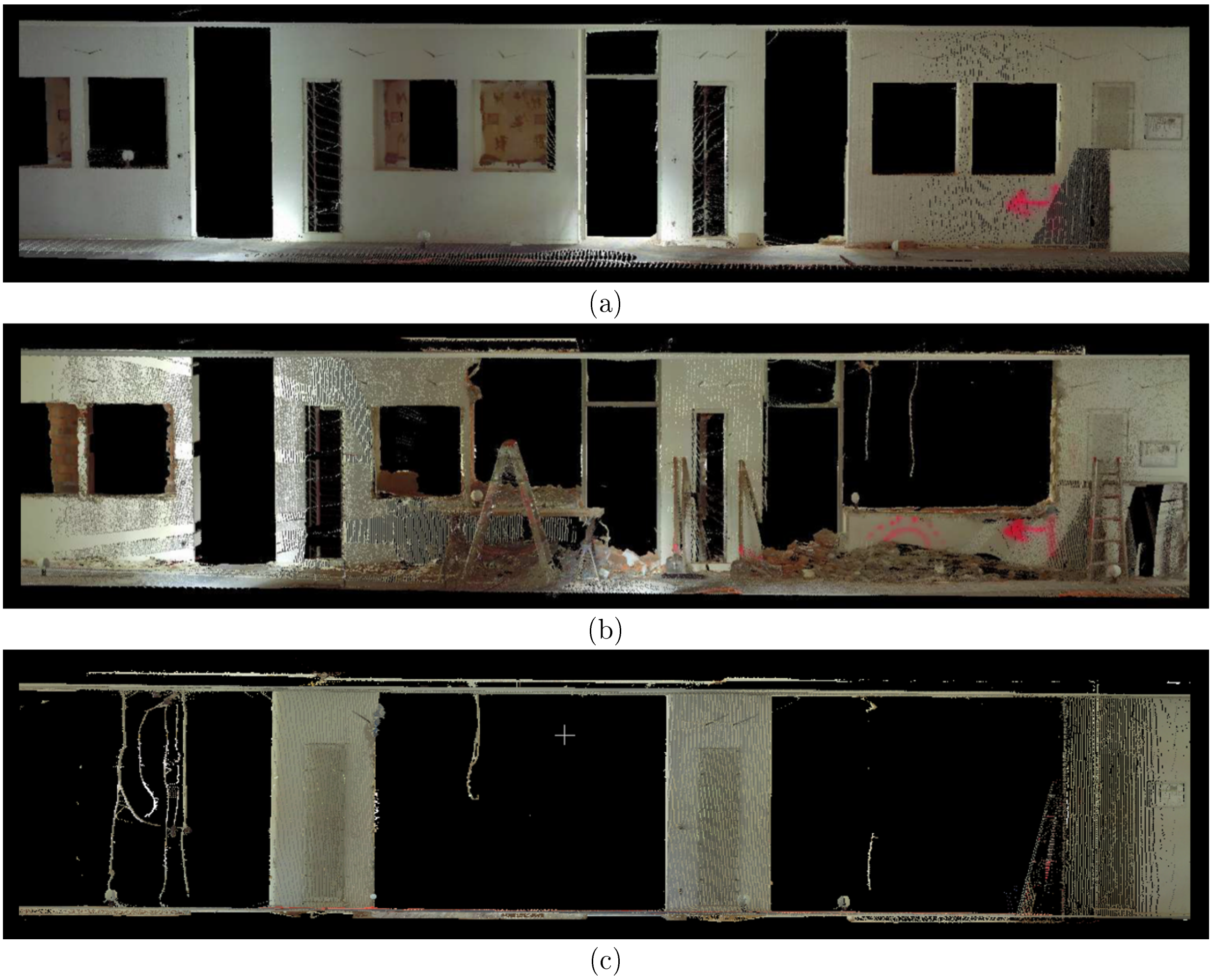

(a)

(b)

(c)

Figure 6.2: Laser scanning data for progress monitoring during demolition work inside of a building: original survey point clouds with RGB color of construction site 1 of a) epoch 1, b) epoch 2, c) epoch 3.

were calculated with image lines of varying degrees of noise $\sigma_1 = 0.0$, $\sigma_1 = 0.5$, $\sigma_1 = 1.0$, $\sigma_1 = 1.5$ and $\sigma_1 = 3.0$ pixel.

6.2 Progress monitoring based on laser scanning point clouds

The following data and experiments refer to progress monitoring based on voxel for two real indoor conversion projects. The first scenario essentially involves the demolition of non-load-bearing wall elements within a long hallway to create more space for an open seminar room in a university building, whereas the second scenario is characterized by partial demolition and simultaneously newly built structural components in the course of converting a former military barrack into rental apartments.

6.2.1 Laser scanning data of construction sites

The demolition work of scenario 1 extended over a period of about 3 weeks within a buildings interior and a FARO® Focus 3D* laser scanner was used to document the project's progress. This

---

*FARO: beam divergence: 0.19 mrad; beam diameter at exit: 2.25 mm

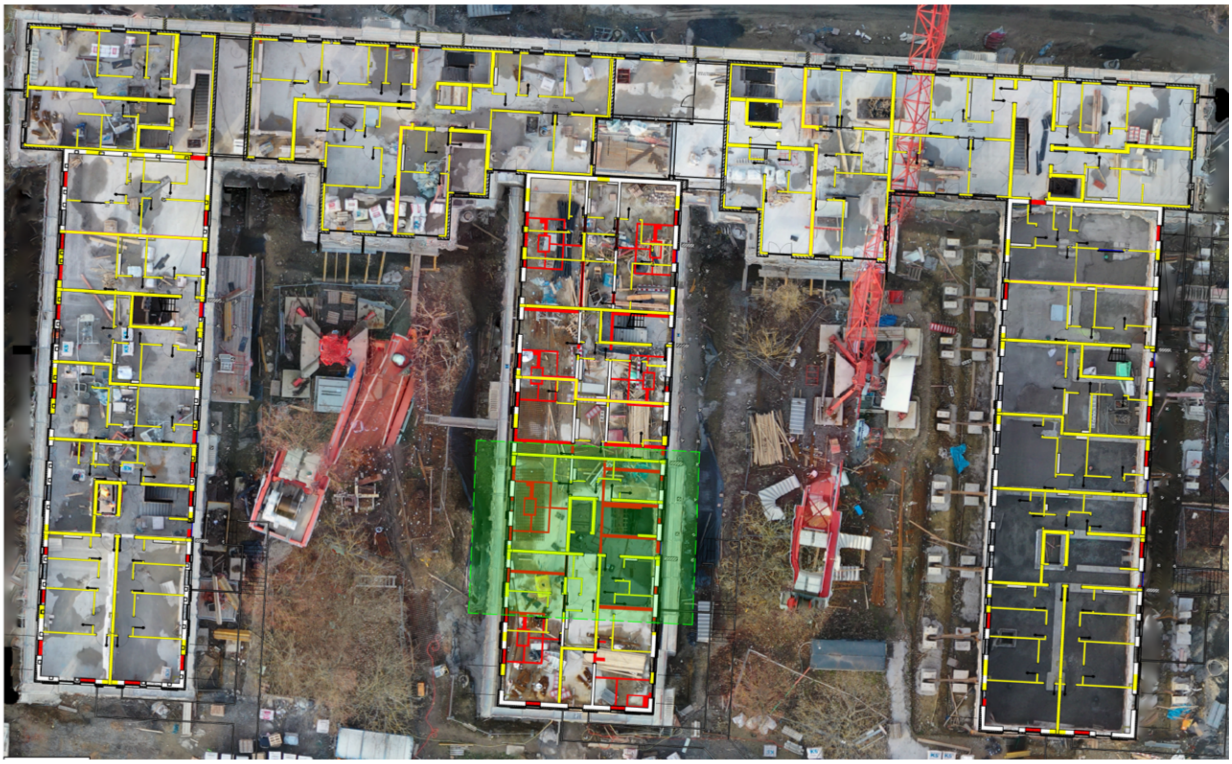

Figure 6.3: Construction site: UAV based orthomosaic (top view) augmented with planning data as overview of the construction site of scenario 2 (indoor conversion). The project mainly involves the demolition of existing walls (red) and the building of new walls (yellow) for new room layouts. The green rectangle indicates the study area for which as-built measurements were conducted.

documentation included three scanning epochs: 1) at project start, i. e. old condition; 2) whilst ongoing demolition work and 3) after completed demolition, i. e. new condition. The three states are depicted in Fig. 6.2. Each survey epoch is composed of three overlapping point clouds. Scenario 2 is part of a major construction site in a city area. A number of old buildings are to be remodeled and expanded in order to provide new living space. The ongoing construction work was captured with a Z+F IMAGER® 5016[†] laser scanner. This project involves two scanning epochs: 1) phase of gutting the interior and 2) construction of new structural elements, e.g. a new ceiling in the area of a former staircase. An aerial orthomosaic of the major construction site, which is subject of scenario 2, is given in Fig. 6.3. For both datasets, the relative orientations of the point clouds within each epoch were realized with a "cloud-to-cloud" approach and consistently good adjustments in the range of sub millimeters where achieved. In order to align the scanning data with the BIM's reference system, tacheometric observed checkerboard targets were used. The absolute orientation of each epoch yielded $\approx 1 - 2.5\,\mathrm{mm}$. The measurements were performed with a Trimble® S6 total station.

6.2.2 High-resolution voxel-based change detection

The available indoor point clouds each include several millions of points and thus reveal very high resolution spatial information about the construction sites. In scenario 1, epoch 1 contains $\approx 33\,$mio. points to process, epoch 2 $\approx 28\,$mio. and epoch 3 $\approx 35\,$mio. Each data set has a quite heterogeneous point-to-point distance due to the highly varying scanner-object distances in the

---

[†] Z+F: beam diameter / divergence: $\approx 3.5\,\mathrm{mm}$ at $1\,\mathrm{m}/\approx 0.3\,\mathrm{mrad}$

constraint indoor environment. However, in the main targeted region the average point-to-point distance is $\approx 2\,\mathrm{mm}$. The overall investigation area of project 1 covers $11.46 \times 15.25 \times 3.38\,\mathrm{m}$. The point clouds describing the as-is state of project 2 cover $19.95 \times 19.95 \times 10.13\,\mathrm{m}$ of the construction site and epoch 1 and 2 each include ≈ 200 mio. 3D points. Both datasets were processed and investigated based on 1 cm voxel size. The voxel space V is defined by the according BIM's reference system, and does not take into account individual point densities or distributions as for example it would be the case for an octree based space partitioning. Therefore, a co-registration of voxel from different epochs is not necessary. To calculate the path of the laser beam $\mathbf{r}_V$ through the voxel space V, a variant of Bresenham's algorithm was used [Bresenham, 1965]. In order to automatically detect changes based on conflicting evidence, every voxel is compared with its corresponding voxel from the other epochs and the BIM itself according to Sec. 4.1.2 and Sec. 4.1.3.

6.3 Experiments on geometric BIM verification

Whenever there is a BIM, either a coarse one from an early planning phase or a more sophisticated one supposed to represent the as-built state, it is usually necessary to verify the given model at project start, e.g. for a conversion project. Although the verification of a BIM is highly important and a recurring demand in engineering practice, yet there are no proven guidelines and approaches established in order to efficiently solve for this task. Therefore, elaborate surveys and remodeling of the entire scene are usually carried out. Since there is a need for practical solutions, this section is focused on the application of the geometric verification approaches proposed in Chapter 5 to either confirm or refute a given BIM and its associated LOA based on 3D point clouds that were generated from both TLS and photogrammetry on real construction sites.

6.3.1 Parameter setting for laser scanning point clouds

The impact of a laser range measurement $\mathbf{P}$ on a query position $\mathbf{Q}$, which represents an arbitrary location in the BIM is determined according to Sec. 5.1.1. The evaluation of the states *occupied*, *empty* and *unknown* are based on the longitudinal and transverse distances d_x and d_y. For the point cloud data presented in Sec. 6.2.1, these parameters were processed in the mass functions 5.3 ideally to find clear confirmation for one of these hypotheses.

The modeled impact of a laser range measurement on the occupancy of space should properly reflect its absolute point positioning accuracy and also the physical characteristics of the laser beam. Considering the typical error sources on TLS measurements (Tab. 2.1) leads to $\sigma_\mathbf{P} = 2.5\,\mathrm{mm}$. The parameters c, λ and κ control the fuzziness and propagation of the modeled laser beams. To find the correct values one should start with the parameter κ. According to Hebel et al. [2013] κ should be chosen such that the full width at half maximum of $e^{-\kappa\, d_y^2}$ amounts twice the average point-to-point distance, which is $\approx$ 2mm for the experiments. The parameters are set to $c = 3$, $\lambda = 600$ and $\kappa = 20000$ (Fig. 6.4). This setting results in a realistic model, provided a sufficient point density which allows for neighboring point *masses* to interfere, i.e. causing an area filling overlap.

6.3.2 Stochastic assessment of BIM related geometry

A BIM corresponds to a central spatial project database. Any structural or semantic changes to the real building should be incorporated into the model. Experts feed in their specialized data, so that all project participants can benefit from it for their concerns. Above all, the geometric model must be accurate and error-free if analysis and subsequent planning is to be based on it. Using the examples of the conversion projects and corresponding BIMs, which include existing and to be demolished elements, a point cloud-to-BIM verification based on evidence theory was performed.

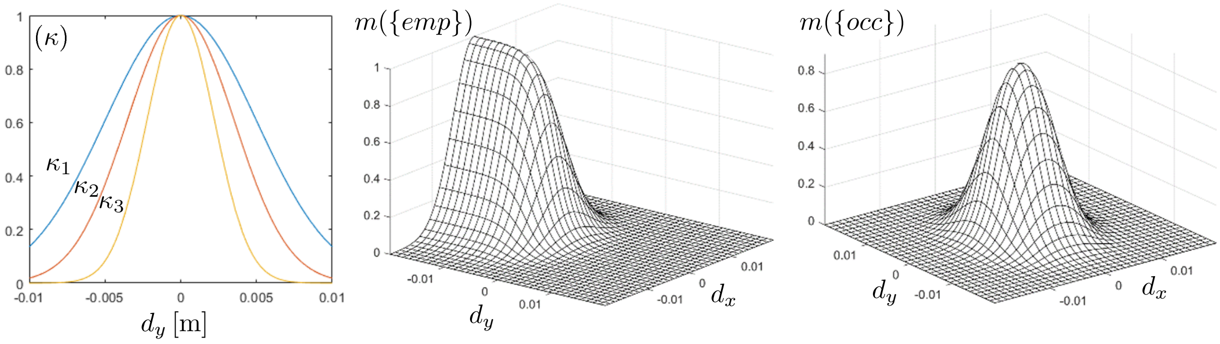

(a) (b) (c)

Figure 6.4: Mass function parameters: a) transverse extend of occupied space based on the parameter $\kappa_1 = 20000$, $\kappa_2 = 40000$ and $\kappa_3 = 100000$, b) mass function $m(\{emp\})$ (empty), c) mass function $m(\{occ\})$ (occupied) assuming $\sigma_\mathbf{p} = 2.5$mm: $\kappa = 20000$, $\lambda = 600$, $c = 3$.

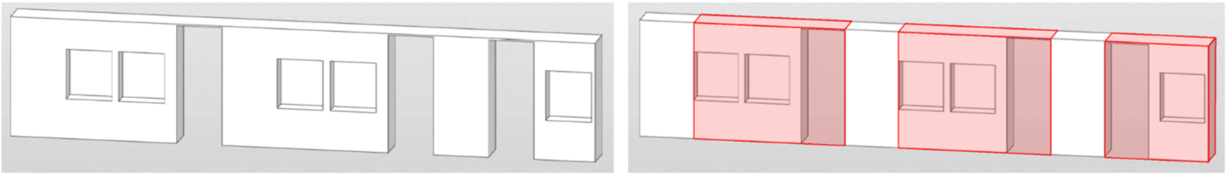

(a) (b)

Figure 6.5: Selected part from the BIM to be verified with belief masses from TLS point clouds: a) BIM version 1 (old state, before demolition), b) BIM version 2 (new state where elements to be demolished are marked red).

The subsequent stochastic assessment relates to the LOA specifications as it is recommended for use in professional practice. The available BIMs, from both project 1 and project 2, refer to previous as-built documentation that was expanded to include new design data for the remodeling projects. The models could be assigned to LOA 30, which means that their structural elements are supposed to be accurate within ± 15 mm at 95 % confidence. According to the USIBD this level of accuracy is the most common one for interior construction and finishes such as floorings and walls. Therefore, LOA 30 also applies for the updated as-built BIMs, which are supposed to represent the new construction state. In addition manufacturing tolerances and related accuracy specifications for as-planned models or objects can be also considered. Depending on the project and customer specific accuracy requirements, it is necessary to decide how densely the given BIM should be sampled for verification. A resolution level of ≈ 2 mm average point-to-point distance was created for the front of a wall surface with openings for doors and display cases (Fig. 6.5) in scenario 1. BIM version 1 denotes the old state, i.e. before demolition and amounts $\approx 400,000$ locations ($\mathbf{Q}_n$) whereas version 2 corresponds to the state after demolition work and involves $\approx 160,000$ points. The laser points of scanning epochs 1-3 were processed with belief functions and the parameters setting described in Sec. 6.3.1.

6.3.3 Photogrammetric data of construction sites

The presented concepts and methodologies of Chapter 5 were used for the evaluation of execution work in three indoor construction projects from photogrammetric as-built data. All three datasets that shall be presented in the following were acquired during as-built and progress documentation surveys that were carried out on real construction sites. The special characteristics of the scenarios as well as the used cameras, geodetic instruments and resulting datasets slightly vary individually:

1. Interior work: Scenario 1 relates to the interior work phase of a new apartment building (Fig. 6.6.a). The construction site was captured with an Apple IPhone's back camera in addition to a terrestrial laser scan performed with a Faro Focus 3D as reference for comparison and evaluation.
2. Indoor conversion: Scenario 2 is part of a major conversion project taking place on former barracks sites that will be converted into rental apartments (Fig. 6.3). New room layouts are implemented structurally, including the bricking of openings and partial demolitions of walls. The scene was captured with the unmanned aerial vehicle (UAV) DJI Inspire 2, equipped with a Zenmuse camera (Fig. 6.6.c and Fig. 6.6.d). Additionally, a reference scan from a Z+F Imager 5016 laser scanner is available.
3. Gutting of a building: In the course of a renovation, scenario 3 takes place within the gutting phase of a building such that only load-bearing structural elements remain. This scenario is characterized by the largest camera-object distance as the ongoing gutting had already created wide empty areas. The scene was captured with a Sony alpha camera (Fig. 6.6.b) and again, a reference point cloud created with a Z+F Imager 5016 laser scanner is additionally available.

Initially, the images of the three test scenarios each were processed with the photogrammetric software Agisoft Metashape Professional. This resulted in internal and external camera parameters, tie point coordinates and dense 3D point clouds. Due to the fact that Metashape does not provide sufficient insight into the performed calculations, the bundle block adjustments were recalculated for each scenario based on the Matlab implementation for bundle adjustment by Börlin & Grussenmeyer [2014] in the Gauss-Markov variant (Sec. 2.1.2). All three camera sensors were each calibrated simultaneously in the course of bundle adjustment. They differ greatly in their quality as can be seen from the tie point accuracies that range from 0.4 to 1.5 pixel. However, these differences are partially compensated by the other project characteristics. For example, the camera quality of scenario 1 is significantly worse than that of scenario 3, but the latter has a much smaller image scale. The properties of the datasets for scenarios 1-3 after final bundle adjustment form the basis for all subsequent processing steps and are summarized in Tab. 6.1.

6.3.4 Empirical dense cloud evaluation

Prior to performing a *Pho-to-BIM* verification based on photogrammetric dense points $\mathbf{X}_n^{DP}$, it is important to determine both, the parameters c, λ and κ for the mass functions that model the extend and spatial expression of belief in occupancy as well as the basic accuracy that is assigned with an according DP. Unlike TPs, DPs do not come with an estimated standard deviation from the bundle adjustment on which to base the parameter setup, and yet, there is no standardized quality measure for DPs either. The photogrammetric software Agisoft Metashape indicates the quality of a DP by the number of contributing combined depth maps, provided as a "confidence" value [Agisoft, 2022]. Although this value indicates somewhat reliability of DPs, it is not assigned a metric accuracy. Another approach is described by James et al. [2017] who ascribe precision values to the DPs based on the precision of their underlying TPs, interpolating uncertainty values into grid cells.

To derive a reasonable spatial belief model for evidence based reasoning from DPs, the metric qualities of dense clouds of scenarios 1-3 were empirically assessed based on corresponding 3D

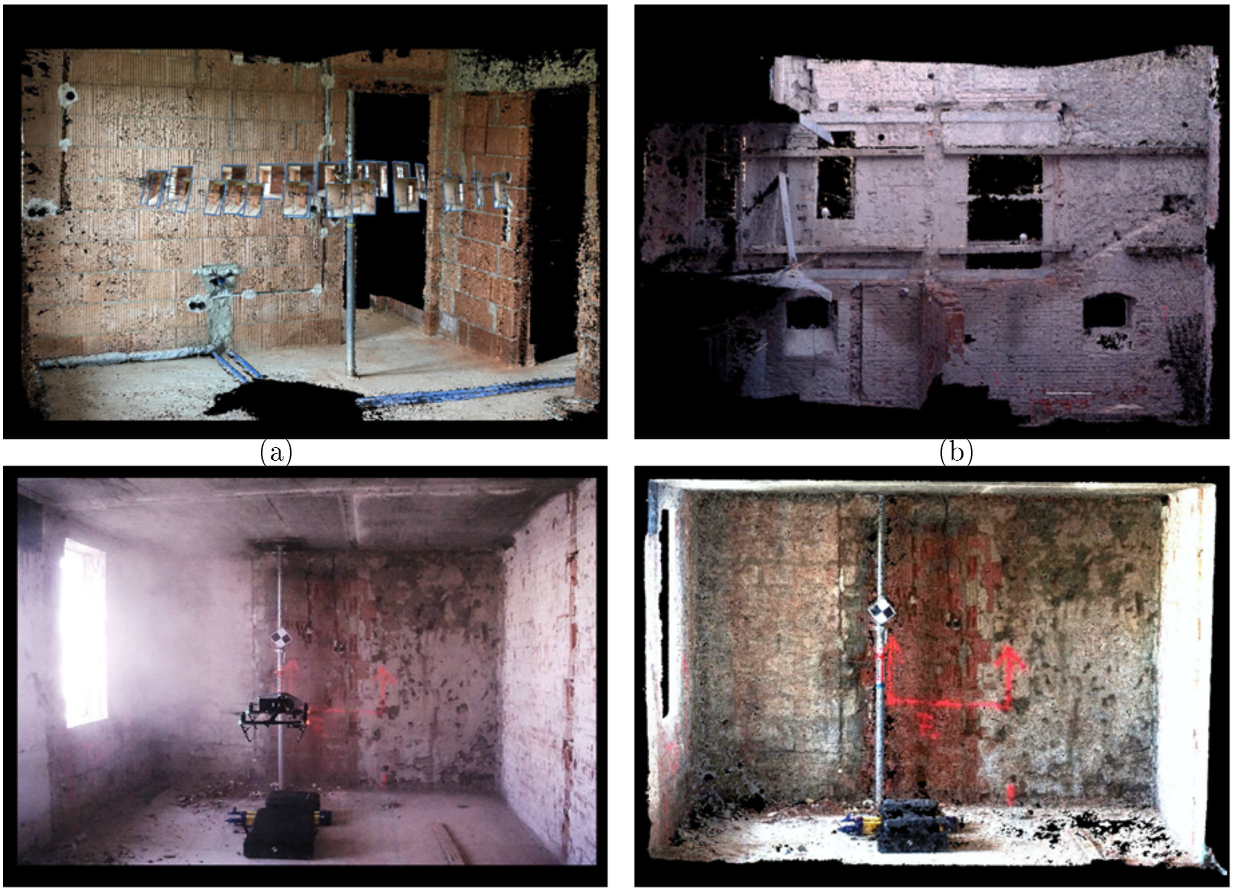
(a) (b) (c) (d)

Figure 6.6: Different scenarios on real construction sites: a) image based point cloud of scenario 1 (interior works), b) image based point cloud of scenario 3 (gutting of a building), c) scene capture with UAV for scenario 2 (indoor conversion), d) image based point cloud of scenario 2

Table 6.1: Characteristics of datasets for scenarios 1-3 after bundle adjustment

Scenario	**1 (interior)**	**2 (conversion)**	**3 (gutting)**
Camera	Apple Iphone 7 back camera	DJI Zenmuse X4S	Sony alpha 5100
Image size [px]	4,032 x 3,024	5,472 x 3,078	4,240 x 2,832
Principal distance [mm]	3.99	8.80	20.00
Number of images	25	57	8
Approx. object distance [m]	2.5	5.0	9.0
Approx. sampling distance [mm]	0.8	1.4	2.5
Number of GCP	5	4	7
GCP accuracy [m], [px]	0.01, 1.0	0.0015, 0.8	0.002, 1.0
Tie point accuracy [px]	1.5	1.0	0.4
Number of estimated TPs	7,371	11,490	9,415
Redundancy R	29,294	72,585	34,834
Estimated variance factor $\hat{\sigma}_0^2$	1.00121	1.17868	0.983674


(a) (b)

Figure 6.7: Exemplary sample of a TLS cloud (a) and a corresponding photogrammetric dense cloud (b) of a brick wall from scenario 2

point clouds from terrestrial laser scanning. The TLS clouds were created at the exact time that the photogrammetric surveys were conducted. Therefore, both types of point clouds show the same scene without any changes, e.g. due to ongoing construction works. The comparison of corresponding point clouds was based on the Multiscale Model to Model Comparison (M3C2) algorithm introduced by Lague et al. [2013]. M3C2 takes into account point cloud registration error, surface roughness and point density. It also offers the possibility of locally estimating a confidence interval for the Level of Detection (LOD) to evaluate the statistical significance of detected local deviations d from one point cloud to another. These properties are advantageous for close range point clouds of indoor constructions with objects of different granularity, e.g. brick walls with deep grooves in comparison to smooth surfaces of concrete elements. The M3C2 distance measure d between two locations from different point clouds is calculated along the surface normal, which is estimated from one (or more) local neighborhood(s) of n points. The spatial variance σ of the neighboring points and the associated point cloud registration error reg is used for the statistical evaluation at a confidence level of 95%.

$$LOD_{95}(d) = \pm 1.96 \left(\sqrt{\frac{\sigma_1(d)^2}{n_1} + \frac{\sigma_2(d)^2}{n_2}} + reg \right) \tag{6.3}$$

[Lague et al., 2013].

The evaluation was carried out on partial sections of the data sets, e.g. on individual wall objects (Fig. 6.7). These sub-areas each represent different conditions, especially in terms of surface roughness, sampling resolution and quality of registration.

6.3.5 Parameter setting for photogrammetric point clouds

The number and spatial distribution of photogrammetric 3D points strongly depends on the survey and object characteristics in terms of image scale, degree of overlap between consecutive images, lighting conditions and object textures on site. Each sub-section of scenarios 1-3 contains several hundreds up to thousands of TPs with estimated σ_x, σ_y and σ_z as a result of image matching

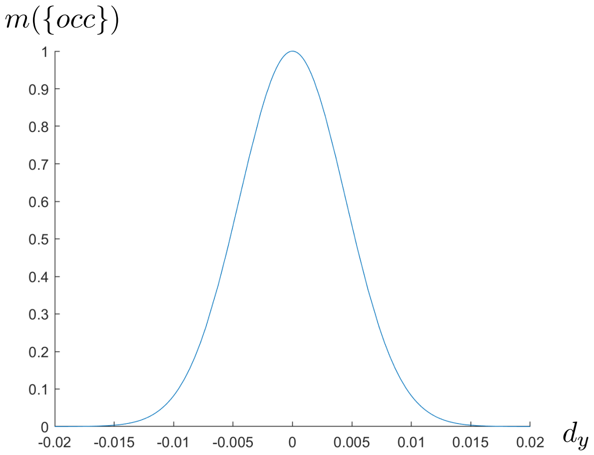

Figure 6.8: Parameter setting for belief functions of photogrammetric point clouds: spatial expression of belief in occupancy along d_y [m] with $\kappa = 25,000$

and bundle adjustment, and millions of DPs from dense matching extended with interpolated and verified accuracies Although the surveys each resulted in a different average point-to-point distance, it is assumed that for each individual scenario neighboring 3D points represent a continuous surface. Belief assignments from neighboring TPs and DPs should on the one hand interfere to derive kind of area filling information, on the other hand they should reflect the inherent fussiness of image based 3D point measurements. The individual uncertainty information is inferred in the phase of combined reasoning in order to balance belief levels by appropriate up- or downgrading and the spatial expression of belief in occupancy is in a first step determined from the average point-to-point distance of the photogrammetric point cloud.

According to the procedure of Sec. 6.3.1, the parameter κ is set such that the distance between points on the curve at which the function $e^{-\kappa\, d_y^2}$ reaches half its maximum value, corresponds to the average point-to-point distance. An exemplary average point-to-point distance of 5 mm leads to $\kappa = 25,000$ to ensure an area filling coverage of $bel > 0.5$ (Fig. 6.8). Whether the setting is then suitable for the specific BIM verification task and its requirements on resolution is not a question of parameter selection. Rather this must be ensured at the project's pre-planning stage in order to chose an appropriate camera and image scale. The parameters λ and c follow κ in a way that $m(\{occ\})$ takes on a smooth, circular shape (Fig. 5.6) for TPs, and a more compressed appearance in the direction of d_x for DPs (Fig. 5.8). A well balanced and appropriate parameter setting will then appear as depicted in Fig. 5.10.

7 Results

The experiments introduced in Chapter 6 relate to different indoor scenarios, construction sites, sensor technologies and methods. The variety of quantitative and qualitative outputs as results of the experiments is subject of this chapter. These involve accuracy investigations on simulated image data for image-to-BIM co-registration, voxel based progress monitoring of construction works of two real conversion projects, and geometric model verification for BIM based on 3D point clouds that were generated from both laser scanning and photogrammetry. The latter comes with the additional results of the empirical image based dense cloud evaluation of Sec. 6.3.4.

7.1 Image-to-BIM co-registration results

An accuracy investigation on image-to-BIM co-registration was conducted on synthetic data of a virtual camera based on the estimation procedure with corresponding line features according to Chapter 3. Simulated statistical uncertainties were used for the experiment of Sec. 6.1. These uncertainties relate to both the geometric reference associated with the BIM, and the quality of straight line detection in the image. After the constraint Gauss-Helmert optimization, the parameters of the exterior camera orientation are only implicitly available in the vector containing the estimated parameters $\hat{\boldsymbol{\beta}}$. The parameter vector $\hat{\boldsymbol{\beta}}$ relates to $\hat{\mathbf{p}}$ - the spherically normalized column vector containing the conditioned elements of $\hat{\mathrm{P}}$. In order to derive the exterior orientation parameters, $\hat{\mathbf{p}}$ is reshaped to the homogeneous 3 x 4 matrix $\hat{\mathrm{P}}$ and re-conditioned with Eq. 3.29. Matrix decomposition results in the coordinates of the projection center and the rotation matrix R with the rotation angles α, β and γ.

Figure 7.1 depicts the projection outcome of statistically uncertain model edges into the synthetic image based on the adjusted projection matrix $\hat{\mathrm{P}}$. The quality of projection and thus image-to-BIM co-registration increases with the assigned LOA of the BIM related reference edges. A high LOA, e. g. LOA 40, results in projected model edges and image lines that coincide well in the synthetic image. The visual effects of a low quality edge projection are clearly recognizable in the pictures of Fig. 7.1. The detailed numerical results of different LOA and simulated accuracies of straight line detection are listed in Table 7.1 and 7.2. They were calculated from 100 simulation runs each. The results show that the exterior orientation of the camera is optimized, provided the reference model has sufficient geometric quality. In the presented example using synthetic data, the camera pose is improved as long as the reference model can be assigned to at least LOA 30 ($\sigma < 7.5\,mm$) and the standard deviation of the image points (for image line construction) for this camera is less than 3 pixels. While very good solutions are achieved with LOA 50 model accuracy, practically this demanding level of accuracy is very rarely achieved in real projects. In practical applications, however, it can be assumed that essential interior elements such as doors, windows and walls are modeled at least LOA 30 compliant and are thus generally suitable as geometric references.

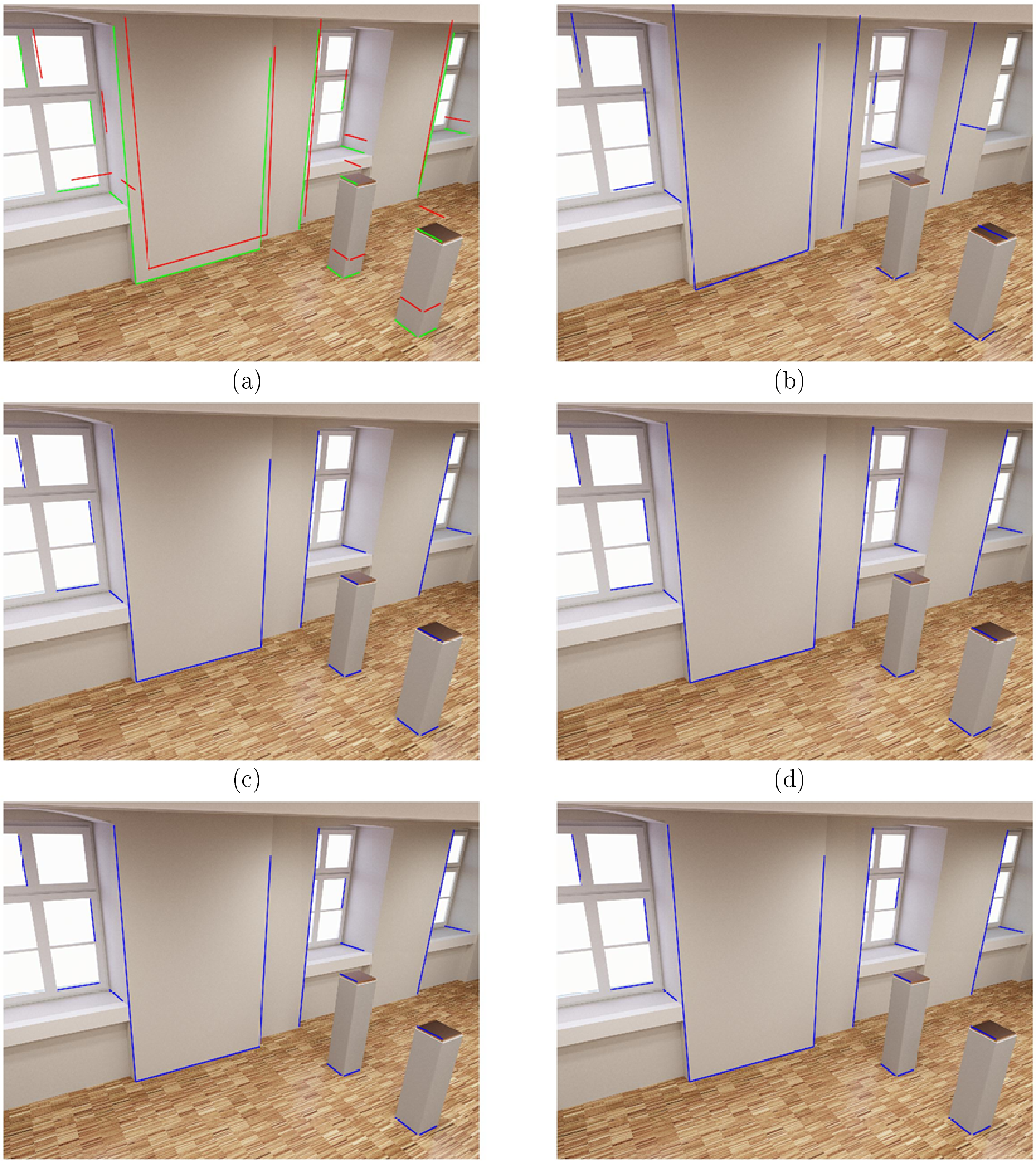
(a) (b) (c) (d) (e) (f)

Figure 7.1: Synthetic image with projected 3D model edges: a) projection with true projection matrix $\tilde{\mathrm{P}}$ (green) and artificially degraded projection matrix P (red); b) adjusted projection matrix $\hat{\mathrm{P}}$ with $\sigma_{\mathbf{l}} = 1.0$ and LOA 10 model; c) adjusted projection matrix $\hat{\mathrm{P}}$ with $\sigma_{\mathbf{l}} = 1.0$ and LOA 20 model; d) adjusted projection matrix $\hat{\mathrm{P}}$ with $\sigma_{\mathbf{l}} = 1.0$ and LOA 30 model; e) adjusted projection matrix $\hat{\mathrm{P}}$ with $\sigma_{\mathbf{l}} = 1.0$ and LOA 40 model; f) adjusted projection matrix $\hat{\mathrm{P}}$ with $\sigma_{\mathbf{l}} = 1.0$ and LOA 50 model

Table 7.1: Results of image-to-BIM co-registration for LOA 50, 20 and 30 with different image line quality and different LOA from 100 simulations each.

LOA 50 ($\sigma = 0.5\,mm$)						
Orientation-parameter	σ_{cam}	Empirical standard deviation (s) from n=100 simulations				
		σ_l=0.0 [px]	σ_l=0.5 [px]	σ_l=1.0 [px]	σ_l=1.5 [px]	σ_l=3.0 [px]
$X0$ [m]	0.15	0.003	0.015	0.026	0.045	0.086
$Y0$ [m]	0.15	0.002	0.010	0.020	0.030	0.072
$Z0$ [m]	0.15	0.002	0.007	0.014	0.023	0.045
α [°]	1	0.031	0.137	0.251	0.464	0.901
β [°]	1	0.015	0.060	0.123	0.183	0.366
γ [°]	1	0.026	0.105	0.222	0.319	0.667
LOA 40 ($\sigma = 2.5\,mm$)						
Orientation-parameter	σ_{cam}	Empirical standard deviation (s) from n=100 simulations				
		σ_l=0.0 [px]	σ_l=0.5 [px]	σ_l=1.0 [px]	σ_l=1.5 [px]	σ_l=3.0 [px]
$X0$[m]	0.15	0.017	0.028	0.035	0.051	0.084
$Y0$ [m]	0.15	0.012	0.017	0.025	0.038	0.063
$Z0$ [m]	0.15	0.009	0.014	0.018	0.025	0.047
α [°]	1	0.160	0.223	0.297	0.461	0.813
β [°]	1	0.072	0.093	0.126	0.199	0.394
γ [°]	1	0.124	0.148	0.216	0.385	0.706
LOA 30 ($\sigma = 7.5\,mm$)						
Orientation-parameter	σ_{cam}	Empirical standard deviation (s) from n=100 simulations				
		σ_l=0.0 [px]	σ_l=0.5 [px]	σ_l=1.0 [px]	σ_l=1.5 [px]	σ_l=3.0 [px]
$X0$ [m]	0.15	0.052	0.054	0.058	0.070	0.113
$Y0$ [m]	0.15	0.041	0.040	0.048	0.053	0.066
$Z0$ [m]	0.15	0.026	0.030	0.033	0.041	0.060
α [°]	1	0.398	0.473	0.571	0.588	0.980
β [°]	1	0.203	0.241	0.284	0.310	0.452
γ [°]	1	0.372	0.442	0.506	0.487	0.767

7.2 Construction progress monitoring results

The progress of indoor construction work of two projects was documented with TLS point clouds as described in Sec. 6.2. The change detection results refer to a voxel size of 1 cm. Essential structural changes in the indoor environment that occurred during conversion project 1 could be clearly detected. Through visual interpretation and inspection, it was determined that demolished wall elements were correctly marked as *disappeared*. The evaluation was performed in the same way for voxel classes *new* and *confirmed*. The architectural structural condition indoors follows a constraint sensor motion and this in turn results in weak overlap of neighboring point clouds. Therefore, in the long, narrow hallway of scenario 1, a relatively large number of voxel were labeled *unknown* as a result of lack of observation mostly due to occlusions. The visual results are depicted in Figure 7.2.

Scenario 2 is characterized by a more open interior, compared to the confined conditions of scenario 1. Nevertheless, optimal scanning geometries could not always be realized in this project

Table 7.2: Results of image-to-BIM co-registration for LOA 20 and 10 with different image line quality and different LOA from 100 simulations each

LOA 20 ($\sigma = 2.5\,cm$)						
Orientation-parameter	σ_{cam}	Empirical standard deviation (s) from n=100 simulations				
		σ_l=0.0 [px]	σ_l=0.5 [px]	σ_l=1.0 [px]	σ_l=1.5 [px]	σ_l=3.0 [px]
$X0$ [m]	0.15	0.213	0.222	0.209	0.230	0.238
$Y0$ [m]	0.15	0.138	0.156	0.128	0.145	0.136
$Z0$ [m]	0.15	0.117	0.152	0.150	0.152	0.144
α [°]	1	1.690	1.530	1.577	1.901	1.733
β [°]	1	0.807	1.103	1.057	1.023	1.012
γ [°]	1	1.336	1.691	1.576	1.633	1.554
LOA 10 ($\sigma = 7.5\,cm$)						
Orientation-parameter	σ_{cam}	Empirical standard deviation (s) from n=100 simulations				
		σ_l=0.0 [px]	σ_l=0.5 [px]	σ_l=1.0 [px]	σ_l=1.5 [px]	σ_l=3.0 [px]
$X0$ [m]	0.15	0.607	0.970	0.959	0.820	0.653
$Y0$ [m]	0.15	0.441	1.048	0.591	0.530	0.516
$Z0$ [m]	0.15	0.489	0.604	0.716	0.747	0.434
α [°]	1	5.353	6.636	4.863	5.087	5.138
β [°]	1	3.201	3.778	4.986	4.691	3.346
γ [°]	1	4.718	5.551	6.650	4.940	4.778

either. Due to the lack of a ceiling in survey epoch 1, the choice of an optimal scanning view point was limited. Additionally, the scenes of construction site 2 were characterized by a lot of clutter such as tools, machinery and building materials. Still, the change detection succeeded well and resulted in a very detailed voxel-cloud. Although discretization by voxel usually results in a significant loss of geometric information, the high-resolution voxelization with only 1 cm voxel size has left visible structures of the walls, demolition edges, formwork supports, safety fences, and even thin reinforcing steel (Fig. 7.4). In total 13,243,632 voxel where classified as either confirmed (65,2 %), new (8.7 %), disappeared (5,0 %) or unknown (21.1 %).

7.2.1 Threshold variation during voxel generation

Scenario 1 was processed in several runs, each with different thresholds $\mathbf{t}$ to experience the effects of voxel size and the heterogeneous point density within the scans, i.e. voxel with different numbers of associated points. The lower $\mathbf{t}$ the more voxel are considered to be relevant, thus the more information comes from the output. The higher $\mathbf{t}$, the higher the quality requirements on the voxel, and the number of voxel that do not meet these requirements anymore. Therefore, a high threshold goes hand in hand with a reduced amount of spatial voxel information as depicted in Fig. 7.5. Nevertheless, the effects of noise and outlier points increase with decreasing $\mathbf{t}$, and a high threshold practically functions as a noise filter. This effect is depicted in Fig. 7.6 where mixed pixel that occurred during indoor scanning, e.g. at the handle of a broom, vanish with increasing $\mathbf{t}$. The threshold has a particularly strong effect on the areas that are far away from the scanner viewpoints and therefore have only a low point density but at the same time a lot of noise. A good compromise and satisfying results were achieved with $\mathbf{t} = 3$. The detailed numerical results of construction site 1 can be found in Table 7.3.

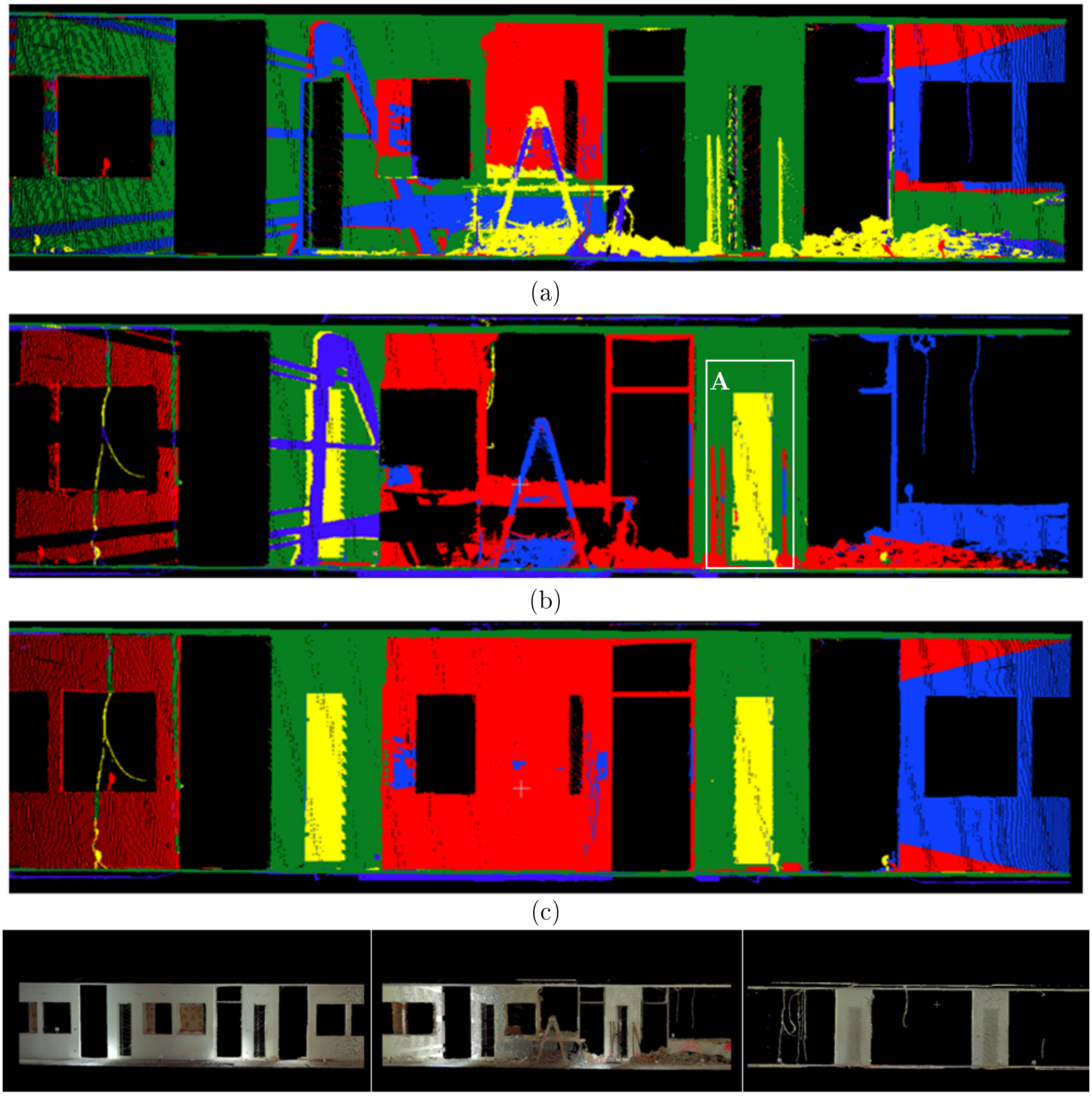

Figure 7.2: Resulting voxel clouds from change detection of project 1: a) epoch 2 vs. epoch 1, b) epoch 3 vs. epoch 2, c) epoch 3 vs. epoch 1 (green = confirmed, yellow = new, red = dissappeared, blue = unknown); Detail A: the yellow voxel indicate a cable duct that had just been closed again; Buttom line: original TLS point clouds from epoch 1, 2 and 3, originally depicted in Fig. 6.2.

Table 7.3: Adjusting the relevance of single measurements from voxel threshold: Results of voxel-based change detection with 1 cm voxel size and different thresholds $t = 3$ and $t = 10$.

epoch	**confirmed** [%]		**new** [%]		**disapp.** [%]		**unknown** [%]		total [$\#points$]	
	$t = 3$	$th = 10$	$t = 3$	$t = 10$	$t = 3$	$t = 10$	$t = 3$	$t = 10$	$t = 3$	$t = 10$
2/1	53.2	52.2	7.9	12.6	4.3	7.8	34.7	27.3	1712632	706100
3/2	49.7	42.9	1.5	2.3	8.4	15.6	40.4	39.2	2327731	809194
3/1	43.6	45.1	1.12	2.3	7.9	16.7	47.4	35.9	2266865	803064

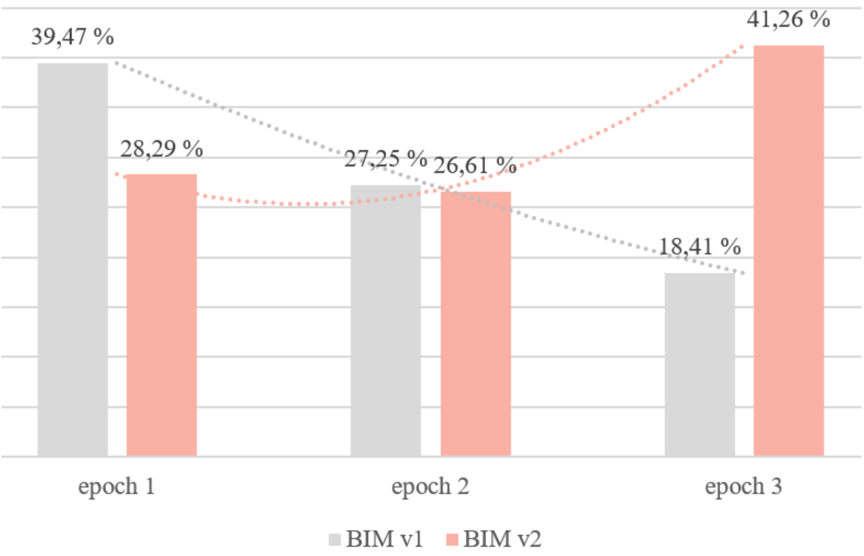

Figure 7.3: Proportion of belief mass > 0.95 from laser range measurements of epoch 1, 2 and 3 confirming each BIM version 1 and BIM version 2.

7.2.2 Change detection point cloud vs. BIM

Change detection in terms of voxel based progress monitoring can also be performed directly using a 3D point cloud and a BIM that is given in the IFC format, instead of exclusively using point clouds from different epochs (Sec. 4.1.3). A point cloud vs. BIM comparison was conducted for construction site 1 and according BIM version 1 (old state before conversion Fig. 6.5), where both the BIM and three measurement epochs were transferred into voxel space using 1 cm voxel size. The advantage of this approach is that, due to the complete knowledge of the target occupancy of space from the model, significantly more spatial change statements can be made. When comparing two point clouds, on the other hand, only two incomplete spatial occupancy models are available, the quality of which strongly depends on the on-site acquisition geometry. The voxel clouds classified into *demolished* and *confirmed* as a result of change detection point cloud vs. BIM for construction site 1 are depicted in Fig. 7.7. The distribution of voxel classes across the measurement epochs clearly reflects the progress of demolition work on site.

7.3 Geometric BIM verification results

A method for the geometric verification of a given BIM was proposed in Chapter 5. In order to assess the presented theories, several experiments on real construction sites were conducted as described in Sec 6.3. The obtained results for TLS based and image based geometry verification are presented in the following. For the latter, a distinction is made between the photogrammetric sparse cloud given unique viewpoint information in terms of coordinates of the projection center, and the photogrammetric dense cloud, which lacks this information for occupancy modeling.

7.3.1 BIM verification using laser scanning point clouds

The point-wise evaluation for scanning epoch 1 with BIM version 1 yielded an almost complete confirmation of the investigated model area of construction site 1 (see Fig 6.2 for original TLS data). Except for two cable ducts (Fig. 7.2.b detail A) that were already open during the scanning survey due to the starting conversion, but not included in the BIM (Fig. 6.5), the modeled and

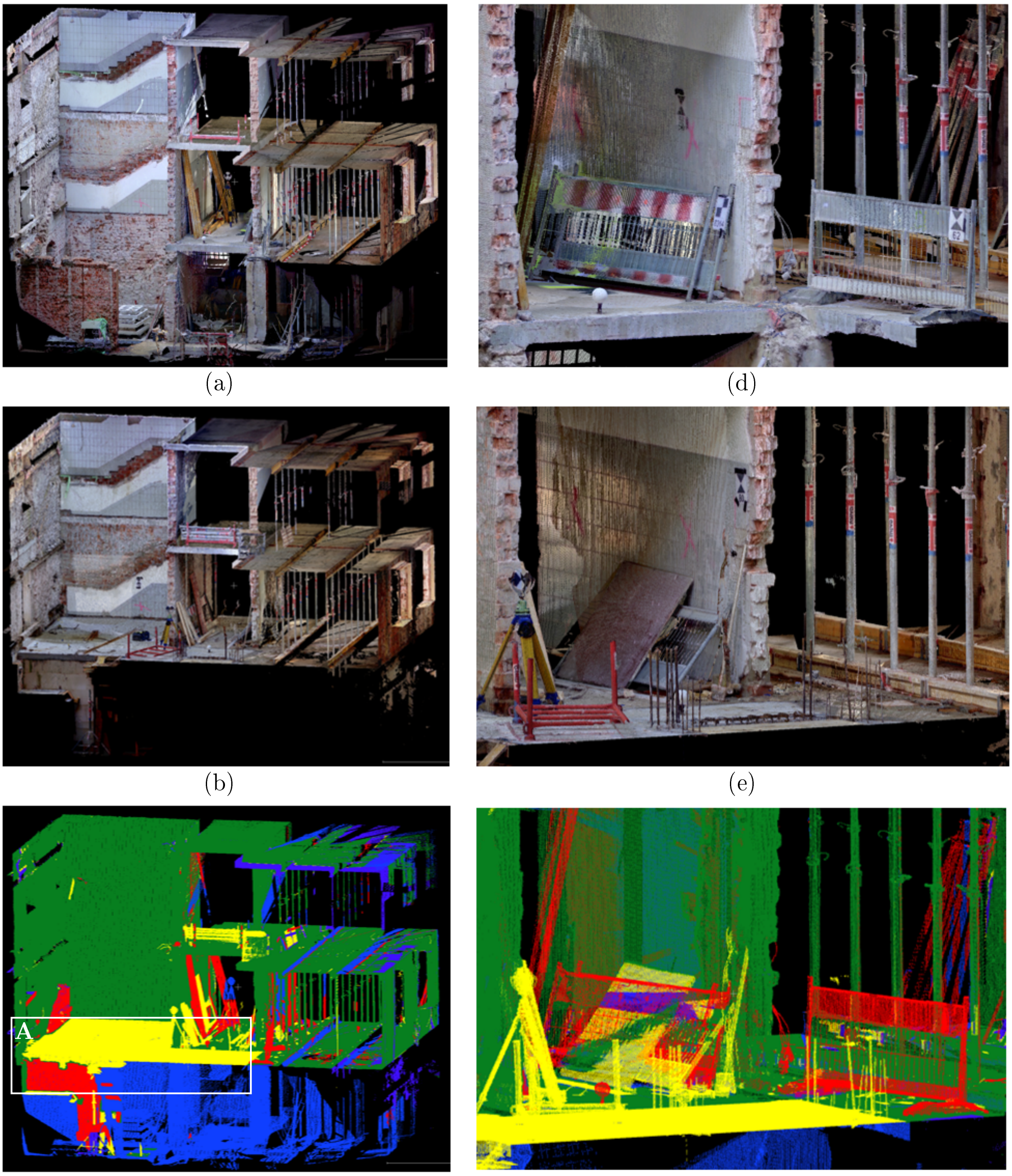

(a) (d)

(b) (e)

(c) (f)

Figure 7.4: Change detection results of construction site 2: a) TLS point cloud with RGB colors from epoch 1, b) TLS point cloud with RGB colors from epoch 2, c) color coded voxel cloud form change detection epoch 2 (new) vs. epoch 1 (old), d) detail TLS point cloud from epoch 1, e) detail TLS point cloud from epoch 2, f) detail voxel cloud (green = *confirmed*, yellow = *new*, red = *dissappeared*, blue = *unknown*), Detail A: newly installed ceiling in the area of a former staircase.

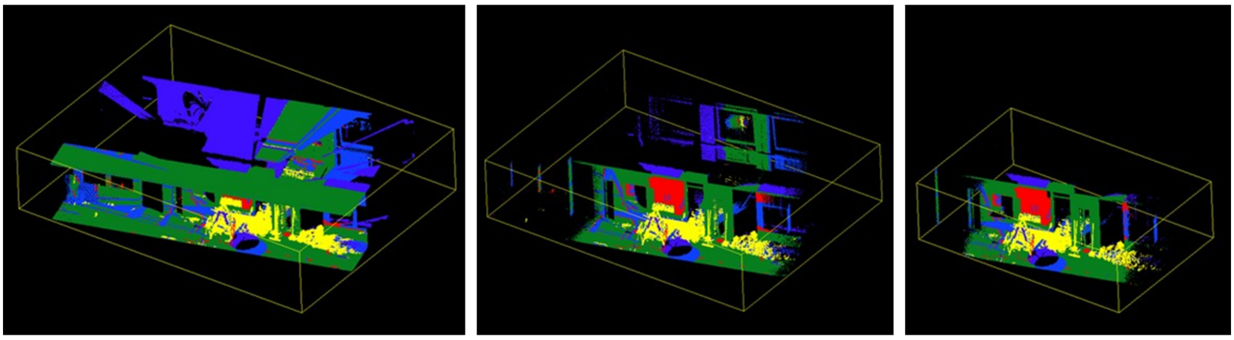
(a) (b) (c)

Figure 7.5: Effect of the magnitude of voxel threshold on the amount of spatial information: an increase of **t** goes hand in hand with a reduced amount of spatial voxel information in the investigated area of the construction site: a) **t** = 3, spatial extend = 11 x 15 x 3 m, No. classified voxel = 1.7 M; b) **t** = 10, spatial extend = 10 x 13 x 3 m, No. classified voxel = 0.7 M; c) **t** = 20, spatial extend = 7 x 10 x 3 m, No. classified voxel = 0.5 M

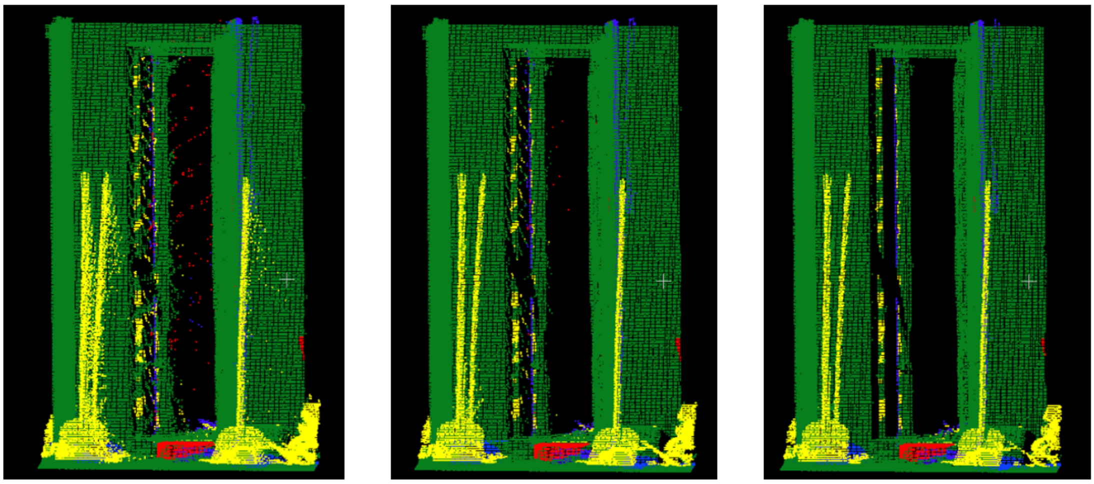
(a) (b) (c)

Figure 7.6: Effect of the magnitude of voxel threshold **t** on noise: an increase of **t** goes hand in hand with a reduction of noise and mixed pixel in the point cloud: a) **t** = 3, b) **t** = 10, c) **t** = 20

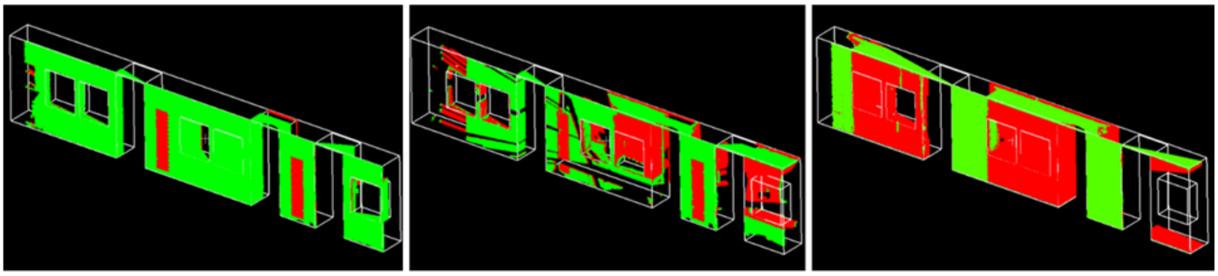
(a) (b) (c)

Figure 7.7: Voxel based change detection in the version TLS point cloud vs. BIM: a) epoch 1 vs. BIM version 1, b) epoch 2 vs. BIM version 1, epoch 3 vs. BIM version 1 (green = confirmed, red = disappeared/ demolished).

Table 7.4: Results of point-to-BIM verification for scenario 1: BIM version 1 and 2 and point clouds of epochs 1, 2 and 3 ($\sigma = 2.5\,\text{mm}$).

epoch	No. points	**BIM version 1**				**BIM version 2**			
		m(o) >0.68		m(o) >0.95		m(o) >0.68		m(o) >0.95	
1	32,689,442	299,158	73.1%	161,460	39.5%	83,894	50.3%	47,198	28.3%
2	27,653,150	188,347	46.0%	111,492	27.3%	78,051	46.8%	44,396	26.6%
3	34,626,046	138,415	33.8%	75,320	18.4%	123,604	74.1%	68,840	41.3%

Table 7.5: Results of point-to-BIM verification for scenario 2: BIM of section 1 and 2, each carried out with point clouds of epochs 1 and 2 ($\sigma = 2.5\,\text{mm}$).

epoch	**section 1**			**section 2**		
	No. points	m(o) >0.68	m(o) >0.95	No. points	m(o) >0.68	m(o) >0.95
1	213,246	14.9 %	0.0 %	457,741	18.1 %	9.5 %
2	1,305,770	42.5 %	4.4 %	5,197,094	57.8 %	35.3 %

real wall surface coincide. The belief functions were initiated based on the parameter setting documented in Sec. 6.3.1. The resulting belief masses are in the range $[0, 1]$ and hence allow for more sophisticated analyses. Figure 7.8 depicts the queried locations $\mathbf{Q}_n$ color coded from red: $m(o) = 0.5$ to green: $m(o) = 1$. It can be seen that the correspondence of BIM and point cloud sightly decreases in the front right area. Since point clouds from epochs 2 and 3 give almost the same result, it can be assumed that the BIM does not fully correspond to the actual as-built condition at this area. Nevertheless, this proportion of weak correspondence is relatively small, as can be seen from the overall distribution of all masses (histograms in Fig. 7.8). Furthermore, by looking at the different survey epochs, one can see how the model and the actual conditions diverge more and more as the construction work progresses. As expected, the results are inversely proportional when using BIM version 2 (Fig. 7.3). Detailed results can be seen in Table 7.4 and Figure 7.8.

Construction site 2 represents a major remodeling project, which includes a large-scale gutting of the entire building (Fig. 6.3). Construction works within the documented survey area include the demolition of walls, removal of wall plaster, construction of new walls, and a new ceiling in the area of a former stairwell (Fig. 7.4.c detail A). The applied point cloud-to-BIM verification reveals areas, which actually match the planning state according to the BIM and areas with a discrepancy between as-is and as-planned. Such deviations either result from construction work that has not yet been carried out, from execution errors or from an incorrect geometry of the reference model despite from its assigned LOA. Figure 7.9 shows the point cloud-to-BIM verification for two certain sections of construction site 2. The walls are very uneven and rough due to the demolition work. In some cases, there are also old tiles on the walls, which cause a deviation in geometry and shape. These circumstances are clearly visible in the evidence based analysis of the model with the TLS measurements. It is also clear to see how a new ceiling was installed between epoch 1 and 2, and how the surface of this structural element is slightly uneven. Detailed results on the achieved confidences can be found in Table 7.5.

7.3.2 Effects of scanning geometry

Terrestrial laser scanning in a building's interior is often challenging due its geometrically constraint conditions. Especially in long corridors, it is often not possible to maintain a sufficient

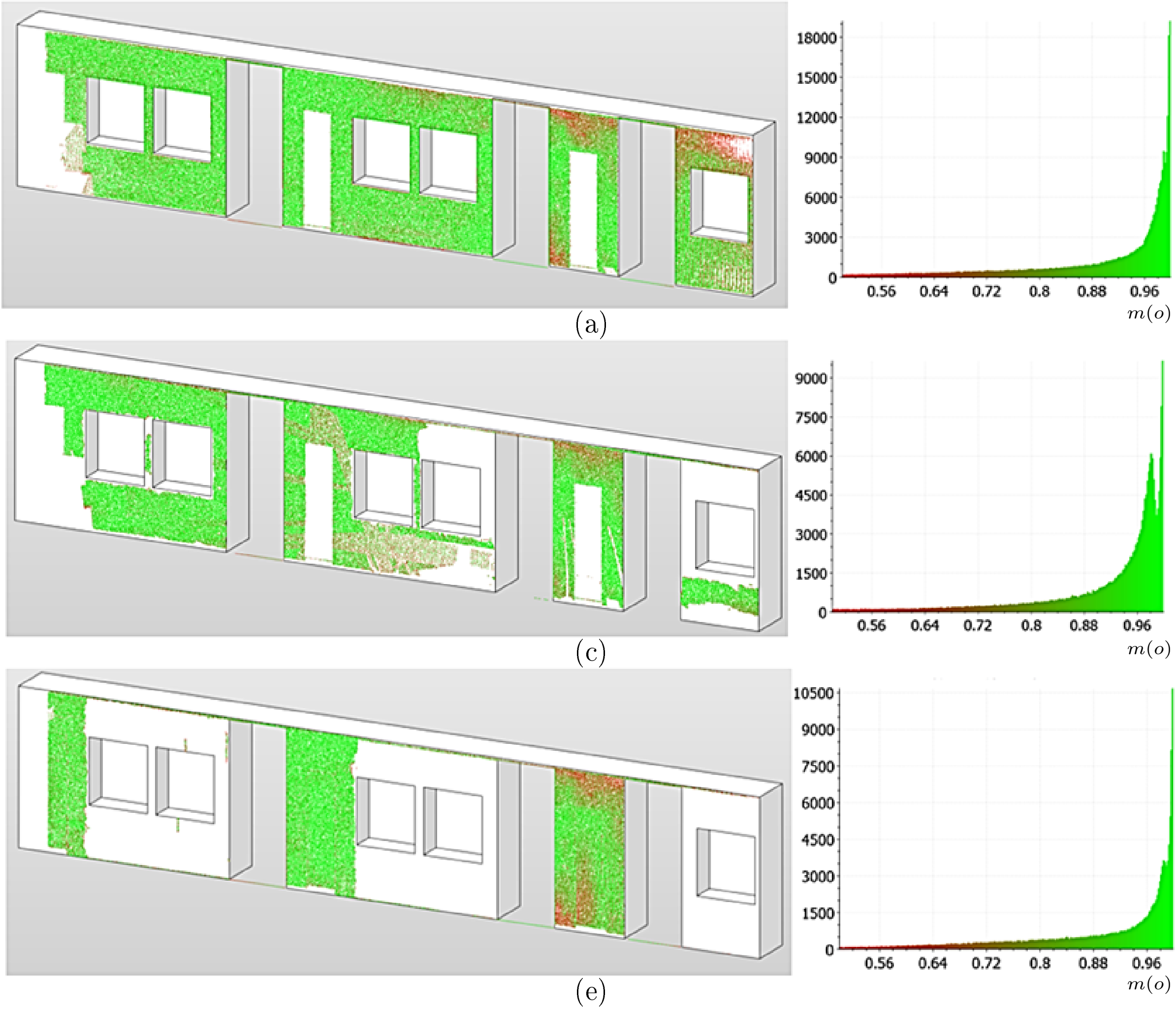

Figure 7.8: Results of point-to-BIM verification for construction site 1 and BIM version 1: a) belief masses of TLS epoch 1, b) belief masses of TLS epoch 2, c) belief masses of TLS epoch 3.

distance between the scanner source **S** and the wall, and this in turn results in a weak overlap of neighboring point clouds, low observational redundancy and critically low incidence angles. A low angle between incoming laser beam and a surface normal causes incomplete object sampling and usually a significant decrease in measurement accuracy due to noise. This common weakness of indoor point clouds is clearly noticeable in the point cloud-to-BIM verification using belief functions. While the parameters setting described in Sec. 6.3.1 brings very good results for reasonable scanning configurations i.e. approx. orthogonal incidence angles, it causes conspicuous results for geometrically weak configurations as depicted in Fig. 7.10. In case of a low incidence angle, the laser beam runs very close to the wall. The transverse distance d_y from the ray $\mathbf{r}$ to the wall is so small that query points $\mathbf{Q}_n$ located in the negative range of the longitudinal distance d_x appear to be traversed and are therefore classified as *empty*.

In order to compensate for this effect, the parameter c which affects the longitudinal extend of occupied space has to be increased e.g. by factor 2-3 (Fig. 7.11). It should be noted that a user must decide for himself in each individual case whether weak data should be compensated for by parameter adjustment, or whether areas of low quality should be marked as suspicious and therefore discarded. A compensation of belief assignments in case of too low incidence angles from

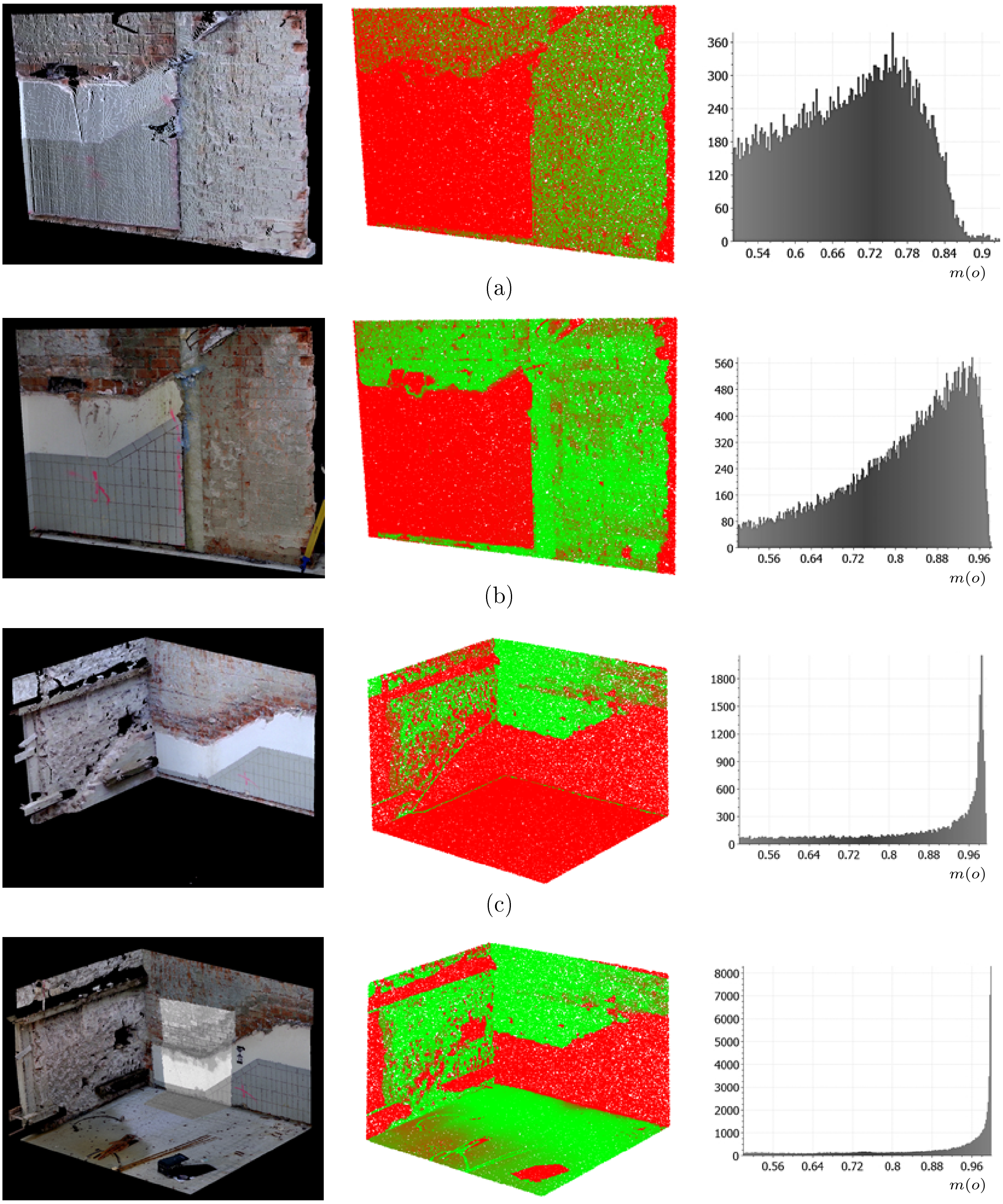

(a)

(b)

(c)

(d)

Figure 7.9: Results of point cloud-to-BIM verification for construction site 2: a) and b) show TLS point clouds, visualizations of magnitude and distribution of belief masses for epoch 1 and 2 for section 1 whereas c) and d) show TLS point clouds, visualizations of magnitude and distribution of belief masses for epoch 1 and 2 for section 2.

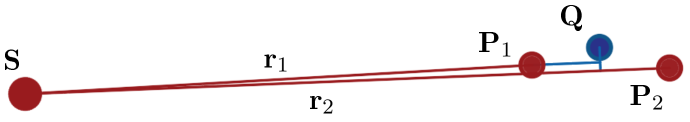

Figure 7.10: Effect of a geometrically weak scanning configuration: a low incidence angle indicating state *empty* at **Q**.

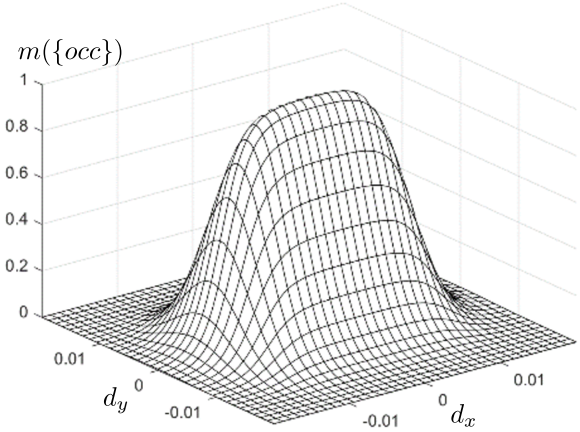

Figure 7.11: Adjusted parameters for the mass function $m(o)$ (occupied) in order to compensate for small incidence angles: $\kappa = 20000$, $\lambda = 600$ and $c = 7$.

parameter adjustment is shown in Fig. 7.12. In particular, it can be observed that the inconsistent areas are those that are farther away from the scanner stations **S** in the long, narrow hallway of construction site 1. The effect of a weak scanning geometry also becomes visible in the data of construction site 2 - section 1: The wall piece under consideration has hardly changed between epoch 1 and 2. Nevertheless, there are differences in the obtained confidences. This is due to the fact that the laser scanner could not be optimally placed in the building during the first measurements in epoch 1 due to the conditions on site. In turn, this resulted in a low incidence angle of the incoming laser beam and a low point density on the wall (Fig. 7.9.a).

7.3.3 Results of empirical dense cloud evaluations

Individual uncertainty information is important for the evidence based reasoning approach presented in Chapter 5. In case of using photogrammetric dense points for a geometric verification, these uncertainty information is not accessible. In order to verify whether the uncertainties for tie points as sparse cloud from bundle adjustment can be used to infer the uncertainty of DPs by spatial interpolation, an empirical evaluation based on TLS point clouds and the M3C2 algorithm was performed as described in Sec. 6.3.4.

Table 7.6 provides detailed numerical results of the M3C2 calculations in comparison to the bundle adjustment results of the corresponding sparse cloud areas. Generally, the magnitude of the deviation d and its associated significance threshold follow the pattern that results from the interrelation of scanner-object and camera-object distance, mean local tie point residual and registration error. The diagram in Figure 7.13 illustrates this correlation. From the distinct evaluation of subsections, it is evident that the overall TP accuracy alone is not meaningful to the overall DP quality. Rather, DPs accuracies and corresponding belief assignments should be

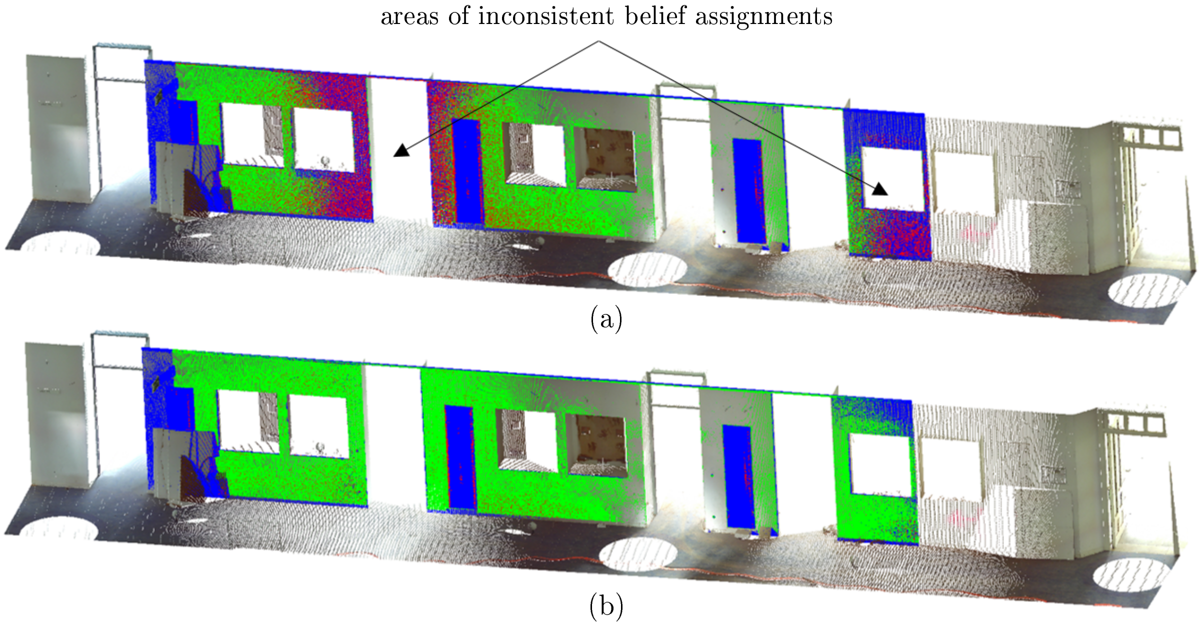

(a)

(b)

Figure 7.12: Compensating TLS geometry on evidence based BIM verification: a) point cloud-to-BIM verification result with original parameter setting, where areas with low incidence angles are erroneously classified red = empty, b) point cloud-to-BIM verification result with adjusted parameters for the mass function $m(o)$ (occupied) in order to compensate for small incidence angles: $\kappa = 20000$, $\lambda = 600$ and $c = 7$.

estimated from the individual σ of local tie points and point densities, as these best reflect the local geometric quality of a dense cloud as depicted Fig. 7.14.

7.3.4 BIM verification using image sensors

The geometric verification method based on image data named *Pho-to-BIM* verification was developed in Sec. 5.1.2 and applied on three photogrametric data sets of indoor construction sites that were introduced in Sec. 6.3.3. As the point-to-point distances of large photogrammetric scene captures may strongly vary, which makes it difficult to model belief assignments homogeneously, it is reasonable to conduct the geometrical verification for manageable sub-areas. Additionally, in the sense of a BIM compliant building model as an object-oriented spatial database system, the photogrammetric points are also considered group-wise as closed units characterizing certain spatial objects. Therefore, the geometrical verifications were performed on five subsections, which are assigned individual wall objects, i.e. TPs and DPs were pre-selected based on spatial queries with the BIM.

In addition to the parameter setting of the belief functions, the *Pho-to-BIM* verification result is also affected by the sampling resolution of the BIM object's surface. In order to decide for a density of query locations $\mathbf{Q}$, there were mainly two aspects to consider: First, the number of $\mathbf{Q}$ was chosen such that transitions between different accuracies and gaps in the dataset could be reliably revealed, i.e. the object sampling sufficiently reflects the real conditions. Second, the number of $\mathbf{Q}$ was reasonable in terms of processing time and the BIM's level of detail (Sec. 5.4). The sampling distance for $\mathbf{Q}$ was chosen to be 1 cm for the conducted experiments. A comprehensive documentation of the input parameters for the investigated subsections, including accuracy assumptions, point-to-point distances and inferred parameters κ, λ and c can be found in the upper rows of Tab. 7.7.

Table 7.6: Results of empirical dense cloud evaluation: for scenarios 1-3 using TLS point clouds and M3C2 approach

Scenario	**1 (interior)**		**2 (conversion)**		**3 (gutting)**
Laser scanner	Faro Focus 3D		Z+F Imager 5016		
	Ranging err.	2 mm	Lin.err.	1 mm + 10 ppm/m	
	Noise	0.3-0.4 mm	Noise	0.2 -0.3 mm	
Scanner-object distance	2-4 m		3-6 m		5-13 m
Camera-object distance	2.5-4.5 m		4-7 m		5-13 m
Mean σ TP from BA	9.6 mm		2.8 mm		2.7 mm
Control points	5		4		7
Registration error (reg)	10 mm		1 mm		3 mm
Section	**1.1**	**1.2**	**2.1**	**2.2**	**3**
Number of scan points	74,000	110,000	5.8 mio	2.2 mio	4.5 mio
Number of dense points	4.8 mio	3.9 mio	5.5 mio	4 mio	3.1 mio
Mean local σ TP	14 mm	19 mm	5 mm	11 mm	8.5 mm
M3C2 dist. ±1mm	18%	10 %	44%	16%	4%
M3C2 dist. ±5mm	61%	34%	92%	63%	29%
M3C2 dist. ±10mm	84%	59%	97%	87%	81%
Mean dist. uncertainty	20 mm	21 mm	2.4 mm	2.6 mm	6.8 mm
Significant deviations	$\lvert d \rvert > 19$mm	$\lvert d \rvert > 20$mm	$\lvert d \rvert > 2$ mm	$\lvert d \rvert > 2$ mm	$\lvert d \rvert > 6$mm

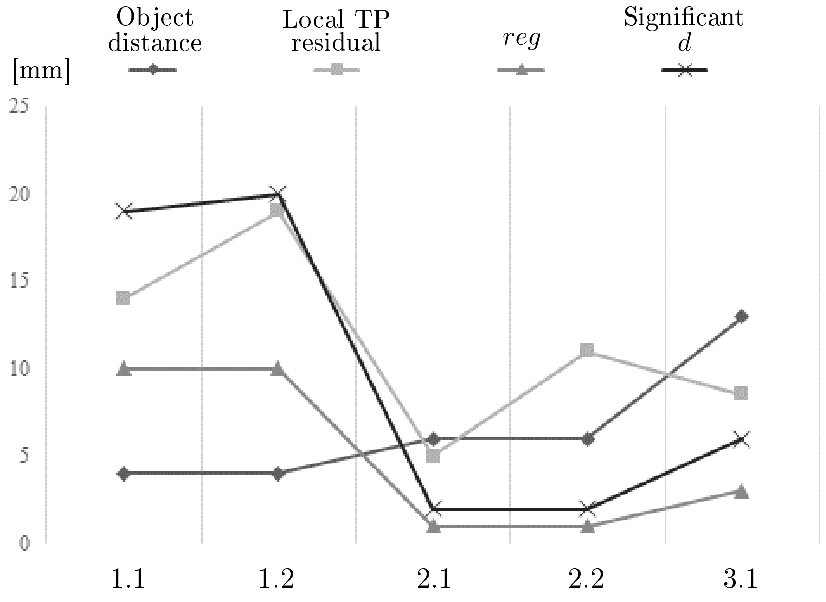

Figure 7.13: Correlation of influencing parameters on M3C2 results: there is a correlation between scanner-object and camera-object distance, mean local tie point residual, registration error and the according magnitude of differences d assumed to be significant.

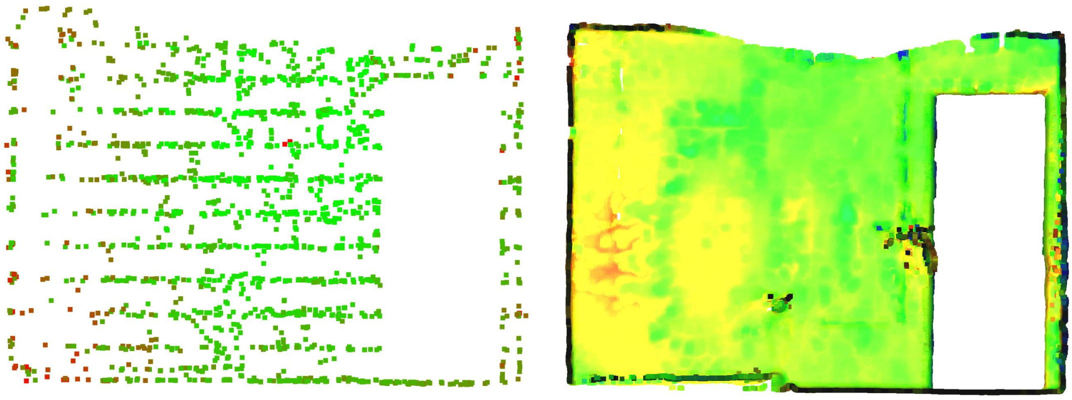
(a) (b)

Figure 7.14: Empirical evaluation of dense point quality for section 1-1: a) tie points from BA (green color indicates high accuracy), b) dense points from stereo matching colored with M3C2 distances to TLS point cloud (green color indicates low distances).

For each $\mathbf{Q}$ of a BIM object, its belief mass is calculated from its neighboring TPs and DPs. Both tie points $\mathbf{X}^{TP}$ and dense points $\mathbf{X}^{DP}$ deliver metric values for d_x and d_y representing variables of the mass functions according to Eq. 5.3 and 5.13. The belief committed to the singeltons $m(\{occ\})$, $m(\{emp\})$ and $m(\{U\})$, resp. $bel(\{occ\})$, $bel(\{emp\})$ and $bel(\{U\})$ as a result of processing d_x and d_y in the belief functions is to be balanced based on the individual accuracy of the associated DP or TP and the BIM's LOA requirement by applying Eq. 5.24. Then, Dempster's Rule allows for the combination of multiple balanced belief masses $bel()_{LOA}$ in an arbitrary order, as the join operation $\oplus$ is commutative and associative (Eq. 5.14 and **??**). Table 7.7 shows the amount of confirmed query locations $\mathbf{Q}$ for the five subsections, each for an accuracy requirement of LOA 40, LOA 30 and LOA 20. An according graphical representation is given by Fig. 7.15.

Sections 1.1 and 1.2 of scenario 1 both represent rough brick walls with MEP (Mechanical, Electrical and Plumping) installations under construction and show similar *Pho-to-BIM* verification results. The given as-built BIM was derived from a former 3D reconstruction in an early construction phase and is thus considered to be compliant with LOA 20, which corresponds to $2\sigma = 5\,\text{cm}$. This LOA was confirmed 36 % and 29 % and the uniform spatial distribution of confirmed $\mathbf{Q}$ suggests that no tilting or strong deformation is to be assumed at the wall objects. Due to the fact that the datasets of scenario 1 do not even a tiny bit confirm a higher LOA, it is clear that the TPs and DPs do actually deviate form $\mathbf{Q}$ in the magnitude of LOA 20 and that the quality of the photogrammetric scene capture performed with the IPhone camera simply does not allow for more sophisticated geometric analysis.

In contrast to the photogrammetric point measures of scenario 1, those of the sections 2.1 and 2.2 of scenario 2 do commit some amount of confirming belief masses to two LOAs, namely LOA 20 (44 % and 18 %) and LOA 30 (11 % and 13 %). Since the standard deviation of section 2.2 is worse than that of section 2.1 by a factor of 2 (see Tab. 7.7), it is not surprising that the percentage of confirmation is much lower here. Scenario 2 had already been subject of a former as-built measurement with walls in their final condition, which is why the given BIM is supposed to be LOA 30 compliant $2\sigma = 1.5\,\text{cm}$. The latest photogrammetric 3D point clouds show the scene which is now composed of partially plastered walls where covering and wall papers had been removed in the course of the ongoing indoor conversion project. Therefore, deviations that were

Table 7.7: Results of geometric verification based on images: *Pho-to-BIM* verification conducted on five subsections of the test scenarios 1-3.

Scenario	**1**		**2**		**3**
Section	**1.1**	**1.2**	**2.1**	**2.2**	**3**
BIM LOA	20	20	30	30	40
Number of **Q**	49,000	35,000	120,000	80,000	210,000
Number of TPs	1,564	810	3,675	766	2,599
TP-to-TP distance	5 cm	5 cm	8 cm	16 cm	15 cm
Mean σ TP	14 mm	16 mm	5.6 mm	9.8 mm	7 mm
TP parameters κ; λ; c	70,000; 1,500; 4	70,000; 1,500; 4	75,000; 1,500; 4	45,000; 1,500; 4	25,000; 1000; 4
Number of DPs	4.7 mio	3.9 mio	5.5 mio	3.8 mio	2.7 mio
DP-to-DP distance	2 mm	2 mm	1.5 mm	3 mm	4 mm
Mean σ DP	11 mm	20 mm	5.5 mm	10 mm	8.3 mm
DP parameters κ; λ; c	65,000; 2000; 4	65,000; 2000; 4	70,000; 2,500; 4	30,000; 2000; 4	25,000; 1500; 4
Confirmed LOA 40	**0 %**	**0 %**	**0 %**	**0 %**	**0.4 %**
Confirmed LOA 30	**0.6 %**	**0 %**	**10.9 %**	**12.5 %**	**8.6 %**
Confirmed LOA 20	**36.2 %**	**28.6 %**	**44.3 %**	**12.5 %**	**8.7 %**

revealed from the *Pho-to-BIM* verification were largely to be expected and it was furthermore to be expected that there is a relatively great amount of **Q** being confirmed to be LOA 20 compliant.

The third scenario has by far experienced the largest structural changes from the last as-built survey. Although the given BIM was assigned LOA 40 with $2\sigma = 5\,\mathrm{mm}$, the gutting of the building has left only rough structures where surfaces deviate by a few centimeters from the previously modeled surface. Only in a few areas where the surface plaster has not yet been removed completely (9% of the total area) the model could still be confirmed within LOA 20 and LOA 30. Yet, due to the quality of the photogrammetric survey, mutually reinforcing belief masses and the high quality of the BIM, it is assigned some tiny amount of belief (0.4 %) confirming LOA 40.

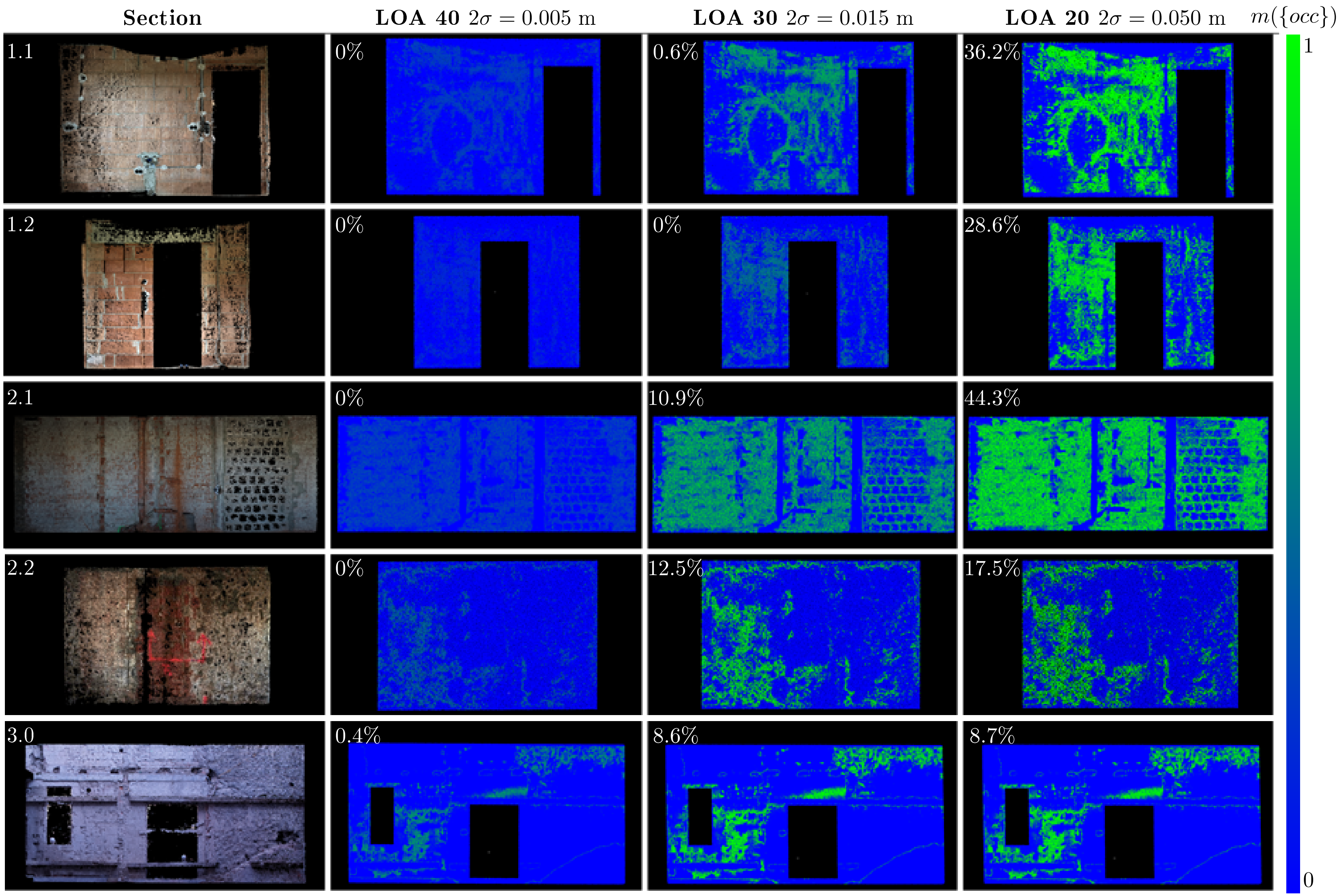

Figure 7.15: Verification results for five subsections of the photogrammetric test scenarios 1-3 (blue color indicates low belief assignments whereas green color indicates strong belief in the associated BIM's geometrical correctness)

8 Discussion

This research focuses on three aspects of geodetic tasks in the field of indoor BIM. These involve image-to-BIM co-registration, 3D point cloud based change detection and the geometric validation of a given building model. The previous chapters introduced methodologies, experiments and results in these contexts. The general findings, interpretations and outcomes but also limitations on the main research aspects are presented in this chapter.

8.1 Discussion on image-to-BIM co-registration

With the advent of spatial indoor applications such as navigation, augmented reality and change detection, the general need for self localization of mobile camera systems within a buildings interior emerges. At the same time, with the implementation and dissemination of digital planning and building, the general availability of digital building models increases. The idea of utilizing the fact that the indoor environment is already known in the form of a BIM for visual localization is obvious. While edge extraction and line matching are well investigated research topics in the field of image-to-model matching, utilizing a statistically uncertain BIM for the co-registration of images for change detection has hardly been addressed yet. The potential accuracy of an image-to-BIM co-registration was investigated based on the constraint optimization model presented in Chapter 3 and experimental parameter estimations utilizing synthetic data as ground truth according to Sec. 6.1 and 7.1.

The tested configuration of a roughly oriented synthetic image and line references resulted in an optimized image-to-BIM co-registration provided the assigned BIM-edges were modeled at least LOA 30 compliant. According to the U. S. Institute of Building Documentation, LOA 30 and LOA 40 are the most common ones that apply for BIM related objects in indoor environments, such as doors, walls and windows. Therefore, it can be concluded that the proposed method for image-to-BIM co-registration is suitable for an optimized alignment between image and BIM as a prerequisite for change detection under explicit consideration of image and BIM related uncertainties. However, with a view to further refinement of the proposed method towards practicability, there are some points and remarks open for discussion:

- ❑ Although BIM elements should be modeled with some level of geometric accuracy, and the USIBD suggests not only providing LOA information but also applying certain methods for validation during as-built documentation, BIM-related geometry and LOA assignments should not be considered completely error-free. Instead, it has to be expected that some model edges are faulty regardless of their associated LOA definition. Additionally, the correspondence analysis of model edges and detected straight lines in an image will in some cases and situations fail and lead to miss-matches. With these possible difficulties in mind, the adjustment procedure shall be improved in a way towards robustness. In case of both local imprecisions and gross errors within the data, an option for reasonable re-weighting observations is needed. Additionally, the estimation procedure is to be extended to a robust optimization by the embedding into a RANSAC loop. A hierarchical estimation pipeline with the ability of revealing observational errors and the verification of the reference BIM's geometry that is used for the alignment of an image should be implemented.

- The test scenario reflected typical indoor conditions with a general image view on walls, windows and some indoor installations. These objects commonly provide a sufficient number of edges for an image-to-BIM co-registration. Nevertheless, in practice, these optimal geometric references may not always be available. Sub-optimal conditions are to be expected in case of a too large image scale as a result of a short distance between camera and object, narrow and confined areas, e. g. in a hallway and in the presence of furniture and clutter that hide object edges. Although the experiments on synthetic data have shown that the image-to-BIM co-registration works in principle and produces sufficiently accurate results, it has not been investigated yet how weak geometric configurations can affect the estimation. The experiments still lack an investigation of critical geometric configurations. These would include two cases in particular: i) A small number of geometric references and ii) uneven spatial distribution of geometric references, e.g. cluster of lines and edges with uniform orientation.

- The co-registration was applied for a single digital image with a BIM. However, the method shall be applicable for a series of consecutive images as it is already assumed that the coarse orientation of the image sensor results from SfM and visual odometry. In order to obtain a robust solution for a series of overlapping images, the constrained estimation has to be extended to a global optimization. This requires an adjustment of the functional model, since geometric correspondences are treated as observations and receive numerical corrections in order to achieve minimal contradictions for a single image. Given a fixed geometric frame, it should be possible to co-register a set of images optimized for the model. By combining relative orientation over the image sequence using SfM and absolute co-registration with the model at selected image frames, it would be possible to bridge regions of weak geometric reference. In the sense of global optimization, the principle of loop closure should also be introduced.

8.2 Discussion on point cloud based change detection

Due to their high resolution, close-range laser scanning point clouds hold immense information potential that is rarely exploited because there is often still a lack of suitable application-specific and, above all, automated strategies for interpretation and analysis. The voxel based method presented in Chapter 4 is an efficient method for occupancy based change detection for progress monitoring and AEC applications. Due to the fact that it exclusively utilizes geometric relations between the scanner viewpoint and 3D points, it is considered extremely robust. The change detection results that were obtained from TLS data of real indoor construction sites demonstrated the practical applicability of the proposed high resolution voxelization.

A voxel based approach inherently involves a discretization and a loss of geometric information. But that is precisely why it is so remarkable that there are still many details to be seen in the resulting classified voxel clouds of Sec. 7.2. Amongst others, these details refer to reinforcement steel, sharp breakoff edges, construction props and thin iron rods as part of a fall protection. A voxel size of 1 cm leads to a maximum point shift error of $d = 0.86$ cm (Eq 4.1). At this point, it is assumed that the measurement and co-registration error of the original TLS measurement is much smaller than the discretization effect, although systematic and gross errors may occur but are not considered in the progress monitoring phase. The level of voxel-detail still enables a re-modeling of the entire scenes only from voxel, considering LOA 30 for absolute measurement accuracy

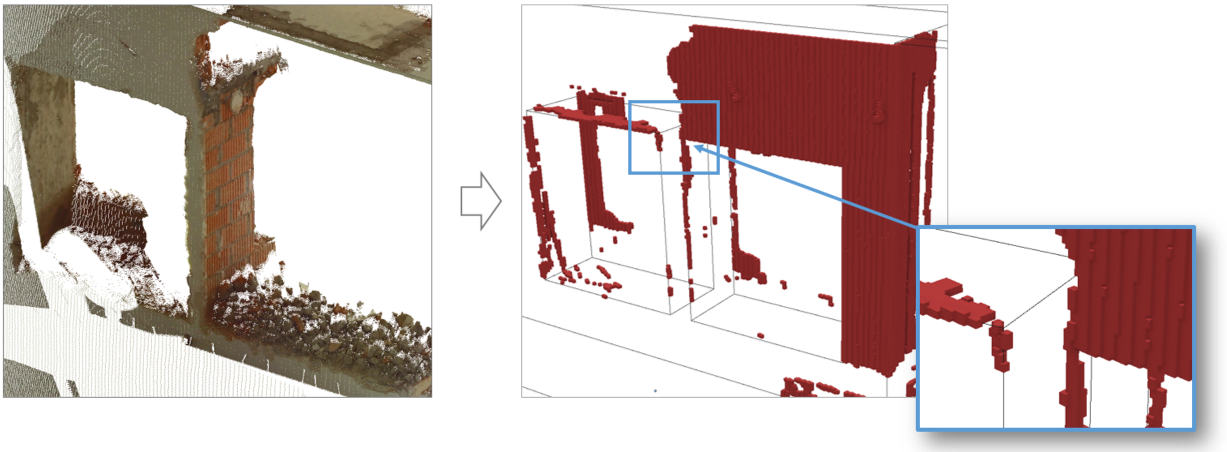

Figure 8.1: Combined analysis of volumetric voxel within a spatial building database: original, uninterpreted 3D point cloud (left) and voxel classified as *demolished* prior to a 3D intersection operation with the geometric model of the wall.

according to the USIBD. Relative measurements according to the LOA specification require a tolerance computation either using the squared or linear approach (Eq. 4.4 and Eq. 4.5). In case of 1 cm voxel size, both of them exceed LOA 30 but rather meet the relative accuracy requirements of LOA 20, which is for service installations, equipment, furnishings and building sitework still sufficient [USIBD, 2019]. In the experiments however, only 1 cm voxel size was tested on standard scanning resolution of 6 mm point-to-point distance at 10 m scanner-object distance. This scan configuration was chosen because it is considered a good compromise in terms of worklad on site[*] and data quality. In further experiments, the scan resolution could be doubled while the voxel size is halved in order to achieve even more detailed voxel clouds for change detection. Depending on the specific accuracy requirements, the presented high resolution voxel approach can be used as a stand-alone application for progress monitoring with non-maximum accuracy requirements or as a pre-processing step for the detection of areas of interest towards a single point evaluation as introduced in Chapter 5.

Although the reliable classification of construction site areas in *disappeard*, *new* and *confirmed* is valuable spatial information, the process of construction progress monitoring is still not considered complete. As the results of Sec. 7.2 show, the task of change detection was solved robustly and well on the part of the geodesy. Nevertheless, there is a need for research on the interface between geodetic measurement data and according result interpretations, and the combined analysis with the building database. In order to utilize the full potential of BIM, classified voxel should be used for continuously updating a BIM' geometry in the sense of permanent monitoring. Volumetric voxel could be used for spatial intersections with BIM objects. In this way it would be possible for example to document the demolition of a wall "as-is" (Fig 8.1) in order to enable spatio-temporal near real time BIM. Nevertheless, the integration of massive 3D data in the form of voxel requires the implementation of 3D indices, 3D topology and a 3D spatial query language as proposed by Borrmann et al. [2006].

---

[*] The configuration resulted in a scan time of about 5-6 minutes per station.

Table 8.1: Conversion of confidence levels using a standard normal table.

LOA	σ $[mm]$	confidence				
40	2.5	0.412	0.683	0.750	0.850	0.955
50	0.5	0.087	0.159	0.182	0.228	0.304
30	7.5	0.901	0.997	0.999	≈ 1	≈ 1
20	15	0.999	≈ 1	≈ 1	≈ 1	≈ 1

8.3 Discussion on geometric BIM verification

The geometric correctness of a building information model is very important for the quality of any analysis and further planning for project management that is based on it. The model is only as valuable as its correspondence to the real object. However, there are still no established methods, specifications and guidelines for the geometric validation of a BIM for 3D point clouds that go beyond a simple point-to-model distance criterion. For this reason, this research gap was addressed with a novel method for geometric validation. The conducted experiments show the practical applicability of the developed method in this research. In the following discussion of the results, a distinction is made between geometric verification based on terrestrial laser scanning and photogrammetric 3D point clouds.

Decision making with TLS point clouds and different LOA

A BIM can be assigned a certain level of geometric accuracy. Thus, any BIM compliant model verification also has corresponding accuracy requirements that must be taken into account. On the one hand, the accuracy of the measuring device, i. e. a terrestrial laser scanner in the experiments, is important for subsequent evaluations. It must be ensured that the measurement accuracy meets at least the case specific accuracy requirement defined by the LOA guideline. Otherwise, the verification result based on belief functions must be downgraded respectively, since the confidence of belief does not meet the certain demands. This is the case when an LOA 50 model is to be evaluated with conventional TLS. A TLS related standard deviation $\sigma_{\mathbf{P}} = 2.5\,\text{mm}$ is assumed. This σ corresponds to LOA 40 and relates to a confidence of ≈ 0.68. However, LOA 50 requires $\sigma_{\mathbf{Q}} = 0.5\,\text{mm}$. Even a maximum belief in a hypothesis that was acquired with a point cloud from TLS does not sufficiently confirm a maximum accuracy BIM. This is shown numerically in Table 8.1: assuming a belief of 0.95 at $\sigma_{\mathbf{P}} = 2.5\,\text{mm}$ corresponds to only 0.30 when $\sigma_{\mathbf{Q}} = 0.5\,\text{mm}$ is requested. Practically such a demanding level of accuracy is very rarely expected in real projects. In practical applications, it can be assumed that essential interior elements such as doors, windows and walls are modeled LOA 30 or 40 compliant [USIBD, 2019]. Thus, in most cases, TLS with a common quality is suitable for the verification of a BIM. In the best case, the measurement accuracy is even significantly higher than that of the model under test. In the experiments and results of Sec. 7.3.1 and the assumed accuracy of the LOA 30 BIM could be almost completely confirmed by the laser measurements.

Point cloud-to-BIM verification using TLS

The two processed datasets of real construction sites reflect typical indoor scanning conditions and are representative for the demonstration and evaluation of the presented method in practical use. The optimal set up of the parameters of the belief functions was determined, such that the experimental point cloud-to-BIM verification resulted in proper joint masses with the associated model accuracy. The standard deviation of the TLS measurements is an a priori assumption and input parameter for this method. Achievable TLS measurement accuracies and the effect of systematic errors is a topic that is already well investigated by other researchers such as Gordon & Lichti [2007], Wujanz et al. [2018] and Holst et al. [2018]. In practical, observational redundancy, geodetic network design, scanning geometry and noise have an effect on the accuracy which is considered in the proposed method. Weak scanning configurations are revealed in the phase of point cloud-to-BIM verification. Noise will be assigned low belief masses, as following the proposed parameter setting, the longitudinal and transverse distance (d_x and d_y) to query positions ($\mathbf{Q}$) will be too large. A generally sufficiently large number of correct scan points will in turn compensate for this effect. Further more, suspicious scanning configurations, which, from experience, entail an increased risk of low point qualities, are revealed from the parameter c of the belief functions (5.3), which affects the longitudinal extend of occupied space. This effect becomes visible in case query points $\mathbf{Q}$ are classified as *empty* if $c = 2$ (Fig. 7.3.2).

While the special properties of surface materials can cause systematic errors during scanning that affect the result, more obvious errors such as from clutter, strong measurement noise or point artifacts have only little effect on the point cloud-to-BIM verification method. These error sources can be handled in the phase of pre-processing by applying the high resolution voxel approach of Chapter 4. A small voxel size (e.g. 1 cm for high resolution indoor TLS) and the threshold parameter T, which controls the minimum number of laser points within a voxel for being considered as relevant for further processing. In the phase of point cloud-to-BIM verification, remaining noise and false returns will be assigned low belief masses, which are compensated by the usually great number of proper laser points. Related strategies for dealing with clutter and occlusions in building point clouds can be found in Maalek et al. [2018] and Pexman et al. [2021].

Pho-to-BIM verification using images

According to the USIBD, the specification of a building-object's level of geometric accuracy is essentially important for meeting quality requirements in context of the digitization of construction and BIM. Reliable confirmation of the level of accuracy of exterior walls and interior partitions, as demonstrated Sec. 6.3.3, 6.3.5 and 7.3.4 is therefore valuable for the AEC practice. The detailed results of photogrammetric geometry verification are to be interpreted from different points of view:

- ❑ Accuracy: The results of the three real construction datasets show, the given geometric models could be confirmed on the basis of the image measurements to certain proportions mostly within LOA 20 and LOA 30. As expected, areas where the deviations were too large clearly correlate with areas of insufficient measurement accuracy, where there is just not enough confidence (e.g. section 1.1) and insufficient consistency between model and reality, e.g. due to ongoing construction work (section 3). Furthermore, a significant loss of belief is observed each in the corners of the wall objects, where the multi-view geometry is considered sub optimal as a result of a limited range of sensor motion in this areas. Prior to measurement, predictions could be made about the achievable accuracies based on the given BIM. For most practical applications and BIM-object categories, compliance with LOA 30 is commonly satisfying and the evaluated experiments show, that this LOA can actually be verified with professional image sensors and reasonable effort. Future developments in the field of autonomous indoor-UAVs are particularly promising regarding efficiency and safety. However, LOA 40 and highest LOA 50 with $2\sigma = 1$ mm are very hard to verify by photogrammetric scene captures on site as this would require a significantly higher quality of ground control points, camera calibration and multiple view geometry. In order to meet these requirements, tests under laboratory conditions should be conducted prior to on site surveys.

- Resolution and generalization: In the experiments, the verified BIM objects are geometrically characterized by flat, continuous wall surfaces that are sampled according to the agreed resolution. Optimal resolution is achieved when the point-to-point distance of the measurement and the number of sample points correspond to an application's required level of detail. Although in the scenarios 1-3 only the geometric primitive "planar surface" was searched for, the resolution of section 2.1, for example, would be high enough to also reveal finer structures such as wall recesses for pipes, if targeted searches were performed. The problem however is, that MEP related structures are not true to shape modeled within a BIM, but commonly heavily generalized and represented only by symbolic (Fig. 8.2). Hence, an exclusively geometry based point-to-model verification is not reasonable but should be combined with semantic image interpretation, e.g. deep learning supported object detection.

- Representation of uncertainty: A BIM-compliant 3D model of a buliding follows certain rules of procedural and parametric modeling. The specification of geometric primitives in addition to topological constraints ensure extensive model validity and data consistency. However, such geometric restrictions limit the ability of modeling true to shape, based on an as-built scene capture for BIM. As a result, detected deviations between model and reality from a *Pho-to-BIM* verification may not necessarily lead to a geometrical update of the BIM. Instead, the revealed uncertainty information could be stored as an additional attribute within the object oriented spatial database. By extension, photogrammetric digitization of MEP installations would also relate to these uncertainty-attributed base components. If for example a power outlet and according electric cable are to be captured by photogrammetric 3D point measures from forward intersections, although despite potentially high precision, these newly created reference points would lead to a violation of topology rules as they do not perfectly join the planar base component "wall". Therefore, information from interior work phase should be projected onto their uncertainty-attributed base components and extended with uncertainty attributes themselves. For example, augmented reality applications in which cables underneath wall plaster are visualized could be enriched with reliable accuracy information so that, for example, a cable is not accidentally damaged during drilling.

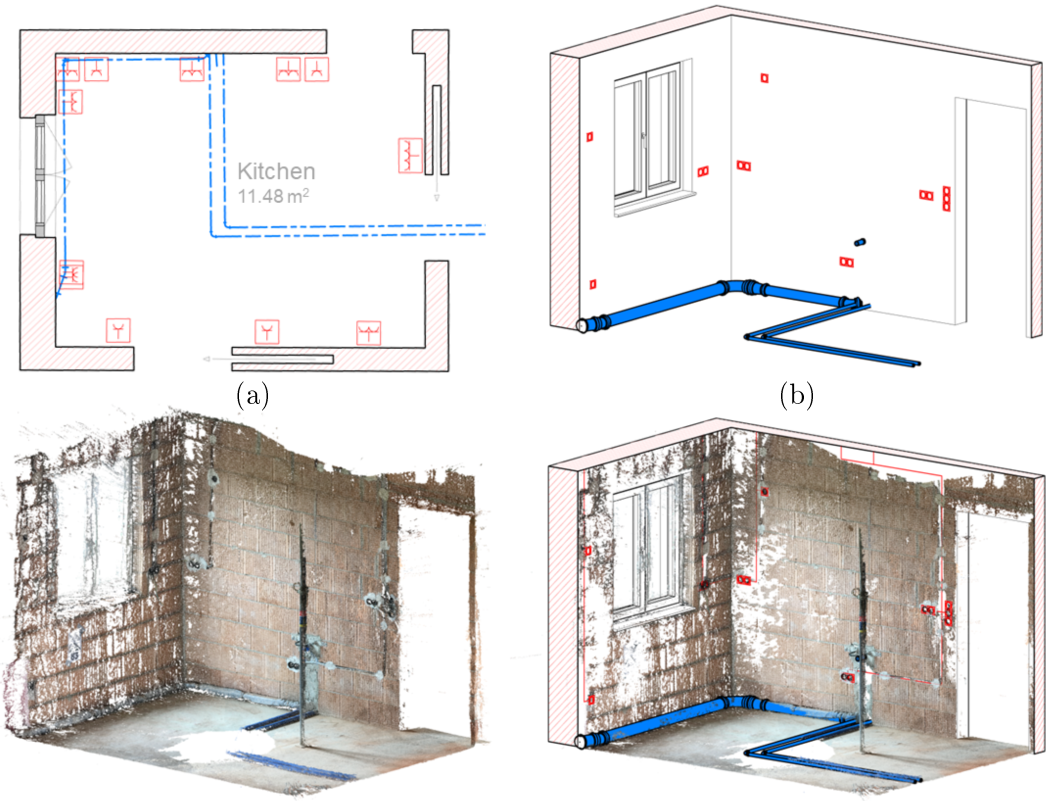

(a) (b)

(c) (d)

Figure 8.2: Room with MEP installations: a) Floor plan with general electrical and plumbing symbols, b) 3D visualization of the initial BIM, c) Image based 3D point cloud, taken at the time when the walls had open slots with cable and cavity wall boxes for electrical outlets to be installed. In addition, the as-built capture already documents the horizontally laid drainpipe and pipes for water supply in the kitchen, d) Updated BIM showing the as-built condition of the electrical cables in the walls, overlaid with the georeferenced point cloud.

9 Conclusions and Outlook

This concluding chapter summarizes the research topic addressed in this thesis. In particular, the most important results are discussed, the answering of which was set as an objective at the beginning. Finally, the thesis ends with a concluding remark and an outlook on future developments and research in this field.

9.1 Conclusions

As-built models are the next evolutionary step and form the basis for rapid action by decision makers. In this context, many engineering companies have found a new focus in their range of services. In "as-built" surveying for BIM, they rely on high-resolution 3D point clouds from TLS and photogrammetry. The methods presented in this thesis refer to image-to-BIM co-registration, progress monitoring and the geometric verification of a given building model. They are based on the geometric evaluation and interpretation of as-built image and point cloud data and consider the individual statistical uncertainties of geodetic measurements and the geometric uncertainties of a reference BIM according to the LOA specification.

Regarding these topics, three research questions were posed at the beginning of this thesis, which will now be answered in the following.

Research question Ia: To what extend do geometric uncertainties of BIM related reference objects effect the accuracy of an image-to-model co-registration?

The aspect of image-to-model co-registration in indoor environments was addressed by the development of a constraint estimation model based on corresponding straight lines in an image and BIM related model edges, which serve as geodetic references. Experiments using synthetic data as ground truth were carried out to assess the effects of different levels of geometric uncertainty. In order to not only evaluate the numerical behavior of uncertainties, but also to be able to assess the practical applicability, the simulations have referred to the Level of Accuracy specification for BIM. The results showed that by using the proposed method, a coarse image orientation can be optimized provided the reference BIM can be assigned to LOA 30 or higher. According to the U.S. Institute of Building Documentation LOA 30 is the most common one that applies for indoor BIM objects. Thus, it can be concluded that the geometric building model can serve as a geodetic reference itself in the proposed way.

Research question Ib: Is the geometric quality of common BIM-compliant interior models sufficient to serve as a geodetic reference itself and to make statements about the compliance with metric tolerances?

Considering the principles of variance propagation, the accuracy of subsequent measurements is limited by the accuracy of the image-to-BIM co-registration. When considering whether metric tolerances can be confirmed based on an image-to-BIM co-registration, a distinction must be made between two cases. First, metric tolerance evaluations in context of engineering and construction require a confidence interval of the measurement to be significantly smaller than the specified tolerance of the object to be tested. An LOA 50 BIM would be necessary for image-to-BIM co-registration to enable the detection of material defects and workmanship faults after the manufacture or installation of individual components during construction phase for example according to ISO 1803 and DIN 180202. In practice, however, LOA 50 models are not expected to actually be encountered. Second, metric tolerances in the context of building documentation according to the LOA specification refer to the acceptable tolerance range for the building measurements acquired during the "scan-to-BIM" acquisition process, and the tolerance range for the representation of these measurements in the model. The LOA specification not only takes up common measurement accuracy standards (DIN 18710), but especially provides detailed guidance on the representation, modeling and verification of as-built data. According to the LOA standard, LOA 30 (15 mm) and LOA 40 (5 mm) can be assumed for interior constructions and finishes (e.g. interior doors, wall finishes and flooring). In contrast to the requirements in building construction, an indoor BIM itself can be used for common tolerance requirements in as-built documentation according to the USIBD.

Research question II: What are the limits of automated 3D point cloud based change detection in terms of detail and resolution? Is it sufficient for interior building documentation with associated accuracy requirements?

In this thesis, a 3D point cloud based change detection was realized by high resolution 3D occupancy modeling using voxel. 3D point clouds in a common resolution of 6 mm point-to-point distance at 10 m scanner-object distance that were obtained from terrestrial laser scanning were used for the experiments on real construction sites. A voxel size of 1 cm leads to a reasonable number of classified voxel for change detection analysis and a maximum point shift error of ≈ 0.86 cm. Given this discretization error, an absolute re-modeling of the 3D construction scene from voxel centroids is possible up to LOA 30. Regarding relative tolerance computations from voxel clouds exceeds LOA 30 but meets LOA 40 requirements, e. g. checking the distance between two walls during construction progress monitoring.

Research question III: Which accuracy classes for BIM can still be verified with sufficient confidence using common laser scanners and RGB cameras?

A building's interior is a quite challenging environment for the verification of geometry and detected changes. A variety of influencing factors has to be considered on a geodetic measurement in order to reveal spatial information with sufficient confidence for decision making in context of BIM and AEC applications. These involve co-registration/ georeferencing, geodetic network design, observational redundancy, noise and random errors but also the resolution in terms of point sampling distance. In order to manage the uncertainty and fuzziness of geodetic point measures, a mathematical expression of belief masses within the frame of Dempster-Shafer evidence theory was developed in this thesis. The experiments were based on different laser scanners and RGB cameras, including an indoor drone and a smart phone camera as these devices and sensors represent typical state of the art mapping systems on both professional and consumer level. From the belief function setup and the obtained results of real construction site data it can be concluded that TLS can verify a BIM's geometry up to LOA 30, whereas the photogrammetric approaches yielded a confirmation in the range of LOA 20-30 for a smart phone, up to LOA 40 when utilizing a professional system camera.

9.2 Outlook

In the AEC industry, there is a great need to implement digital methods and to therefore verify the quality of building information models in order to conduct valid analysis, progress control and planning. In this context, the aim of this thesis was to develop methods to further advance progress monitoring and evaluation, particularly in indoor environments. This goal was achieved through the successful development of scientific methods and research in the fields of image-to-model co-registration, point cloud based change detection and geometric BIM verification. Considering the research results and the current limitations of the proposed methods, further aspects should be investigated and improved in the future.

The novel method for geometric verification is based on the combination of Dempster-Shafer theory and 3D point clouds from laser scanning and photogrammetry. The new approach is particularly capable to manage and infer individual uncertainty information of both, the image measurements and a pre available BIM according to the LOA specification. For the verification, there is no 3D reconstruction necessary, no pre-processing (e.g. outlier removal) and every single point information is used. Thus, there is no discretization nor any kind of approximation of the original data. The strength of Dempster Shafer theory is decision making for practical applications from the combination of multiple evidence and the explicit consideration of ignorance. If an assumption cannot be confirmed directly, this does not automatically mean that its negation is advocated. This is a crucial advantage, because in context of as-built verification, it allows to distinguish model areas that are not confirmed because of occlusions from those that actually deviate geometrically. However, the results are sensitive to the geodetic networkdesign on site and the parameter setting of the belief functions. Therefore, the proposed method should be tested in some more construction site scenarios with varying geodetic configurations and long term monitoring. In particular, the effects of different combination rules for conflicting evidence and weighting such evidence should be investigated.

It is conceivable to upgrade a BIM's associated LOA if it is verified with sufficient belief from accurate TLS or image-based measurements. Actually, the geometry of a BIM could be updated by spatial 3D operations with voxel. In this context, progress is needed in the area of BIM-GIS (Geo Information Science) integration and enhanced functionality of 3D and especially indoor GIS frameworks, including 3D topology and level of detail structures as discussed in Borrmann et al. [2006] and Meyer & Brunn [2019]. Furthermore, modern mobile mapping systems, e.g. backpacks, (indoor) UAVs or trolleys are promising for as-built documentation and change detection. In future development, the presented approaches shall be adopted to these types of systems. In case of a mobile sensor platform, the trajectory, the motion model and the quality of the absolute orientation have to be considered in stochastic input and in the set up of the belief functions.

Generating image based 3D point clouds is quick and easy with a wide range of camera sensors and 3D reconstruction software. The developed image-to-BIM co-registration method based on BIM-edges shall be further extended and optimized for stereo cameras. In this way, a scale information would be directly obtained, which in turn, increases the robustness of the method. Either way, once a proper co-registration is achieved, the experiments of this work showed that caution is required when evaluating and interpreting photogrammetric results. Although the amount of image overlap and GCP residuals roughly indicate the quality of a photogrammetric scene capture, professionally qualified statements require the consideration of the entire bundle adjustment result. Only then it is possible to infer single point accuracies as well as to apply statistical tests in order to reveal possible outliers and systematic errors. Currently, methods for statistical analysis of photogrammetric point clouds that estimate valid confidence intervals for individual points are still lacking. Future work could be dedicated to this topic.

Finally, regarding image based techniques, an extension with semantic image interpretation and tests on the maximum assessable accuracy with regard to LOA 50 first, under laboratory conditions, shall be part of future work. Additionally, a planning of photogrammetric surveys for *Pho-to-BIM* verification based on BIM and forecast adjustments could be developed. In this way, it cloud be aimed to implement the presented methods in as-built modeling software for an optimal scene capture, a supported modeling process by kind of permanent and on the fly point cloud-to-BIM compliance checking as well as uncertainty aware analysis for BIM based on a draft towards an uncertainty extended spatial data model that supports common level of detail structures.

Bibliography

Acharya D, Ramezani M, Khoshelham K, Winter S (2019) BIM-tracker: A model-based visual tracking approach for indoor localisation using a 3d building model. ISPRS Journal of Photogrammetry and Remote Sensing, 150: 157–171.

Agisoft (2022) Dense cloud editing with confidence filter tool. Helpdesk Portal.

Aijazi AK, Checchin P, Trassoudaine L (2013) Detecting and updating changes in lidar point clouds for automatic 3d urban cartography. ISPRS Annals of the Photogrammetry, Remote Sensing and Spatial Information Sciences, II-5/W2: 7–12.

Alizadehsalehi S, Yitmen I (2019) A concept for automated construction progress monitoring: Technologies adoption for benchmarking project performance control. Arabian Journal for Science and Engineering, 44 (5): 4993–5008.

Avbelj J, Iwaszczuk D, Stilla U (2010) Matching of 3d wire-frame building models with image features from infrared video sequences taken by helicopter or uavs. The International Archives of Photogrammetry, Remote Sensing and Spatial Geoinformation Sciences, : 149–154.

Bahl P, Padmanabhan V (2000) RADAR: an in-building RF-based user location and tracking system. In: Proceedings IEEE INFOCOM 2000. Conference on Computer Communications. Nineteenth Annual Joint Conference of the IEEE Computer and Communications Societies (Cat. No.00CH37064)

Boerner R, Kröhnert M (2016) Brute force matching between camera shots and synthetic images from point clouds. ISPRS - International Archives of the Photogrammetry, Remote Sensing and Spatial Information Sciences, XLI-B5: 771–777.

Borrmann A, König M, Koch C, Beetz J, eds (2021) Building Information Modeling. Springer Fachmedien Wiesbaden.

Borrmann A, van Treeck C, Rank E (2006) Towards a 3d spatial query language. 11th International Conference on Computing in Civil and Building Engineering.

Bosché F, Ahmed M, Turkan Y, Haas CT, Haas R (2015) The value of integrating scan-to-bim and scan-vs-bim techniques for construction monitoring using laser scanning and bim: The case of cylindrical mep components. Automation in Construction, 49: 201–213.

Bosche F, Haas CT (2008) Automated retrieval of 3d cad model objects in construction range images. Automation in Construction, 17 (4): 499–512.

Braun A, Tuttas S, Borrmann A, Stilla U (2015) A concept for automated constuction progress monitoring using bim-based geometric constraints and photogrammetric point clouds. Journal of Information Technology in Construction, (20): 68–79.

Bresenham JE (1965) Algorithm for computer control of a digital plotter. IBM Systems Journal, 4 (1): 25–30.

Börlin N, Grussenmeyer P (2014) Camera calibration using the damped bundle adjustment toolbox. ISPRS Annals of the Photogrammetry, Remote Sensing and Spatial Information Sciences, II-5: 89–96.

Canny J (1986) A computational approach to edge detection. IEEE Transactions on Pattern Analysis and Machinge Intelligence, (8 (6)): 679–698.

Dai F, Lu M (2010) Assessing the accuracy of applying photogrammetry to take geometric measurements on building products. Journal of Construction Engineering and Management, 136 (2): 242–250.

DeGol J, Golparvar-Fard M, Hoiem D (2016) Geometry-informed material recognition. : 1554–1562.

Dempster AP (1976) Upper and lower probabilities induced by a multivalued mapping. The Annals of Mathematical Statistics, 38: 325–339.

Esfahani ME, Rausch C, Sharif MM, Chen Q, Haas C, Adey BT (2021) Quantitative investigation on the accuracy and precision of scan-to-bim under different modelling scenarios. Automation in Construction, 126: 103686.

Eugster H, Nebiker S (2009) Real-time georegistration of video streams from mini uas using digital 3d city models. 6th International Symposium on Mobile Mapping Technology.

Förstner W (2010) Optimal vanishing point detection and rotation estimation of single images from a legoland scene. Paparoditis N., Pierrot-Deseilligny M., Mallet C., Tournaire O. (Eds), IAPRS, Vol. XXXVIII, Part 3A, : 157–162.

Förstner W, Wrobel BP (2016) Photogrammetric Computer Vision, volume 11. Cham: Springer International Publishing.

Gehrung J, Hebel M, Arens M, Stilla U (2020) Change detection and deformation analysis based on mobile laser scanning data of urban areas. ISPRS Annals of the Photogrammetry, Remote Sensing and Spatial Information Sciences, V-2-2020: 703–710.

Gehrung J, Hebel M, Arens M, Stilla U (2022) Change detection in street environments based on mobile laser scanning: A fuzzy spatial reasoning approach. ISPRS Open Journal of Photogrammetry and Remote Sensing, 5: 100019.

Gerke M (2011) Using horizontal and vertical building structure to constrain indirect sensor orientation. ISPRS Journal of Photogrammetry and Remote Sensing, 66 (3): 307–316.

Golparvar-Fard M, Bohn J, Teizer J, Savarese S, Peña-Mora F (2011) Evaluation of image-based modeling and laser scanning accuracy for emerging automated performance monitoring techniques. Automation in Construction, 20 (8): 1143–1155.

Golparvar-Fard M, Pena-Mora F, Savarese S (2015) Automated progress monitoring using unordered daily construction photographs and ifc-based building information models. Journal of Computing in Civil Engineering, 29 (1).

Gordon SJ, Lichti DD (2007) Modeling terrestrial laser scanner data for precise structural deformation measurement. Journal of Surveying Engineering, 133 (2): 72–80.

Hebel M, Arens M, Stilla U (2013) Change detection in urban areas by object-based analysis and on-the-fly comparison of multi-view als data. ISPRS Journal of Photogrammetry and Remote Sensing, 86: 52–64.

Heuel S (2004) Uncertain projective geometry: Statistical reasoning for polyhedral object reconstruction: Zugl.: Bonn, Univ., Diss., 2002, volume 3008 of Lecture notes in computer science. Berlin: Springer.

Heuel S, Förstner W (2001) Matching, reconstruction and grouping 3d lines from multiple views using uncertain projective geometry. Proceedings of Computer Vision and Pattern Recognition.

Hirschmüller H (2008) Stereo processing by semi-global match-ing and mutual information. EEE Transactions on Pattern Analysis and MachineIntelligence.

Hoegner L, Stilla U (2015) Building facade object detection from terrestrial thermal infrared image sequences combining different views. ISPRS Annals of the Photogrammetry, Remote Sensing and Spatial Information Sciences, II-3/W4: 55–62.

Hoegner L, Tuttas S, Stilla U (2017) Bim gestütztes monitoring von bauwerken aus bildsequenzen verschiedener sensoren und epochen. 19. Internationale Geodätische Woche Obergurgl 2017.

Hofer M, Maurer M, Bischof H (2015) Line3d: efficient 3d scene abstraction for the built environment. Computer Vision and Image Understanding (CVIU).

Holst C, Medić T, Kuhlmann H (2018) Dealing with systematic laser scanner errors due to misalignment at area-based deformation analyses. Journal of Applied Geodesy, 12 (2): 169–185.

Hough P (1962) Method and means for recognizing complex patterns. US Patent 3,069,654, Ser. No. 17,7156 Claims.

Huang R, Yusheng X, Hoegner L, Stilla U (2022) Semantics-aided 3d change detection on construction sites using uav-based photogrammetric point clouds. Automation in Construction, 134: 104057.

ISO (2008) Guide to the expression of uncertainty in measurement.

Iwaszczuk D (2015) Automatic texturing of 3d models of urban areas using image sequences from airborne tir cameras. PhD thesis, Technische Universität München, München.

Iwaszczuk D, Hoegner L, Schmitt M, Stilla U (2012) Linienbasiertes matching von 3d-gebäudemodellen mit ir luftbildsequenzen zur automatischen texturgewinnung. 32. Wissenschaftlich-Technische Jahrestagung der DGPF, : 195–201.

Iwaszczuk D, Stilla U (2017) Camera pose refinement by matching uncertain 3d building models with thermal infrared image sequences for high quality texture extraction. ISPRS Journal of Photogrammetry and Remote Sensing, 132: 33–47.

James MR, Robson S, Smith MW (2017) 3-d uncertainty-based topographic change detection with structure-from-motion photogrammetry: precision maps for ground control and directly georeferenced surveys. Earth Surface Processes and Landforms, 42 (12): 1769–1788.

Jung J, Bang K, Sohn G, Armenakis C (2016) Matching aerial images to 3d building models based on context-based geometric hashing. ISPRS Annals of Photogrammetry, Remote Sensing and Spatial Information Sciences, III-1: 17–23.

Jung J, Stachniss C, Ju S, Heo J (2018) Automated 3d volumetric reconstruction of multiple-room building interiors for as-built bim. Advanced Engineering Informatics, 38: 811–825.

Kada M, Haala N (2005) Façade texturing for rendering 3d city models. The International Archives of Photogrammetry and Remote Sensing, : 78–85.

Koch KR (2008) Evaluation of uncertainties in measurements by monte carlo simulations with an application for laserscanning. Journal of Applied Geodesy, 2 (2).

Koch T, Korner M, Fraundorfer F (2016) Automatic alignment of indoor and outdoor building models using 3d line segments. Proceedings of the IEEE Conference on Computer Vision and Pattern, : 689–697.

Kromer RA, Abellán A, Hutchinson DJ, Lato M, Chanut MA, Dubois L, Jaboyedoff M (2017) Automated terrestrial laser scanning with near-real-time change detection – monitoring of the séchilienne landslide. Earth Surface Dynamics, 5 (2): 293–310.

Läbe T, Ellenbeck KH (1996) 3d-wireframe models as ground control points for the automatic exterior orientation. International Archives of the Photogrammetry, Remote Sensing and Spatial Information Sciences, (Volume XXXI Part B2): 218–223.

Lague D, Brodu N, Leroux J (2013) Accurate 3d comparison of complex topography with terrestrial laser scanner: Application to the rangitikei canyon (n-z). ISPRS Journal of Photogrammetry and Remote Sensing, 82: 10–26.

Lee SC, Jung SK, Nevatia R (2002) Automatic pose estimation of complex 3d building models. Proceedings of Workshop on Application of Computer Vision, : 148–152.

Lerner R, Rivlin E, Rotstein H (2006) Pose and motion recovery from feature correspondences and a digital terrain map. IEEE Transactions on Pattern Analysis and Machine Intelligence, (9): 1404–1417.

Li-Chee-Ming J, Armenakis C (2013) Determination of uas trajectory in an known environment from fpv video. International Archives of the Photogrammetry, Remote Sensing and Spatial Information Sciences, (XL-1/W2): 247–252.

Li-Chee-Ming J, Armenakis C (2014) Feasibility study for pose estimation of small uas in known 3d environment using geometric hashing. Photogrammetric Engineering & Remote Sensing, 80 (12): 1117–1128.

Li-Chee-Ming J, Armenakis C (2017) Matching real and synthetic panoramic images using a variant of geometric hashing. ISPRS Annals of Photogrammetry, Remote Sensing and Spatial Information Sciences, IV-1/W1: 199–206.

Lichti DD (2007) Error modelling, calibration and analysis of an am–cw terrestrial laser scanner system. ISPRS Journal of Photogrammetry and Remote Sensing, 61 (5): 307–324.

Liu D, Li D, Wang M, Wang Z (2021) 3d change detection using adaptive thresholds based on local point cloud density. ISPRS International Journal of Geo-Information, 10 (3): 127.

Lowe DG (1991) Fitting parameterized three-dimensional models to images. IEEE Transactions on Pattern Analysis and Machine Intelligence, 13 (5): 441–450.

Maalek R, Lichti DD, Ruwanpura JY (2018) Robust segmentation of planar and linear features of terrestrial laser scanner point clouds acquired from construction sites. Sensors (Basel, Switzerland), 18 (3).

Meidow J, Beder C, Förstner W (2009) Reasoning with uncertain points, straight lines, and straight line segments in 2d. ISPRS Journal of Photogrammetry and Remote Sensing, 64 (2): 125–139.

Meyer T, Brunn A (2019) 3d point clouds in postgresql/postgis for applications in gis and geodesy. Proceedings of the 5th International Conference on Geographical Information Systems Theory, Applications and Management, : 154–163.

Meyer T, Brunn A, Stilla U (2021) Accuracy investigation on image-based change detection from bim compliant indoor models. ISPRS Annals of the Photogrammetry, Remote Sensing and Spatial Information Sciences, V-4-2021: 105–112.

Meyer T, Brunn A, Stilla U (2022a) Change detection for indoor construction progress monitoring based on BIM, point clouds and uncertainties. Automation in Construction, 141: 104442.

Meyer T, Brunn A, Stilla U (2022b) Genauigkeitsbetrachtung voxelbasierter änderungsdetektion im gebäudeinnenbereich zur automatisierten baufortschrittsüberwachung. Publikationen der DGPF, 30.

Meyer T, Brunn A, Stilla U (2022c) Geometric bim verification of indoor construction sites by photogrammetric point clouds and evidence theory. Under review for ISPRS Journal of Photogrammetry and Remote Sensing.

Molton N, Davison A, Reid I (2004) Locally planar patch features for real-time structure from motion. Proc. of the British Machine Vision Conference.

Moravec H, Elfes A (1985) High resolution maps from wide angle sonar. Proceedings. 1985 IEEE International Conference on Robotics and Automation, 2: 116–121.

Nakagawa M, Shibasaki R (2008) Building change detection using a 3-d texture model. The International Archives of the Photogrammetry, Remote Sensing and Spatial Information Sciences. Vol. XXXVII. Part B3a, : 173–178.

Nikoohemat S, Diakite A, Zlatanova S, Vosselmann G (2020) Indoor 3d reconstruction from point clouds for optimal routing in complex buildings to support disaster management. Automation in Construction, 113: 1–17.

Nikoohemat S, Koeva M, Oude Elberink SJ, Lemmen CHJ (2018) Change detection from point clouds to support indoor 3d cadastre. ISPRS - International Archives of the Photogrammetry, Remote Sensing and Spatial Information Sciences, XLII-4: 451–457.

Nyaruhuma AP, Gerke M, Vosselman G (2012) Verification of 3d building models using mutual information in airborne oblique images. ISPRS Annals of Photogrammetry, Remote Sensing and Spatial Information Sciences, I-3: 275–280.

Olszewski B, Fenton S, Tworek B, Liang J, Yelamarthi K (2013) RFID positioning robot: An indoor navigation system. In: IEEE International Conference on Electro-Information Technology , EIT 2013

Pexman K, Lichti DD, Dawson P (2021) Automated storey separation and door and window extraction for building models from complete laser scans. Remote Sensing, 13 (17): 3384.

Reineking T (2014) Belief functions: theory and algorithms. PhD thesis, Universität Bremen, Bremen.

Retscher G, Kistenich M (2006) zfv_2006_1_retscher_kistenich. ZfV, (1): 25–35.

Rother C (2000) A new approach for vanishing point detection in architectural environments. In Proc. 11th British Machine Vision, : 382–391.

Schickler W (1992) Feature matching for outer orientation of single images using 3-d wireframe controlpoints. International Archives for Photogrammetry (B3/III), : 591–598.

Sester M, Förstner W (1989) Object location based on uncertain models. Mustererkennung 1989, 219: 457–464.

Shafer G (1976) A Mathematical Theory of Evidence. Princeton University Press.

Shirowzhan S, Sepasgozar SM, Li H, Trinder J, Tang P (2019) Comparative analysis of machine learning and point-based algorithms for detecting 3d changes in buildings over time using bi-temporal lidar data. Automation in Construction, 105.

Soudarissanane S, Lindenbergh R, Menenti M, Teunissen P (2011) Scanning geometry: Influencing factor on the quality of terrestrial laser scanning points. ISPRS Journal of Photogrammetry and Remote Sensing, 66 (4): 389–399.

Tan K, Zhang W, Shen F, Cheng X (2018) Investigation of tls intensity data and distance measurement errors from target specular reflections. Remote Sensing, 10 (7): 1077.

Tian Y, Gerke M, Vosselman G, Zhu Q (2008) Automatic edge matching across an image sequence based on reliable points. The International Archives of Photogrammetry, Remote Sensing and Spatial Geoinformation Sciences, : 657–662.

Tran H, Khoshelham K (2020) Procedural reconstruction of 3d indoor models from lidar data using reversible jump markov chain monte carlo. Remote Sensing, 12 (5): 838.

Tuttas S, Braun A, Borrmann A, Stilla U (2017) Acquisition and consecutive registration of photogrammetric point clouds for construction progress monitoring using a 4d bim. PFG – Journal of Photogrammetry, Remote Sensing and Geoinformation Science, 85 (1): 3–15.

Unger J, Rottensteiner F, Heipke C (2016) Integration of a generalized building model into the pose estimation of uas images. ISPRS - International Archives of the Photogrammetry, Remote Sensing and Spatial Information Sciences, XLI-B1: 1057–1064.

Unger J, Rottensteiner F, Heipke C (2017) Assigning tie points to a generalised building model for uas image orientation. ISPRS - International Archives of the Photogrammetry, Remote Sensing and Spatial Information Sciences, XLII-2/W6: 385–392.

USIBD (2019) Level of accuracy specification 3.0.

van den Heuvel F (1998) Vanishing point detection for architectural photogrammetry. International archives of photogrammetry and remote sensing, H. Chikatsu & E. Shimizu (eds.), Vol. 32 part 5, : 652–659.

Vosselman G (1992) Relational matching: Zugl.: Bonn, Univ., Diss, volume 628 of Lecture notes in computer science. Berlin: Springer.

Want R, Hopper A, Falcão V, Gibbons J (1992) The active badge location system. ACM Transactions on Information Systems, 10 (1): 91–102.

Witte B, Sparla P, Blankenbach J (2020) Vermessungskunde für das Bauwesen mit Grundlagen des Building Information Modeling (BIM) und der Statistik. Wichmann Verlag, 9 edition.

Wujanz D, Burger M, Tschirschwitz F, Nietzschmann T, Neitzel F, Kersten TP (2018) Determination of intensity-based stochastic models for terrestrial laser scanners utilising 3d-point clouds. Sensors (Basel, Switzerland), 18 (7).

Wysocki O, Hoegner L, Stilla U (2022) Refinement of semantic 3d building models by reconstructing underpasses from MLS point clouds. International Journal of Applied Earth Observation and Geoinformation, 111: 102841.

Xu Y, Tong X, Stilla U (2021) Voxel-based representation of 3d point clouds: Methods, applications, and its potential use in the construction industry. Automation in Construction, 126: 103675.

Yang F, Zhou G, Su F, Zuo X, Tang L, Liang Y, Zhu H, Li L (2019) Automatic indoor reconstruction from point clouds in multi-room environments with curved walls. Sensors (Basel, Switzerland), 19 (17).

Youssef MA, Agrawala A, Udaya Shankar A (2003) Wlan location determination via clustering and probability distributions. : 143–150.

Zámečníková M, Wieser A, Woschitz H, Ressl C (2014) Influence of surface reflectivity on reflectorless electronic distance measurement and terrestrial laser scanning. Journal of Applied Geodesy, 8 (4).

Zhang C, Arditi D (2013) Automated progress control using laser scanning technology. Automation in Construction, 36: 108–116.

Zlatoff N, Tellez B, Baskurt A (2006) Region-based perceptual grouping: a cooperative approach based on dempster-shafer theory. In: Dougherty ER, Astola JT, Egiazarian KO, Nasrabadi NM, Rizvi SA (eds) SPIE Proceedings